

Review

Recent Advances of Cobalt-Based Electrocatalysts for Oxygen Electrode Reactions and Hydrogen Evolution Reaction

Haihong Zhong¹, Carlos A. Campos-Roldán², Yuan Zhao^{2,3}, Shuwei Zhang¹, Yongjun Feng^{1,*}  and Nicolas Alonso-Vante^{2,*} 

¹ State Key Laboratory of Chemical Resource Engineering, Beijing University of Chemical Technology, No. 15 Beisanhuan East Road, Beijing 100029, China; 2014200922@grad.buct.edu.cn (H.Z.); zhangshuwei024@gmail.com (S.Z.)

² IC2MP, UMR-CNRS 7285, University of Poitiers, F-86022 Poitiers cedex, France; carlos.campos.rolan@univ-poitiers.fr (C.A.C.-R.); yuan.zhao@univ-poitiers.fr (Y.Z.)

³ College of Material Science and Science Technology, Nanjing University of Aeronautics and Astronautics, Nanjing 211106, China

* Correspondence: yjfeng@mail.buct.edu.cn (Y.F.); nicolas.alonso.vante@univ-poitiers.fr (N.A.-V.); Tel.: +86-106-443-6992 (Y.F.); +33-549-453-625 (N.A.-V.)

Received: 1 September 2018; Accepted: 14 November 2018; Published: 19 November 2018



Abstract: This review summarizes recent progress in the development of cobalt-based catalytic centers as the most potentially useful alternatives to noble metal-based electrocatalysts (Pt-, Ir-, and Ru-based) towards the oxygen reduction reaction (ORR), oxygen evolution reaction (OER), and hydrogen evolution reaction (HER) in acid and alkaline media. A series of cobalt-based high-performance electrocatalysts have been designed and synthesized including cobalt oxides/chalcogenides, Co-N_x/C, Co-layered double hydroxides (LDH), and Co-metal-organic frameworks (MOFs). The strategies of controllable synthesis, the structural properties, ligand effect, defects, oxygen vacancies, and support materials are thoroughly discussed as a function of the electrocatalytic performance of cobalt-based electrocatalysts. Finally, prospects for the design of novel, efficient cobalt-based materials, for large-scale application and opportunities, are encouraged.

Keywords: electrocatalysis; cobalt-based electrocatalysts; oxygen reduction reaction; oxygen evolution reaction; hydrogen evolution reaction; non-precious metal

1. Introduction

Considering the continuous decrease of fossil fuels and deteriorated environments, it is of great importance and urgency to explore abundant, eco-friendly and renewable energy sources. Many energy conversion and storage technologies, e.g., proton exchange membrane fuel cells (PEMFCs, in which the free energy of a chemical reaction is directly converted into electrical energy), water electrolyzers (WEs, where oxygen and hydrogen from water are produced), unitized regenerative cells (URCs, a system comprising an electrolyzer and a fuel cell), due to their high efficiency and friendly environments, have been extensively developed [1,2]. To some extent, electrochemical processes play an essential role in these systems, for example, the oxygen reduction reaction (ORR) and hydrogen oxidation reaction (HOR) occurring on the cathode and anode of a H₂-O₂ fuel cell, whereas the oxygen evolution reaction (OER) and hydrogen evolution reaction (HER) are, respectively, the anodic and cathodic reactions in an electrolyzer [3–5]. Platinum-based materials perform efficiently the HOR with much less Pt mass loading (0.05 mg cm⁻²) at the anode [6]. The complex oxygen electrode reactions (oxygen reduction reaction and oxygen evolution reaction), which involve various elementary steps,

are kinetically intrinsic sluggish reactions, and primarily catalyzed by precious metal centers, e.g., Pt, Ir, Ru. The limited resources and high cost of these precious metals are an unavoidably obstacle for widespread commercial applications [7]. Therefore, it is of increasing interest to reduce the usage of precious metals, or completely replace precious metals with abundant, cheap and highly active ones. In the past few years, various kinds of novel non-precious metal nanomaterials have been explored as alternatives to precious metal-based electrocatalysts, including strongly coupled transition metals (oxides, phosphides, chalcogenides, hydroxides, double perovskites, and so on) [8–14], nanocarbon hybrids [15], and free-metal carbon-based materials [7,16].

Cobalt (Co), the 32nd most abundant element in the Earth's crust, has emerged as an attractive non-precious metal for electrochemical reactions due to its catalytic performance. The price of cobalt per mass fluctuates over the years; currently its average-price is estimated at 72.82–48.07 €/kg (January–October 2018). From 2005 to 2018, the price has been subjected to small or important changes, meaning that the market is rather sensitive to the use purposes and to the localized reserve in the world. Regarding selenium and sulfur, for the period January to October 2018, the average-price ranges are 23.208–36.109 €/kg, and 0.063–0.067 €/kg, respectively. A series of cobalt-based catalytic center materials such as chalcogenides [17–22], oxides [23–25], metal–organic frameworks (MOFs) [26–30] and layered double hydroxides (LDHs) [31–33], have been recognized as potential candidates because of their parallel or even better activities, and superior electrochemical stability, compared with precious metals (Pt, Ir and Ru) [34]. Additionally, recent research results have established that cobalt-containing compounds supported onto conducting carbonaceous materials, e.g., Vulcan-XC-72 [35], nitrogen-doped carbon nanotubes (CNTs) [36], carbon nanoweb (CNWs) [37], graphene [38], reduced graphene oxide (RGO) [39,40] and so on, represent a valid way to endow the catalysts with rich exposed catalytic sites, high surface area, high electrical conductivity and fast mass transport, thus enhancing the catalytic activities.

In this review, we stress this novel cobalt-based material (CoCat) associated with some electrochemical processes, e.g., ORR, OER and HER in acid and alkaline electrolytes from the surface electrochemistry perspective. All these carbons supported cobalt-centered catalysts are organized into several categories, namely, cobalt oxides, cobalt chalcogenides (selenides, sulfides), Co-LDH, Co-MOFs, and Co-N_x/C, see Figure 1. In what follows, we firstly illustrate the basic reaction mechanism of ORR, OER and HER, then summarize recent progress in the development of cobalt-based electrocatalysts towards ORR, OER, HER. For the Co-centered electrocatalysts, particular attention is paid to the design, synthesis strategies, and electrocatalytic performance. Finally, we further discuss the challenges ahead in designing novel, highly efficient cobalt-based electrocatalysts for large-scale applications and opportunities.

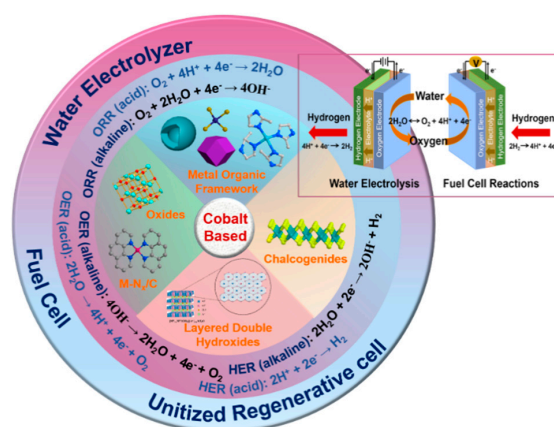


Figure 1. Schematic organization of the cobalt-based catalysts (CoCat) including layered double hydroxides, chalcogenides, oxides, M-N_x/C and metal organic framework with some major applications.

2. Electrocatalysts for Oxygen Reduction Reaction (ORR)

2.1. Mechanism of ORR

The oxygen reduction reaction is the cathodic electrode reaction. The ORR electrochemical properties can be evaluated from rotating disc electrode (RDE) measurements (namely, the onset potential (E_{onset}), half-wave potential ($E_{1/2}$), overpotential (η), and diffusion-limiting current density (j_L)). The ORR electrochemical reactions, in acid and alkaline medium, are shown below. The adsorbed molecular oxygen is reduced by a “direct” four-electron charge transfer process or reduced to water (acid medium) or OH^- (alkaline medium) via the formation of HO_2^- and H_2O_2 intermediates with the consumption of two electrons [41]. In acid condition, oxygen can be reduced to water with a standard thermodynamic potential at 1.229 V vs. SHE (Standard Hydrogen Electrode) for the four-electron pathway (Equation (1)); while in the alkaline medium, hydroxide is produced with a standard thermodynamic potential at 0.401 V vs. SHE in the four-electron reaction (Equation (4)). The charge-transfer reaction depends on the electrolyte nature and the surface properties of the catalytic centers. Even for Pt, considered as the best ORR catalyst, a substantial cathodic overpotential of 300 mV [41] is observed in acid electrolyte. Clearly, a selectivity for the four- e^- reduction pathway is highly desirable to improve the electrocatalytic ORR efficiency.

Acid medium:



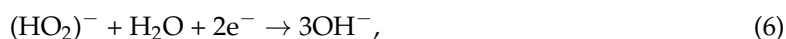
or



Alkaline medium:



or



2.2. Oxygen Reduction on Cobalt Chalcogenides Catalysts

2.2.1. Bond Ionicity or Covalency of S, Se, Te

In transition metals (TM) chalcogenides, the increase of covalency is obtained when d-state of TM interact with p-state of chalcogenides take place in MX_2 compounds (e.g., M: Co; X: S, Se). The hybridization degree of chalcogenides p-state with d-state of TM favors the metal–metal interaction. Moreover, metal cluster chalcogenides catalysts, $\text{Ru}_2\text{Mo}_4\text{X}_8$ (Chevrel phase), where X: Se- and S-based, have motivated a strong interest since Alonso-Vante and Tributsch [42] in 1986 reported the comparable ORR activity of $\text{Ru}_2\text{Mo}_4\text{Se}_8$ to that of Pt in H_2SO_4 [43–46]. In binary metal clusters (e.g., Ru) coordinated with X, they proposed that the activity of Ru_xX_y catalysts depends on the chalcogen, and increases according to: $\text{Ru}_x\text{S}_y < \text{Ru}_x\text{Te}_y < \text{Ru}_x\text{Se}_y \sim \text{Mo}_x\text{Ru}_y\text{Se}_z$ in acid solution [47]. The structure analysis from the EXAFS (Extended X-ray Absorption Fine Structure) data suggested that that the variation of the chalcogen nature led to a change in its amount in the first co-ordination sphere of ruthenium. The latter apparently affected the strength of ruthenium interaction with oxygen, which is evidenced by significant differences observed in the Ru/O distances. For Ru_xS_y clusters, the high co-ordination number of Ru to sulfur resulted in blocking the ruthenium active sites towards adsorption of molecular oxygen, which showed lowest ORR catalytic activity. In this respect, the coordinating strength of S, Se, Te on Ru chalcogenides was demonstrated (ligand effect). This is in contrast to cobalt dichalcogenides compound (CoX_2) demonstrated by Behret et al. [48] that reported a trend of ORR activity basically followed the sequence: $\text{M}_x\text{S}_y > \text{M}_x\text{Se}_y > \text{M}_x\text{Te}_y$. In addition, the activity was also related to the catalytic

centers with Co. Both theoretical and experimental results confirmed that Co–selenides are less active than its sulfides by ~ 0.2 V [49]. The considerable decrease in activity was observed when S was partly or totally substituted by O, Se, and Te, probably attributed to the geometric and electrostatic conditions in spinel structures. It was claimed that the selenium and tellurium with higher atomic radii give a weaker electrostatic repulsion to the reduction product (O^{2-}) and also to the intermediate reduction products. Therefore, the reaction products on the surface of seleno- and tellurospinel were not as easily desorbed as those on thiospinels [48].

Furthermore, a series of transition metal chalcogenides were reported by Behret et al. [48] consisting of the anionic substitution (S, Se and Te), and the cationic substitution (Fe, Co, Ni). These primary results disclosed a trend for ORR electrochemical performance with the metal cations as follows: $Co > Ni > Fe$, and for the chalcogenide anions: $S > Se > Te$. They found that Co–S and Co–NiS systems possessed very high catalytic activity in acidic medium. They declared that better catalytic activity may be caused by the minimal energy difference between the oxygen 2p orbital and the highest occupied d orbital of sulfides [50]. CoS was, apparently, the most promising ORR non-precious metal catalyst in alkaline media. Besides, Co_9S_8 was predicted to have similar ORR activity with that of Pt via a four-electron ORR pathway in acidic solution [51]. Zhu et al. [52] developed a simple and scalable route to synthesize 3D hybrid nanocatalyst—the Co_9S_8 incorporated in N-, S-doped porous carbon exhibited an excellent catalytic activity, superior long-term stability, and good tolerance against methanol. Recently, Dai et al. [19], for the first time, designed and prepared the etched and doped Co_9S_8 /graphene hybrid as an advanced bifunctional oxygen electrode reactions catalyst.

2.2.2. Crystal Structure and Particle Size Effect

The different crystal structures with the same chemical composition led to the different ORR catalytic activity. For instance, $CoSe_2$ has two common crystal structures: cubic (pyrite-type), and orthorhombic marcasite-type. Alonso-Vante and Feng [53,54] discovered that the orthorhombic $CoSe_2$ was obtained after a heat treatment of 250–300 °C. The cubic $CoSe_2$ phase was obtained at high temperature (400–430 °C). The latter showed a higher ORR activity by 30 mV in 0.5 M H_2SO_4 . Wu et al. [55] prepared cubic Co_9S_8 particles surrounded by nitrogen-doped graphene sheets for the ORR in alkaline medium with an improved ORR activity and stability comparable to Pt/C. Similarly, cobalt sulfides with different chemical compositions and crystal structures, namely, $Co_{1-x}S$, CoS (hexagonal phase) [56], CoS_2 , Co_9S_8 and Co_3S_4 (cubic phase) [56], are the most promising type of chalcogenides for the ORR. As an illustration, Dai et al. [18] obtained the Co_2S/RGO with an average particle size of ca. 50 nm and $Co_{1-x}S/RGO$ with an average particle size of 10–20 nm. The latter displayed a better ORR activity in terms of the onset potential of ca. 0.8 V vs. RHE (Reversible Hydrogen Electrode) in 0.5 M H_2SO_4 . The authors noticed that the ORR performance depends on the particle size and on the crystal structure.

Generally, the mass activity (MA, activity $mass^{-1}$) of a catalyst is defined as the current normalized by the noble metal loading or catalyst loading as measured at a specific electrode potential. In order to increase MA, some strategies can be adopted, i.e., increasing the specific surface area of the catalysts by decreasing the particle size [57]. The particle size effect on the specific activity of catalysts has been attributed to different factors, such as, the structural sensitivity, i.e., the dependence of surface geometry, the electronic state, and the metal–support interaction [58]. Moreover, the particle size of the catalysts on the oxygen reduction reaction can be influenced by the adsorption of oxygen during the reaction, which is mainly associated with the fraction of active sites on the surface of the catalysts. Wang et al. [59] demonstrated that the Pd_3Co alloy had a slightly smaller lattice spacing than that of Pd, and thus a further shifting to larger size was expected due to the stronger lattice-induced compression. The 3-fold enhancement in the specific activity of Pd_3Co could be attributed to the nanosized-, and lattice mismatch-induced contraction in (111) facets, based on the DFT (density Functional Theory) calculation using a nanoparticle model. Feng et al. [46] developed cubic CoS_2 nanocatalysts with different particle size from 30 nm to 80 nm by adjusting the initial Co^{2+} concentration in the presence of

hexa-decylcetyl-trimethylammonium (CTAB), and further demonstrated that the ORR activity depends on the average particle size, see Figure 2. The ORR activity remained similar to the particle size from 30 nm to 50 nm, and then significantly decreased with size from 50 nm to 80 nm. The CoS₂ catalyst with an average particle size of 30.7 nm demonstrated an excellent electrocatalytic performance with an onset potential (E_{onset}) of 0.94 V vs. RHE, a half-wave potential of 0.71 V vs. RHE, and high tolerance in methanol-containing 0.1 M KOH. Such a trend was also found for 20 wt% Co₃S₄/C nanoparticles and 20 wt% CoSe₂/C [60]. The particle size can be approximately adjusted within a certain range by controlling the initial feeding concentrations, which has strong effect on the crystal nucleation and crystal growth.

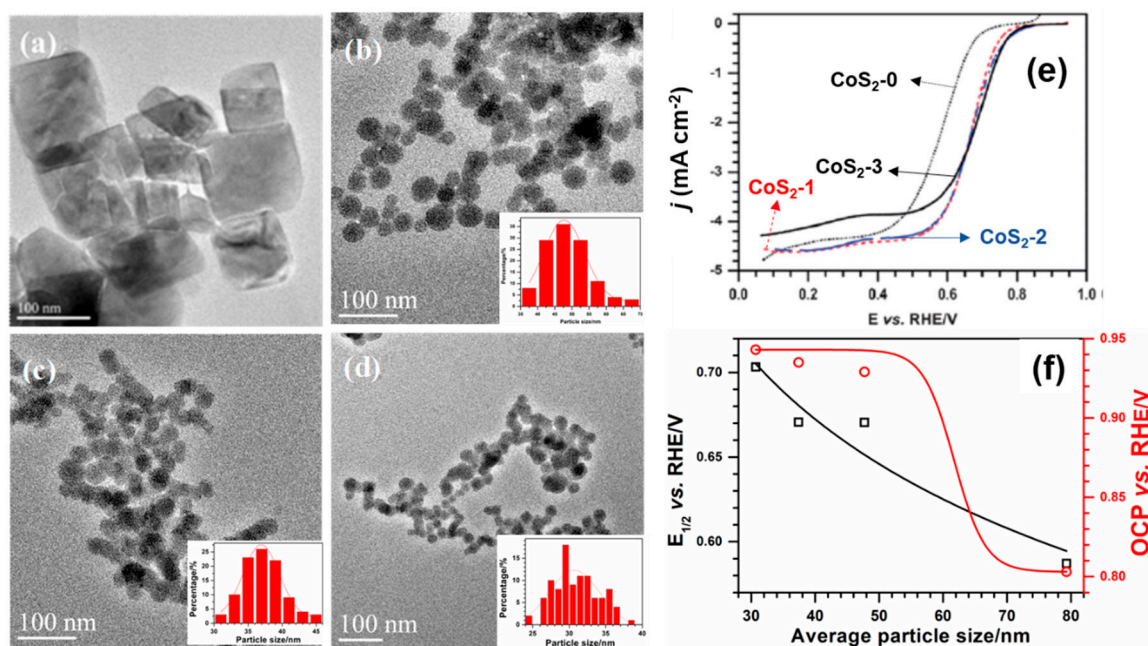


Figure 2. (a–d) High-resolution transmission electron microscope (HRTEM) images of CoS₂-0 (without addition of hexa-decylcetyl-trimethylammonium (CTAB)), CoS₂-1, -2, and -3 nanoparticles with the initial Co²⁺ concentrations from 0.025 M to 0.075 M in the presence of 0.5 mM CTAB; (e) rotating disc electrode (RDE) curves of the four CoS₂ samples in O₂-saturated 0.1 KOH at 1600 rpm at a scan rate of 5 mV s⁻¹ (cathodic sweep) at room temperature. The catalyst loading was 0.1 mg cm⁻²; (f) half-wave potential ($E_{1/2}$) and OCP (Open Circuit Potential) extracted from Tafel plots as a function of the average CoS₂ particle size. Reproduced from [46], Copyright © Royal Society of Chemistry, 2013.

2.2.3. Synthesis and Support Effect

Cobalt selenides have received extensive attention for their ORR activity [61,62]. This electrocatalyst deposited on highly conductive supporting material is very important to enhance the electrocatalytic performance. The ideal supporting materials for catalytic centers have high surface area, high electrical conductivity, and high chemical stability [63]. Taking advantage of the high surface area of amorphous carbon, Feng et al. [62] synthesized via a surfactant-free way the CoSe₂ orthorhombic-phase nanoparticle supported onto XC-72 Vulcan with a promising ORR performance in acid media. Zhou et al. [64] developed supported CoSe₂ nanostructures by a hydrothermal approach using the increased disordered domains of carbon nanotubes (CNTs) derived from a MOF with excellent ORR performance in 0.1 M KOH with a Tafel slope of 45 mV dec⁻¹, onset potential of ca. 0.8 V vs. RHE, and a long-term stability. Although a relative success was obtained, the major drawback of the hybrid catalysts is the weak interaction between the catalytic centers and the support leading to low activity and stability. The formation of interfacial bonds between the catalytic center and the support favors the adsorption properties, therefore, enhancing the kinetics toward the electrocatalytic reaction [65].

The catalytic–support interaction may weaken the adsorption events, and then decrease the energy barriers for the reaction. This phenomenon, known as strong metal–support interaction (SMSI) is an important ingredient to tailor, and tune highly active and stable catalyst centers. Unni et al. [66] fabricated high-surface area N-doped carbon nanohorns (NCNH) supported cubic-phase CoSe_2 via a simple NaBH_4 -chemical reduction process of CoCl_2 and SeO_2 , Figure 3a,b. The $\text{CoSe}_2/\text{NCNH}$ demonstrated considerable ORR activity in alkaline medium, cf. Figure 3c,d, as a result of the electronic structure modification of chalcogenide (CoSe_2) centers throughout its interaction with NCNH via the nitrogen moieties, Figure 3e.

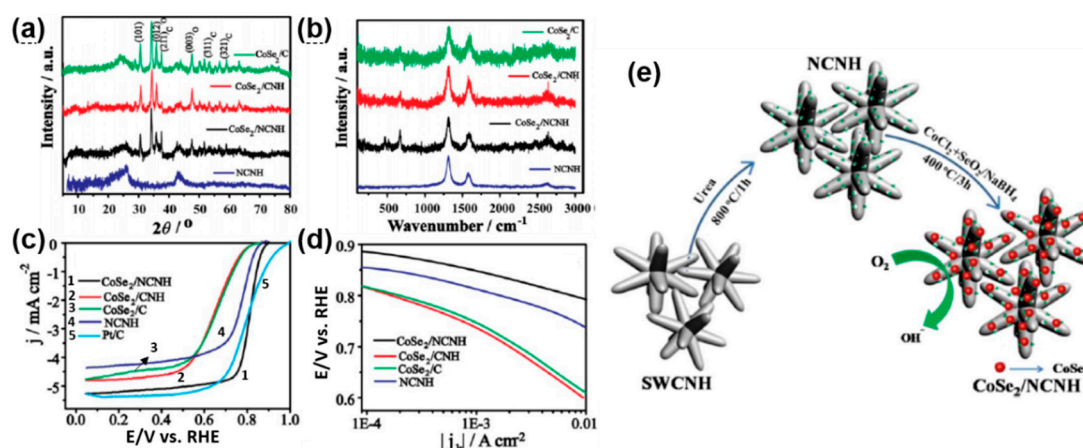


Figure 3. (a) Raman spectra; (b) X-ray diffraction (XRD) patterns; (c) oxygen reduction reaction (ORR) polarization curves of CoSe_2/N -doped carbon nanohorns (NCNH), $\text{CoSe}_2/\text{carbon nanohorns}$ (CNH), CoSe_2/C , NCNH and Pt/C catalysts in O_2 -saturated 0.1 KOH at 1600 rpm at a scan rate of 5 mV s^{-1} (cathodic sweep) at 25°C . The catalyst loading was 0.214 mg cm^{-2} ; (d) ORR Tafel plots of supported CoSe_2 onto carbon Vulcan, CNH and NCNH; (e) schematics of the synthesis procedure. Reproduced from [66], Copyright © Wiley, 2015.

Similarly, García-Rosado et al. [67] prepared a series of N-doped reduced graphene oxide (N-RGO) as supports for hexagonal cobalt selenide (CoSe) by a NaBH_4 -assisted chemical reduction, Figure 4. The carbon support after the surface reduction supplied more available active and anchor sites due to the increase in the pore size and surface area. The ORR performance is concomitant with the properties of the supports. The graphitic and pyridinic nitrogen moieties of N-RGO acted as electrochemical active sites for the ORR in alkaline media.

Additionally, Pan et al. [68] used porous $g\text{-C}_3\text{N}_4$ as a template and a N-source to successfully synthesize mesoporous S-, and N-co-doped carbon matrix coupled with $\text{Co@Co}_9\text{S}_8$ nanoparticles, cf. Figure 5. Herein, the $g\text{-C}_3\text{N}_4$ carbon matrixes not only enhance the conductivity, but also suppress the aggregation phenomenon during the electrochemical reactions. Besides, the strong coupling between $\text{Co@Co}_9\text{S}_8$ and N-, S-carbon promoted significantly the ORR electrocatalytic performance with a more positive half-wave potential and lower Tafel slope value, as compared with the commercial Pt/C catalyst.

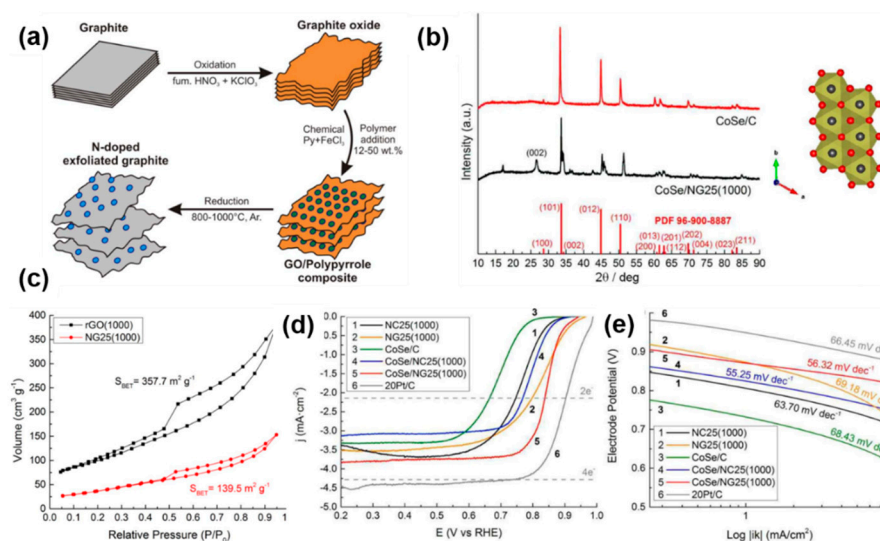


Figure 4. (a) scheme of the synthesis of N-doped reduced graphene oxide (N-RGO); (b) XRD patterns of supported hexagonal CoSe onto GO and N-RGO; (c) BET–nitrogen adsorption–desorption isotherms of rGO(1000), and NG25(1000); (d) ORR polarization curves of NC25(1000), NG25(1000), CoSe/C, CoSe/NC25(1000), CoSe/NG25(1000) and Pt/C electrocatalysts at 900 rpm (cathodic sweep) in O₂-saturated 0.1 M KOH at 25 °C with the catalyst loading of 0.286 mg cm⁻²; and (e) ORR Tafel plots of supported CoSe catalysts in alkaline medium. Reproduced from [67], Copyright © The Electrochemical Society, 2017.

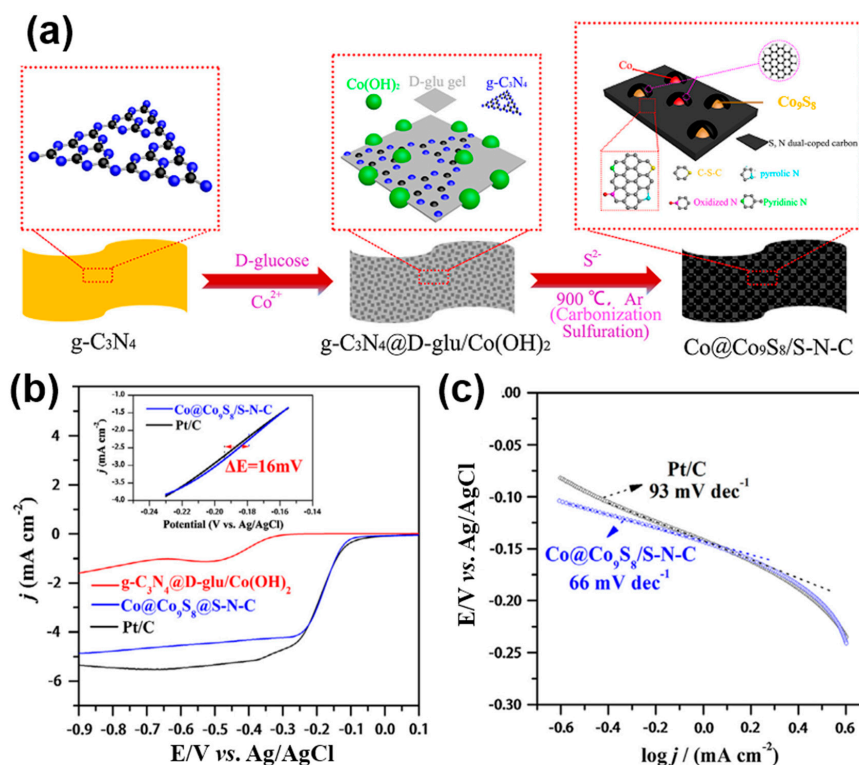


Figure 5. (a) The schematic chemical synthesis route of Co@Co₉S₈/S-N-C; (b) linear sweep voltammetry (LSV) curves for the g-C₃N₄@D-glu/Co(OH)₂, Co@Co₉S₈/S-N-C, and Pt/C electrodes recorded in O₂-saturated 0.1 M KOH solution at 1600 rpm with scan rate of 10 mV s⁻¹ (cathodic sweep) at 25 °C (catalyst mass loading: 0.2 mg cm⁻²); (c) Tafel plots of Co@Co₉S₈/S-N-C and Pt/C catalysts. Reproduced from [68], Copyright © Elsevier, 2018.

2.3. Oxygen Reduction on Metal–Organic Frameworks (MOFs) Catalysts

MOFs and their derivatives have also been used as efficient precursors and self-sacrificing templates because of their well-tunable physical and chemical properties. Benefiting from the unique properties of MOF, such as, large surface area, tailoring porosity, and easy functionalization with other heteroatoms or metal/metal oxides, various carbon-based nanomaterials (as support) have been prepared. Based on organic ligands and cobalt metal centers, MOFs compounds possess special superiority to prepare various cobalt-based functionalized carbon nanomaterials, including heteroatom-doped porous carbons, and metal/metal oxide decorated porous carbons, via thermal decomposition under controlled atmospheres. For instance, Lou et al. [69] used ZIF-67 as a template and thioacetamide as a sulfur source to prepare a double-shelled Co–C@Co₉S₈ nanocages electrocatalyst for the ORR. By adjusting the reaction time, the amorphous CoS nanocages (a–CoS NCs) and ZIF-67@a–CoS yolk-shelled hollow nanostructures were fabricated. The Co₉S₈ shells, served as a nanoreactor, effectively prevented the Co–C active centers from aggregation, Figure 6a. Interestingly, the unique Co–C hollow cages significantly shortened the diffusion pathway of the electrolyte, and thus promoted the electrocatalytic activity, durability, and tolerant to methanol toward the ORR of Co–C@Co₉S₈ catalyst. In Figure 6b–e, the onset potential remarkably reached 0.96 V vs. RHE with a limiting current of 4.5 mA cm⁻² and a four-electron transfer route with OH⁻ production in alkaline media.

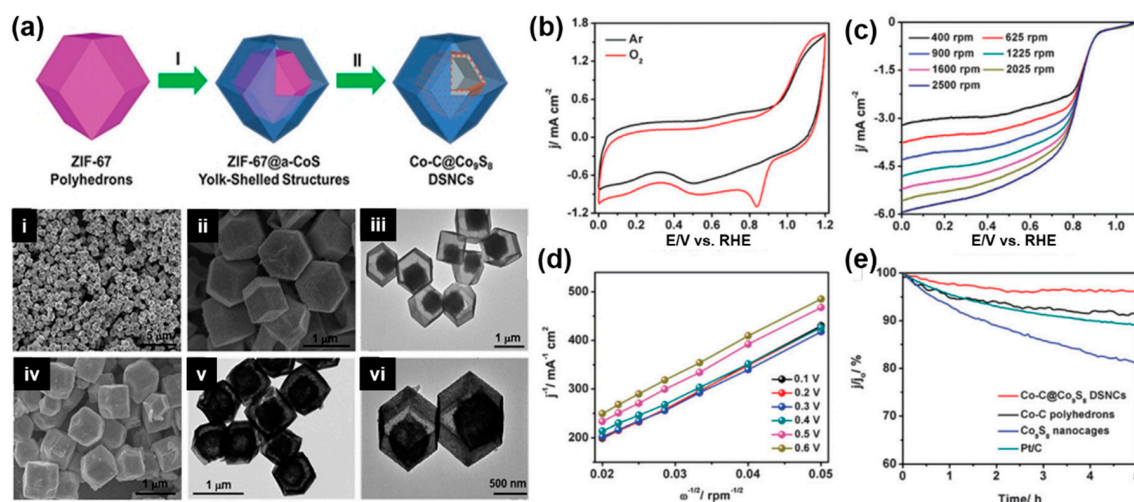


Figure 6. (a) The synthesis route of Co–C@Co₉S₈ DSNCs (double-shelled nanocages); (i–vi) field-emission scanning electron microscopy (FESEM) and TEM micrographs of the catalyst; (b) CV curves of Co–C@Co₉S₈ DSNCs in Ar- or O₂-saturated 0.1 M KOH electrolyte with a scan rate of 10 mV cm s⁻¹; (c) LSV (cathodic sweep) curves of Co–C@Co₉S₈ DSNCs catalyst recorded at different rotation speeds from 400 to 2500 rpm in O₂-saturated 0.1 M KOH; (d) the K–L plots of Co–C@Co₉S₈ DSNCs at various potentials (0.1–0.6 V vs. RHE (Reversible Hydrogen Electrode)); (e) the chronoamperometric responses (j/j_0 (%) vs. t) of Co–C@Co₉S₈ DSNCs, Co–C polyhedrons, Co₉S₈ nanocages and Pt/C electrodes at 0.5 V in O₂-saturated 0.1 M KOH solution at 1600 rpm. Reproduced from [69], Copyright © Royal Society of Chemistry, 2015.

Additionally, a simple and efficient method to produce homogeneously dispersed cobalt sulfide/N-, S-co-doped porous carbon electrocatalysts, using ZIF-67 as precursor and template, was reported by Xia et al. [70]. Due to a unique core–shell structure, high porosity, homogeneous dispersion of active components together with N-, and S-doping effects, the electrocatalyst not only showed an excellent electrocatalytic activity towards ORR with a high onset potential (ca. -0.04 V compared with -0.02 V for the benchmark Pt/C catalyst), but also revealed a superior stability (92%) compared with the commercial Pt/C catalyst (74%) in ORR.

Table 1 summarizes some transition metal chalcogenides as ORR catalysts investigated so far. One can conclude that: (1) Co-based chalcogenides are promising catalysts for the ORR in alkaline media; (2) the carbon support having a pore morphological structure, and hetero-atom doping plays a key role to promote the ORR performance of Co-based chalcogenides.

2.4. Oxygen Reduction on Cobalt Oxide Catalysts

2.4.1. Nanostructure

Intensive efforts have been devoted to fabricate various surface-tuned cobalt oxides materials with different nanostructures and morphologies, including Co_3O_4 nanorods [71], nanowires [72], core-shell [73], and hollow structures [74], which are responsible for the electrochemical performance. For example, Kurungot et al. [75] prepared a series of surface-tuned Co_3O_4 nanoparticles with different morphologies (cubic ($\text{Co}_3\text{O}_4\text{-NC/NGr-9h}$), blunt-edged cubic ($\text{Co}_3\text{O}_4\text{-BC/NGr-12h}$), and rough edged spherical ($\text{Co}_3\text{O}_4\text{-SP/NGr-24h}$)) dispersed on nitrogen-doped graphene (NGr) electrocatalysts for ORR by varying the reaction time. The transformations of the morphologies of Co_3O_4 could be assigned to the transformation of the higher to the lower surface energy crystal plane structure, which was expected to obtain the mixed facets of the exposed Co-oxide crystals. Among them, the NGr supported spherical Co_3O_4 ($\text{Co}_3\text{O}_4\text{-SP}$) nanoparticles ($\text{Co}_3\text{O}_4\text{-SP/NGr-24h}$) with the highest roughness factor and increased surface area exhibited the best activity in alkaline medium, and attributed to: (1) homogenous dispersion of Co_3O_4 nanoparticles on NGr support; (2) NGr served as nucleation sites, efficiently controlling the growth kinetics of Co_3O_4 nanoparticles; and (3) a strong synergistic interaction between the active sites and the support.

2.4.2. Particle Size Effect and Chemical Composition

Different particle size also influences the electrocatalytic active surface. For example, Feng's group [76] synthesized a series of $\text{Co}_3\text{O}_4/\text{N-RGO}$ composites with different particle size by controlling Co^{2+} initial feeding concentrations, and carefully investigated the particle size effect of Co_3O_4 nanoparticles on the bifunctional oxygen electrocatalytic performance. The $\text{Co}_3\text{O}_4/\text{N-RGO}$ with the smallest particle size of 12.2 nm revealed the best bifunctional oxygen activity (ORR and OER) with lower $\Delta E = 0.75$ V ($\Delta E = E_{\text{OER}, j@10 \text{ mA cm}^{-2}} - E_{\text{ORR}, j@-3 \text{ mA cm}^{-2}}$) ($E_{\text{OER}, j@10 \text{ mA cm}^{-2}}$, the potential at a current density of 10 mA cm^{-2} for OER; $E_{\text{ORR}, j@-3 \text{ mA cm}^{-2}}$, the potential at a current density of -3 mA cm^{-2} for ORR) than other larger particle sized samples. Sun and co-workers [77] investigated, on the other hand, the impact of the CoO particle size on the ORR activity via a combined controllable hydrolysis and thermal treatment process. The promoted ORR current and the increased content of HO_2^- produced over the smallest CoO particles benefited from the increase of the interface between carbon support and CoO nanoparticles (NPs). Thus, the interface between carbon and CoO NPs could be identified as the most active site.

Besides the control of particles' size, fine-tuning of the chemical composition (e.g., $\text{Co}^{3+}/\text{Co}^{2+}$ ratio) was an effective strategy to boost the electrocatalytic activity of cobalt oxide catalysts. Liu et al. [78] proposed an interesting approach to enhance the electrocatalytic activity of Co_3O_4 nanosheets through the modulation of the inner oxygen vacancy concentration, and the $\text{Co}^{3+}/\text{Co}^{2+}$ ratio. Based on the synergistic effect of the fashioned 2D nanosheets, the presence of oxygen vacancies, and the $\text{Co}^{3+}/\text{Co}^{2+}$ ratio, the catalyst showed a much lower overpotential towards ORR and OER for Li-O₂ batteries. Furthermore, Zhao's group [79] reported that the ORR catalytic activity of the prepared catalysts is sensitive to the number and activity of surface-exposed Co^{3+} ions that could be tailored by the morphology of cobalt oxides.

2.4.3. Support Effect

Cobalt oxide (Co_3O_4 and CoO) nanoparticles are recognized as a class of non-precious catalysts with high activity, stability and durability in alkaline solution. For example, $\text{Co}_3\text{O}_4/\text{graphene}$

hybrids had a remarkable ORR performance comparable to that of commercial Pt/C in alkaline, which was attributed to the synergistic catalyst-support coupling [25]; as for graphene supported 3D “sheet-on-sheet” interleaved Co_3O_4 nanosheets (Co-S/G), the strong electron transport and charge transfer from graphene to Co_3O_4 nanosheets significantly enhanced the ORR electrocatalytic properties of Co-S/G [80].

Bao et al. [81] proposed that the excessive ascorbic acid (AA) could form abundant negative functional groups on the surface of 3D graphene aerogel (3DG, Figure 7a), with Co^{2+} ions uniformly anchored on 3DG by electrostatic or coordination interaction. The hollow Co_3O_4 /3DG was synthesized by a direct oxidation of C@Co/3DG precursor through the Kirkendall effect, Figure 7b. The prepared Co_3O_4 /3DG (22 wt% Co_3O_4) electrocatalyst showed a positive onset potential of 0.82 V vs. RHE, and a limiting current density of 5.12 mA cm^{-2} (1600 rpm), Figure 7c. The rotating ring disk electrode (RRDE) method further confirmed a charge transfer pathway close to 4-electron with a production of hydrogen peroxide (HO_2^-) of 4.27% to 14.2% in Figure 7d.

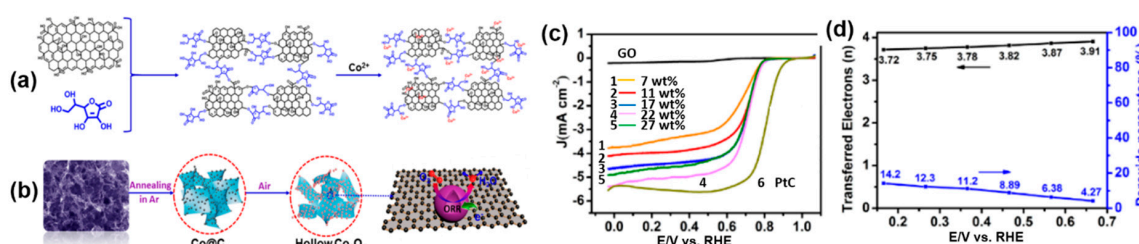


Figure 7. (a) Schematic representation of how an excess of ascorbic acid reduced graphene oxide (GO) and formed 3DG (three-dimensional graphene). The added Co^{2+} are anchored on 3DG; (b) Schematic showing the formation of HNPs (hollow nanoparticles) Co_3O_4 /3DG material; (c) LSVs (cathodic sweep) curves of GO, Co_3O_4 /3DG (with various weight loading) and Pt/C electrodes in O_2 -saturated 0.1 M KOH electrolyte at 5 mV s^{-1} at 1600 rpm; (d) the transferred electrons and peroxide percentage of Co_3O_4 /3DG (22 wt%). Reproduced from [81], Copyright © Wiley, 2017.

Wang et al. [82] developed a supramolecular gel-assisted method to manufacture N-doped carbon shell coated Co@CoO nanoparticles on carbon Vulcan XC-72 (Co@CoO@N-C/C) for ORR. Herein, melamine not only acted as a chelating agent interacting with Co^{2+} , but also as a nitrogen source to dope at high-temperature pyrolysis treatment. Due to the synergistic effect, the double-shelled Co@CoO@N-C/C nanoparticles displayed the excellent ORR performance with $E_{\text{onset}} = 0.92 \text{ V}$ vs. RHE and $E_{1/2} = 0.81 \text{ V}$ vs. RHE, comparable with the commercial Pt/C in 0.1 M KOH.

2.5. Oxygen Reduction on Cobalt-Based Layered Double-Hydroxides Catalysts

Synthesis Strategy

Layered double hydroxides (LDHs), a class of two-dimensional (2D) layered material, consist of host sheets with divalent (M^{II}) and trivalent (M^{III}) metal cations coordinated to hydroxide anions, and the guest anions in the interlayer regions. This kind of structure has attracted interest in various energy conversion systems [31]. Generally, hydroxides have a good affinity to aqueous electrolytes and their layered structures offer an enlarged surface area and improved dispersion degree based on the confinement effect. This latter property favors the accessibility of catalytic sites. Nevertheless, the positively charged host sheets in LDHs favor the oxygen adsorption and its oxygen reduction. Currently, Co-containing LDHs, as ORR catalysts, have been the object of intense research [83–85]. For instance, Li et al. [85] investigated the interaction of LDHs with RGO toward the ORR via a four-electron transfer pathway and found that the Co^{2+} in the LDHs, as active sites, catalyzed the disproportionation of the peroxide species to form H_2O and O_2 . Additionally, the RGO support increased the electrical conductivity.

Apart from the direct preparation of the LDHs precursor, the materials derived from LDHs, after thermal treatment, showed similar promising electrocatalytic activity in alkaline solution. For example, $\text{Co}_3\text{Mn}-\text{CO}_3\text{-LDH}/\text{RGO}$ precursor was calcined to produce reduced graphene oxide supported Co–Mn oxides under nitrogen atmosphere with enhanced catalytic performance ($E_{\text{onset}} = 0.95$ V vs. RHE, $E_{1/2} = 0.76$ V vs. RHE, and $j_{\text{limit}} = 4.2$ mA cm⁻² at 0.2 V vs. RHE, 1600 rpm) [84]. Similarly, $\text{Co}_3\text{O}_4/\text{Co}_2\text{MnO}_4$ composites, resulting from CoMn–LDHs precursor, displayed excellent bifunctional activities for ORR and OER with $\Delta E = 1.09$ V.

Herein, the activity of the material was attributed to the large specific surface area and well-dispersed heterogeneous structure [83]. Xu et al. [86], on the other hand, fabricated a Co/CoO/CoFe₂O₄ as ORR electrocatalyst based on the utilization of CoFe–LDHs as precursor by separate nucleation and aging steps (SNAS). The same group later reported Co@N–CNTs obtained by calcination of melamine/CoAl–LDH mixture, cf. Figure 8 [32]. Here, the CoAl–LDH precursor operated as: (i) catalyst for carbonization and formation of N–CNTs; (ii) detacher of active Co nanoparticles from the Co component in the host sheet; (iii) enabler for the growth of long N–CNTs with the aid of the confinement effect of non-active Al₂O₃ matrix formed.

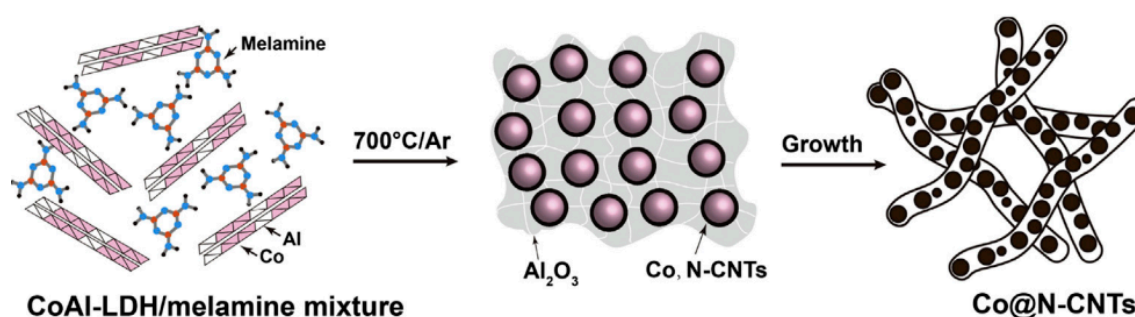


Figure 8. Representation of Co@N–CNTs–m resulting from CoAl–layered double hydroxides (LDH)/melamine mixture. Reproduced from [32], Copyright © Elsevier, 2016.

2.6. Oxygen Reduction on Co–N_x/C Catalysts

2.6.1. Co–N_x Active center

Besides the aforementioned Co-based electrocatalysts, Co–N_x/C has also been considered as another potential candidate to substitute Pt for ORR. In 1964, Jasinski [87] for the first time found that cobalt–phthalocyanine (CoPc) activated the ORR process in alkaline electrolyte. However, the catalytic sites in macrocyclic cathode catalysts for ORR are still controversial. Apropos Co–N_x/C catalysts, various type of active sites were proposed, including Co–N₄/C and Co–N₂/C [88–92], N_xC_y [93], pyridinic N [91,94], and graphitic N [95,96]. For example, Kiefer et al. [97] explained the origin and mechanism of ORR on Co–N_x ($x = 2, 4$) based on self-assembled carbon supported electrocatalysts in alkaline and acidic media via first-principle DFT calculations. The graphitic Co–N₄ defect was energetically more favorable than the graphitic Co–N₂ defects, and the former was predicted to be the dominant in-plane graphitic defect in Co–N_x/C electrocatalysts.

Nevertheless, Li et al. [98] believed that the dominant reactive sites for cobalt single atoms (Co–SAs) in Co–SAs/N–C could be postulated as Co–N₄ and Co–N₂ moieties, and Co–N₂ species had a stronger interaction with peroxide than Co–N₄, promoting the ORR four-electron reduction process. Tang et al. [99] considered that both of Co–N_x and pyri–N species were very important and their coupling effect (Co–pyri–N) was of paramount importance in the high electrocatalytic activity due to the high lying HOMO energy levels. Besides, Liao et al. [100] proposed that doped transition metals could act, on one hand, as a catalyst for the formation of stable active sites in the pyrolysis process, and on the other hand, the residual metal compounds could serve as active sites. In fact, the ORR catalytic performance improvement of transition metals might be the result of joint effects: (i) the overall N content/active N content; (ii) metal residue; and (iii) the surface area and pore structures. Metal-free

carbon structure was originally suggested as active sites by Wiesener [101]. Yet, Masa et al. [102] argued for the concept of a metal-free catalyst. Indeed, truly metal-free nitrogen-doped carbon demonstrated much lower ORR activity and reduced O_2 through a two-electron pathway in acidic solution, so that undetectable metal residues may play a crucial role for the ORR.

2.6.2. Co-N_x Synthesis Strategy

Generally, the electrocatalytic activity and stability of Co-N_x/C, or nitrogen-modified carbon supports (NCSs) or templates materials, basically rely on the morphology, pore structure, dispersion of the active sites, and nitrogen species, which are up to the crucial synthetic route. Traditional methods involving the pyrolysis of carbon-supported cobalt N₄-macrocycles, e.g., phthalocyanine (Pc), tetra-azaannulene (TAA), tetra-phenylporphyrin (TPP) and tetra-methoxyphenylporphyrin (TMPP), at temperatures between 550 °C and 800 °C preserved or created Co-N_x active sites, although the macrocyclic structure of the complex was partially or completely destroyed [103–106]. Above 800 °C, the metal–nitrogen species are known to decompose with a concomitant decrease in the ORR performance. For example, Popov et al. [107] found, via EXAFS, that the content of Co–N species decreased when the heat treatment exceeded 800 °C. Yet, Dodelet's group [108] proposed that Co metal and/or CoPc fragments containing Co could be responsible for the catalytic activity of CoPc/XC-72 pyrolyzed at 600 or 700 °C, a treatment where the maximum of the electrocatalytic activity was obtained [109]. Jahnke et al. [110] improved the stability as well as the electrochemical activity of transition metal porphyrins deposited on carbon support by a pyrolytic treatment step in the range of 450 to 900 °C, in an inert atmosphere. Qiao et al. [35] synthesized carbon-supported cobalt catalysts, namely, Py–CoPc/C, heat-treated at 600–900 °C, and investigated its heat-treatment effect onto the ORR activity in alkaline electrolyte. The catalysts that annealed at 700 °C exhibited the best activity towards ORR in 0.1 M KOH. Such a phenomenon was related with Co-N_x/C, pyridinic-N and graphitic-N active sites. Shan et al. [111] fabricated novel mesoporous Co-N_x-C, by a nanocasting-pyrolysis method, using Co-phenanthroline as the only precursor, permitting that abundant Co-N_x moieties remained embedded in the graphitic framework during pyrolysis.

Recently, most Co-N_x/C catalysts were fabricated by pyrolysis treatment of Co salts mixed with carbon support and nitrogen-rich precursor [100]. Zelenay et al. [88] used polyaniline (PANI) as a nitrogen source for high-temperature synthesis of catalysts incorporating iron or cobalt centers. The most active catalysts: FeCo/N/C, showed a very positive onset potential of ~0.93 V with a long-term stability test of 700 h at a fuel cell voltage of 0.4 V in 0.5 M H₂SO₄. Zhang et al. [112] demonstrated the direct utilization of the intrinsic structural defects in nanocarbon to generate atomically dispersed Co-N_x-C active sites via defect engineering. The as-obtained Co/N/O tri-doped graphene mesh (denoted as NGM-Co) were prepared via the carbonization of a mechanical mixture of gelatinized amylopectin, melamine, cobalt nitrate, and in situ generated Mg(OH)₂ nanoflakes. The remarkable bifunctional electroactivity for ORR and OER in alkaline medium of NGM-Co catalyst was ascribed to Co-N_x-C moieties, nitrogen-doping, oxygen functional groups, and topological defects. Miao et al. [113] reported a noble-free Co-N-C catalyst, derived from cobalt-phenanthroline complexes on CMK-3 under heat-treatment. By careful examination of the Co-N-C catalyst with sub-Ångström-resolution aberration-corrected scanning transmission electron microscopy (HAADF-STEM), the authors suggested that the Co single atoms bonded to N within the graphitic sheets served as the active sites. Wang's group [114] developed a new type of Co-N/C catalysts that contained two forms of active components, namely, coordinating cobalt moieties (CoC_xN_y or CoN_x) and Co nanoparticles encapsulated in mesoporous N-doped carbon hollow spheres (Co-N-mC) by pyrolyzing the polystyrene@polydopamine-Co (PS/PDA-Co) precursor. The Co-N-mC catalysts revealed striking ORR performance, comparable with commercial Pt/C, with onset potential of 0.94 V vs. RHE, half-wave potential of 0.851 V vs. RHE, and a Tafel slope of 45 mV dec⁻¹ in 0.1 M KOH. Similarly, Tsiakaras et al. [115] designed and fabricated a 3D hollow carbon spheres (HCS) with co-doping of cobalt and nitrogen, using dopamine and poly-methyl-methacrylate

(PMMA) as a template and a vacuum-assisted impregnation method, Figure 9a. The Co-N@HCS catalyst with a large specific surface area ($347.3 \text{ m}^2 \text{ g}^{-1}$) displayed excellent catalytic activity for both ORR and OER with a ΔE ($\Delta E = E_{\text{OER}, j@10 \text{ mA cm}^{-2}} - E_{1/2, \text{ORR}}$) of 0.856 V, much lower than those of the N@HCS (1.233 V) and the benchmark Pt/C catalysts (1.044 V).

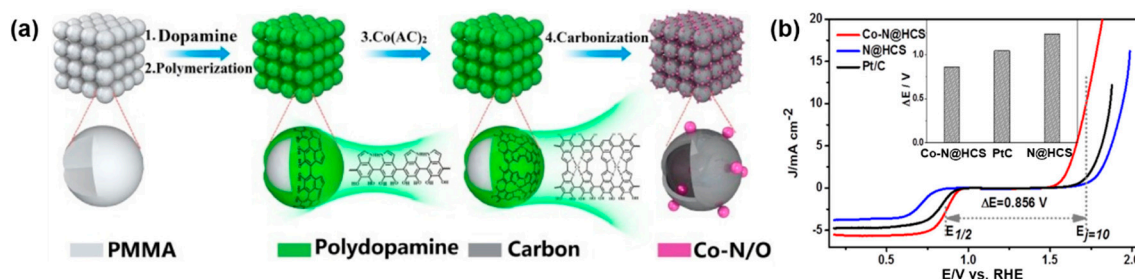


Figure 9. (a) The schematic chemical synthesis route of Co-N@HCS catalyst; (b) the LSV curves within ORR (cathodic sweep) and OER (anodic sweep) potential window of Co-N@HCS, N@HCS and Pt/C catalysts in O_2 -saturated 0.1 KOH at a rotation speed of 1600 rpm with a mass loading of 0.3 mg cm^{-2} . Inset: the comparison of the ΔE values. Reproduced from [115], Copyright © Elsevier, 2017.

Besides, more recently, some new synthesis strategies have been proposed to precisely control and fabricate the Co-N_x catalytic materials, under the confinement effect, with well-engineered nanostructure derived from metal-organic framework precursors (MOFs). The $\text{Co-N}_x/\text{C}$ catalysts synthesized by a simple pyrolysis of MOF precursor, inherited the large surface area and satisfactory porosity of MOFs, which led to dense active sites on the surface of materials. Feng's group [28] fabricated the $\text{Co}/\text{CoN}_x/\text{N-CNT}/\text{C}$ electrocatalysts by heat treatment of MOF (Co-mela-BDC) at different temperatures under N_2 atmosphere. The $\text{Co}/\text{CoN}_x/\text{N-CNT}/\text{C}$ catalyst obtained at 800°C contained N-doped carbon nanotubes, which were generated by the catalysis of cobalt species. Owing to the synergistic effect between $\text{Co-N}_x\text{-C}$ and NCNTs, the $\text{Co}/\text{CoN}_x/\text{N-CNT}/\text{C}$ composite boosted the much higher ORR performance. Aijaz et al. [116] reported highly active bifunctional electrocatalysts for oxygen electrodes containing core-shell $\text{Co@Co}_3\text{O}_4$ nanoparticles embedded in CNT-grafted N-doped carbon-polyhedra from the pyrolysis of ZIF-67, involved in the sequential reduction and oxidation steps. The use of ZIF-67, as sacrificial precursor, was advantageous to build a core-shell nanostructured polyhedral with large surface area, and high dispersion of Co-N_x and $\text{Co}_3\text{O}_4\text{-N}_x$ active sites. Furthermore, Zheng et al. [117] developed a bimetal (Cu and Co) embedded N-doped carbon framework, using the in situ growth of ZIF-67 polyhedrons on $\text{Cu}(\text{OH})_2$ nanowires, followed by pyrolysis treatment, Figure 10. The pyrolytic decomposition proceeded successively for $\text{Cu}(\text{OH})_2$ and ZIF-67, and thus the hierarchical porosity of ZIF-67 enabled the confinement of Cu nanocrystals and particles' size. The authors proposed that the existence of Cu ions not only provided extra active sites, but also led to an increased nitrogen content in the carbon frameworks via Cu-N coordination, optimized porous structure and large specific surface area, favorable to enhance the ORR electrocatalytic activity, Figure 10b. The CuCo@NC material showed an outstanding ORR activity, with much more positive $E_{\text{onset}} = 0.96 \text{ V}$ and $E_{1/2} = 0.88 \text{ V}$, comparable to commercial 30% Pt/C (1.04 V and 0.84 V, for E_{onset} , and $E_{1/2}$, respectively).

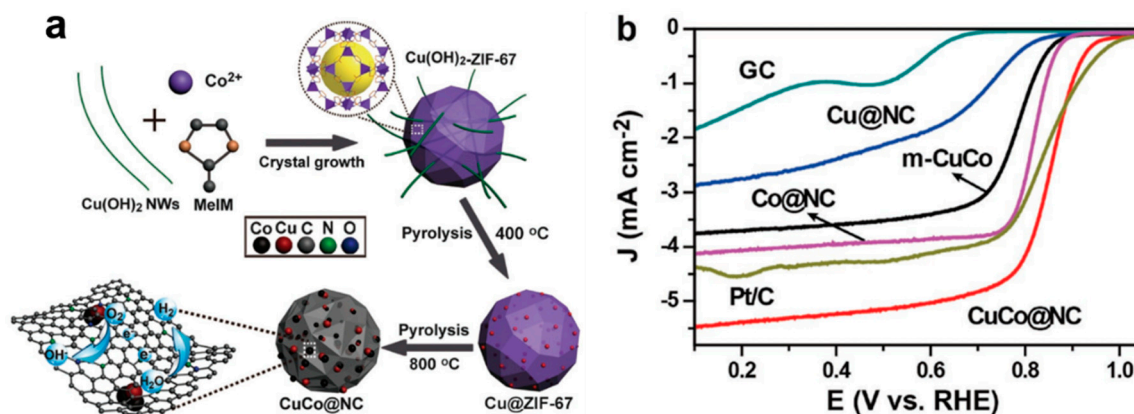


Figure 10. (a) The chemical synthesis route of Co-N@HCS catalyst; (b) ORR current-potential characteristics on (Cu and Co) embedded N-doped carbon materials in O₂-saturated 0.1 M KOH solution at a scan rate of 10 mV s⁻¹ and rotation speed of 1600 rpm (cathodic sweep) at room temperature (25 ± 1 °C). The catalyst loadings of all samples were 0.182 mg cm⁻². Reproduced from [117], Copyright © Wiley, 2017.

Because of some interesting properties, such as, tunable chemical composition, permanent porosity, and a high thermal/chemical stability, the porous covalent networks (PCNs), also known as covalent organic frameworks (COFs), are chemical precursors of interest for electrocatalysis. In this context, Bu et al. [118] proved that the porphyrinic conjugated network PCN-FeCo/C, a carbonized product of heterometalporphyrinic PCN-FeCo at 800 °C, showed a spectacular ORR activity and electrochemical stability in alkaline and acid electrolytes, Figure 11. The PCN-FeCo/C electrode displayed a very positive onset potential (1.00 V vs. RHE), and a half-wave potential of 0.85 V vs. RHE comparable to that of Pt/C (0.84 V vs. RHE) in 0.1 M KOH. Again, the binary PCN-FeCo/C catalyst was found to give the highest activity, i.e., the most positive $E_{\text{onset}} = 0.90$ V vs. RHE, and $E_{1/2} = 0.76$ V vs. RHE in 0.1 M HClO₄ solution. The prominent performance of PCN-FeCo/C was attributed to the high homogeneity of active components derived from ordered distribution of Fe and Co covalent network, i.e., a generated hierarchical porosity.

Table 1. Selected Co-based catalyst for the oxygen reduction reaction.

Catalysts	Mass Loading (mg cm ⁻²)	Electrolyte	RPM (rpm)	j_k (mA cm ⁻²)	$E_{1/2}$ (V/RHE)	Tafel Slope (mV dec ⁻¹)	Refs.
Cubic CoSe ₂ /NCNH ^a	0.214	0.1 M KOH	1600	8.1 @ 0.8 V	0.81	52	[66]
Hexagonal CoSe/N-RGO ^b	0.286	0.1 M KOH	1600	2.9 @ 0.85 V	0.86	56	[67]
Co ₃ C-GNRs ^c	-	0.1 M KOH	1600	4.6 @ 0.5 V	0.77	41	[119]
Cubic CoSe ₂ /XC-72 Vulcan	0.1	0.5 M H ₂ SO ₄	2000	0.1 @ 0.8 V	-	113	[120]
Cubic CoSe ₂ /XC-72 Vulcan	0.22	0.1 M KOH	1600	-	0.71	-	[61]
Co _{1-x} S/RGO	0.285	0.1 M KOH 0.5 M H ₂ SO ₄	1600	3.8 @ 0.7 V 1.1 @ 0.7 V	0.75 0.59	-	[18]
Co _{1-x} S/N-S-G ^d	0.5	0.1 M KOH	1600	15% higher than Pt/C @ 0.6 V	0.86	58	[121]
Co _{1-x} S/SNG/CF ^e	0.153	0.1 M KOH	1600	4.3 @ 0.2 V	0.83	85	[122]
Co-S/NS-RGO ^f	0.38	0.1 M KOH	900	-	0.81	-	[123]
CoS ₂ /NS-GO	0.25	0.1 M KOH	1600	7.7	0.79	30	[124]
CoS ₂ /XC-72	0.1	0.1 M KOH	1600	4.2 @ 0.4 V	0.71	73	[46]
Co ₃ S ₄ /G ^g	0.051	0.1 M KOH	1600	4.5 @ -1.1 V (vs. Ag/AgCl)	-	-	[125]

Table 1. Cont.

Catalysts	Mass Loading (mg cm ⁻²)	Electrolyte	RPM (rpm)	j_k (mA cm ⁻²)	$E_{1/2}$ (V/RHE)	Tafel Slope (mV dec ⁻¹)	Refs.
Co ₃ S ₄ nanosheets	-	0.1 M KOH	1600	-	-0.19 (vs. Hg/HgO)	-	[126]
Co ₃ S ₄ /C	0.011	0.5 M H ₂ SO ₄	1600	-	0.26	-	[60]
Co ₉ S ₈ /G	0.6	0.5 M H ₂ SO ₄	1600	3.7 @ -0.1 V (vs. Ag/AgCl)	-0.11 (vs. Ag/AgCl)	52	[127]
Co ₉ S ₈ /N-S-C ^h	0.1	0.1 M KOH	1600	-	0.90	74	[128]
Hollow Co ₉ S ₈ microspheres	0.61	0.5 M H ₂ SO ₄	1600	-	~0.18	-	[129]
Co ₉ S ₈ /N-S-G ₃ C ₃ N ₄	0.612	0.1 M KOH	1600	-	-0.10 (vs. Ag/AgCl)	-	[130]
Co ₃ O ₄ /N-rmGO ⁱ	0.24	0.1 M KOH	1600	5.0 @ 0.4 V	0.83	42	[25]
Co@N-CNTs-m ^j	0.6	0.1 M KOH	1600	6.0	0.85	-	[32]
Co-S/G-3	0.08	0.1 M KOH	1600	7.0 @ 0.85 V	0.83	38	[80]
Co ₃ O ₄ -SP/NGr-24h ^k	-	0.1 M KOH	1600	-	0.82	76	[75]
Co@CoO@N-C/C	-	0.1 M KOH	1600	-	0.81	69	[82]
Co ₃ O ₄ /N-RGO-3	0.1	0.1 M KOH	1600	5.24	0.82	55	[76]
L ₁ G ₅ ^l CoAl-LDHs/RGO	0.255	0.1 M KOH	1600	5.1 @ 0.2 V	0.71	-	[85]
CoPc/C	0.071	0.1 M KOH	1500	-	0.03 (vs. SHE)	62	[35]
NGM-Co	0.25	0.1 M KOH	1600	-	-	58	[112]
Co-N-mC	0.285	0.1 M KOH	1600	4.5 @ 0.8 V	0.85	45	[114]
Co-N@HCS ^m	0.3	0.1 M KOH	1600	4.8 @ 0.8 V	-	56	[115]
MOFs-800	0.335	0.1 M KOH	1600	3.7 @ 0.7 V	0.80	42	[28]
Co@Co ₃ O ₄ /NC-1	0.21	0.1 M KOH	1600	-	0.80	92	[116]
CuCo@NC	0.182	0.1 M KOH	1600	4.4 @ 0.8 V	0.88	80	[117]

j_k : kinetically current density; $E_{1/2}$: half-wave potential. ^a NCNH, N-doped carbon nanohorns; ^b N-RGO, N-doped reduced graphene oxides; ^c GNRs, graphene nanoribbons; ^d N-S-G, N, S-doped graphene; ^e CF, carbon fiber; ^f NS-RGO, N, S-doped reduced graphene oxides; ^g G, graphene; ^h N-S-C, N, S-doped carbon; ⁱ N-rmGO, N-doped reduced mildly graphene oxides; ^j N-CNTs-m, N-doped carbon nanotubes mixture; ^k NGr-24h, N-doped graphene; ^l L₁G₅, the mass ratio of LDHs/GO (1:5); ^m HCS, hollow carbon spheres.

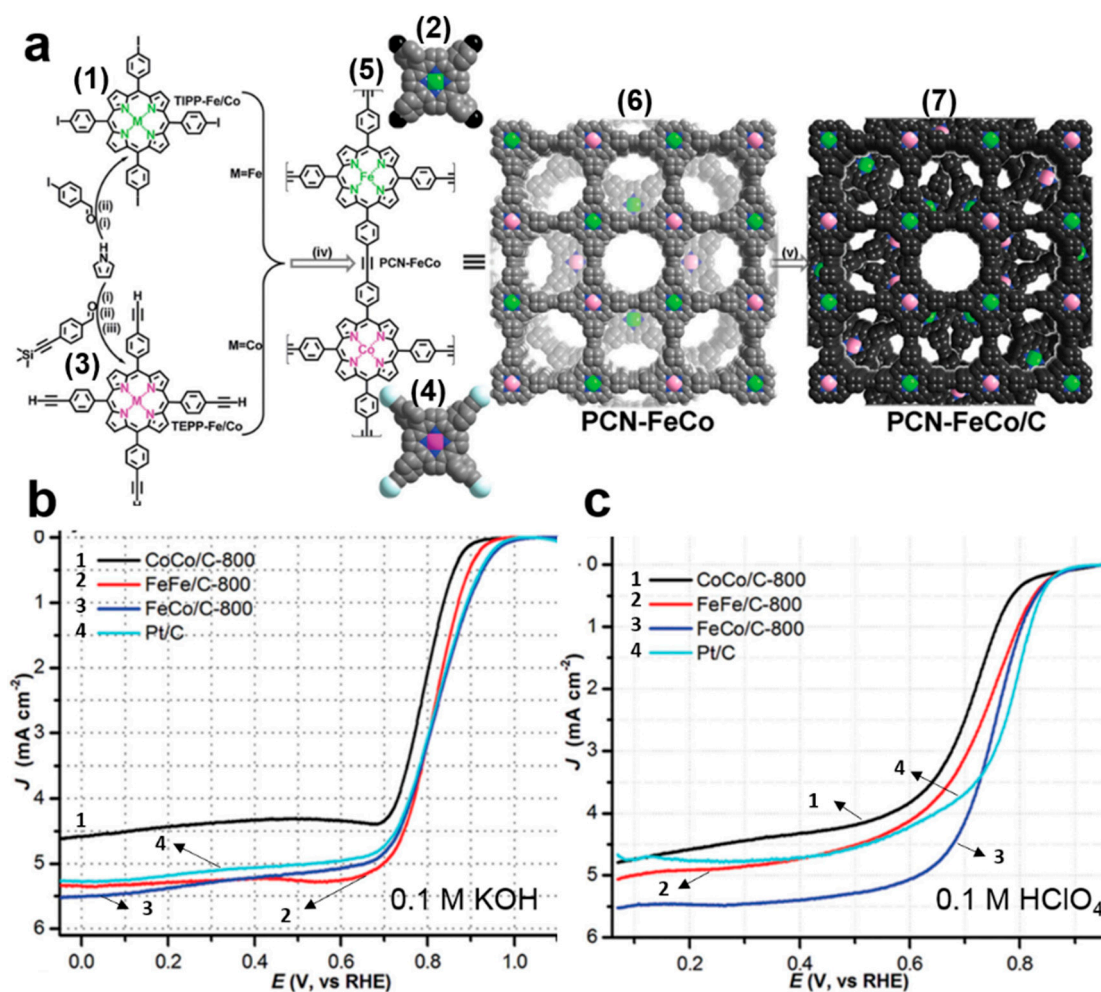


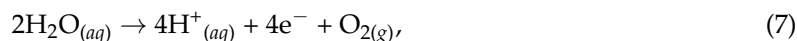
Figure 11. (a) Synthesis representation of porous covalent network (PCN)-FeCo/C by carbonization. Monomers: (1,2) TIPP-M, and (3,4) TEPP-M (M = Fe, Co). (5,6) porphyrinic conjugated network PCN-FeCo, and (7) the PCN-FeCo/C product. The reagents and conditions were: (i) propionic acid, reflux, 3 h; (ii) $\text{Co}(\text{OAc})_2 \cdot 4\text{H}_2\text{O}$ or $\text{FeCl}_2 \cdot 4\text{H}_2\text{O}$, $\text{CHCl}_3 \cdot \text{CH}_3\text{OH}$, reflux, 12 h; (iii) tetrabutylammonium fluoride (TBAF), $\text{THF} \cdot \text{CH}_2\text{Cl}_2$, at R.T. 1 h; (iv) $\text{Pd}_2(\text{dba})_3$, AsPh_3 , $\text{THF}/\text{Et}_3\text{N}$, 50°C , 72 h. TIPP stands for: 5, 10, 15, 20-tetrakis (4-iodophenyl) porphyrin, and TEPP for: 5, 10, 15, 20-tetrakis (4-ethynylphenyl) porphyrin; (b) ORR current-potential curves on PCN/C and 20% Pt/C (Alfa) at 1600 rpm (cathodic sweep) in O_2 -saturated 0.1 M KOH solution, with the catalyst loading on PCN/C electrode of 0.2 mg cm^{-2} and on Pt/C electrode of 0.1 mg cm^{-2} ; (c) in O_2 -saturated 0.1 M HClO_4 with the catalyst loading on PCN/C electrode of 0.6 mg cm^{-2} and on Pt/C electrode of 0.1 mg cm^{-2} . Reproduced from [118], Copyright © Wiley, 2015.

3. Electrocatalysts for Oxygen Evolution Reaction (OER)

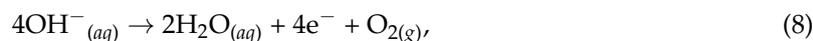
3.1. Mechanistic Approach of OER

OER kinetics are also a multi-electron charge transfer process in acid and alkaline media. The kinetic parameters such as overpotential (η), exchange current density (i), Tafel slope (b), turnover frequency (TOF), and so on, are employed to evaluate the OER performance of electrocatalytic materials. Particularly, the overpotential at a current density of 10 mA cm^{-2} is a crucial criterion to examine the OER performance (indicated as $\eta_{@10}$). These parameters play a key role for obtaining an insight into the mechanism of this electrocatalytic process. In general, the electrochemical reaction that occurs at the anode (OER) in acid, and alkaline electrolytes are:

Acid medium:

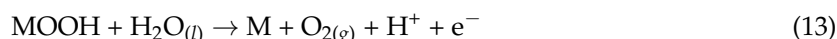
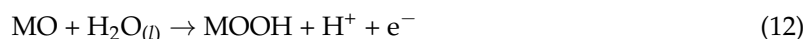
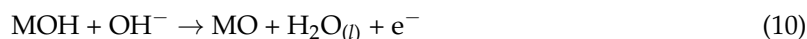


Alkaline medium:



Various research groups have proposed possible OER mechanisms in acid (Equations (9)–(13)) and alkaline medium (Equations (14)–(18)). Most of the proposed mechanisms involve MOH and MO intermediates. The diagram in Figure 12 displays two different routes to form oxygen from a MO intermediate. One, the green route, via the direct combination of 2MO to produce $\text{O}_{2(g)}$ (Equation (11)), and that involving the generation of the MOOH intermediate (Equations (12) and (17)) which subsequently decomposes, black route, to $\text{O}_{2(g)}$ (Equations (13) and (18)). During the heterogeneous OER process, all the bonding interactions (M–O) within the intermediates (MOH, MO and MOOH) are crucial to determining the overall electrocatalytic performance.

Acid medium:



Alkaline medium:

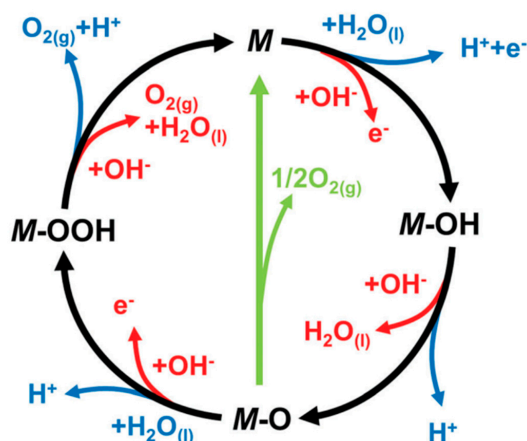
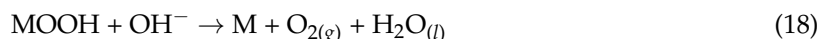
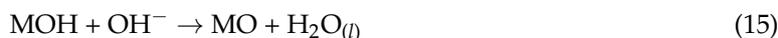


Figure 12. The oxygen evolution reaction (OER) mechanism in acid (blue line) and alkaline (red line) medium. Two reaction routes of oxygen evolution take place: (1) black line indicates that the process involves the formation of a peroxide (M–OOH) intermediate; (2) green line indicates that the direct reaction of two adjacent oxo (M–O) intermediates to produce molecular oxygen. Reproduced from [4], Copyright © Royal Society of Chemistry, 2017.

Until now, the Ni- and Co-based materials (both free support and supported on, e.g., carbon) have been intensively investigated as promising non-precious OER electrocatalysts. The catalysts derived from cobalt metal centers can activate the OER in alkaline medium rather than in acid medium. Particularly for CoO_x and CoOOH , the nature of their OER activities, stabilities in alkaline solution and OER mechanism have been thoroughly investigated [131–133]. For example, Mattioli group [131] provided insightful information into the pathways towards oxygen evolution of a cobalt-based catalyst (CoCat) by performing ab initio DFT + U molecular dynamics calculations of cluster models in water solution. The reaction pathways of CoCat were proposed as follows: (1) the fast H^+ mobility at the CoCat/water interface is responsible for an optimal distribution of terminal Co(III)-OH groups, as sites of injected holes. These sites are preferred in the case of complete cubane units; (2) the oxygen evolution process starts with the release of a proton from one of such terminal Co-OH sites, a process favored by the proton-acceptor species in solution, leading to the formation of a Co(IV)=O^\bullet oxyl radical; (3) the coupling of Co=O radicals with germinal (i.e., bonded to the same Co atom) Co-OH or $\text{Co-}\mu\text{O-Co}$ groups to form hydroperoxo and peroxo intermediates.

3.2. Oxygen Evolution on Cobalt Chalcogenides Catalysts

3.2.1. Synthesis Strategy

One of the attractive electrocatalysts surface engineering strategies, e.g., etching and edging, could greatly improve the catalytic performance. Dai et al. [19], for the first time, developed an novel bifunctional oxygen electrode catalysts by using NH_3 -plasma to simultaneously etch and dope the cobalt sulfides-graphene hybrid ($\text{N-Co}_9\text{S}_8/\text{G}$). NH_3 -plasma treatment, not only could induce the N doping into both Co_9S_8 and graphene to enhance the activity, but also realized etching on the surface to expose more active sites for electrocatalysis. The $\text{N-Co}_9\text{S}_8/\text{G}$ catalyst exhibited a low onset potential at ca. 1.51 V vs. RHE and a small Tafel slope of 82.7 mV dec^{-1} . Notably, the required overpotential of $\text{N-Co}_9\text{S}_8/\text{G}$ catalyst to reach the current density of 10 mA cm^{-2} was only 0.409 V in 0.1 M KOH. Additionally, Xie's group [134] proposed that reducing the thickness of bulk CoSe_2 into the atomic scale, rather than doping or hybridizing, was inclined to form a great deal of exposed active sites e.g., V_{Co} vacancies, which could effectively catalyze the OER process evidenced by the positron annihilation spectrometry, XAFS (X-ray Absorption Fine Structure) spectra and DFT calculations. The ultrathin CoSe_2 nanosheets with rich V_{Co} vacancies manifested an OER overpotential of 0.32 V at 10 mA cm^{-2} in alkaline electrolyte (pH = 13) much less than that of the bulk CoSe_2 .

3.2.2. Support Effect

Clear evidence of the strong metal-support interaction (SMSI) was given by Gao et al. [135] with synthesized CoSe_2 nanobelts on N-doped reduced graphene oxide (RGO) sheets. This system showed an exceptional OER activity and stability in alkaline environment, with a Tafel slope of 40 mV dec^{-1} and $\eta_{@10}$ (the overpotential required to achieve the current density of 10 mA cm^{-2}) of 0.366 V. The authors concluded that the high performance is dependent on the interaction between N-doped carbon domains and CoSe_2 nanobelts. Similarly, Liao et al. [121] embedded Co_{1-x}S hollow nanospheres in N and S co-doped graphene holes to create an efficient bifunctional catalysts ($\text{Co}_{1-x}\text{S}/\text{N-S-G}$) with hierarchical meso-macroporous structures for ORR and OER. The $\text{Co}_{1-x}\text{S}/\text{N-S-G}$ material with a large specific surface area ($390.6 \text{ m}^2 \text{ g}^{-1}$), showed a small overpotential of 371 mV for 10 mA cm^{-2} in 0.1 KOH, and the ΔE value is 0.706 V, which was much smaller than those of many reported non-precious metal catalysts. The investigated results demonstrated that the excellent bifunctional performance was mainly attributed to a synergistic effect of the multiple active sites consisting of Co_{1-x}S , N and S dopants, and possible Co-N-C sites. Interestingly, Guo et al. [136] used CoSe_2 nanosheets as support to grow Co_2B at room temperature. The resulting $\text{Co}_2\text{B}/\text{CoSe}_2$ hybrid catalysts showed $\eta_{@10}$ values for OER and HER in alkaline of 0.32 V, and 0.30 V, respectively. Apparently, CoSe_2

nanosheets supplied nucleation sites for Co_2B , as well as high electrical conductivity that promoted a high stability through water splitting reactions in alkaline medium.

3.3. Oxygen Evolution on Cobalt Oxides Catalysts

3.3.1. Mechanism of Cobalt Oxides

Cobalt (II) commonly undergoes the oxidation ($\text{Co}^{\text{II}} \rightarrow \text{Co}^{\text{III}}$) under an anodic potential prior to the OER in an aqueous solution, forming a layered oxidic cobalt species [137,138]. Some researchers pointed out that Co^{IV} species were generated on the outermost surface of the electrode [137,139]. So that the catalytic site formed on the Co_3O_4 electrode was the quasi-reversible redox couple $\text{Co}^{\text{III}}/\text{Co}^{\text{IV}}$ that accelerated the one-step or two-step OER [131,133,140,141]. In order to investigate the role of the peroxy process in the oxygen evolution reaction, Fu et al. [142] prepared ultrathin Co_3O_4 nanosheets (NSs) with abundant active centers with a large electroactive surface to gain an insight into the OER performance of Co_3O_4 NSs. The possible mechanism of Co_3O_4 nanosheets towards OER included essentially double two-electron steps: (1) oxidation of OH^- to OOH_{ads} (thermodynamic rate-limiting step); and (2) fast oxidation of the intermediate OOH_{ads} to O_2^{ads} by $\text{Co}^{\text{III}}/\text{Co}^{\text{IV}}$ surface redox couple (kinetic process), Figure 13. The apparent OER on Co_3O_4 NSs that proceeded via a four-electron pathway, corresponding to a double two-electron one, ascribed to $\text{Co}^{\text{III}}/\text{Co}^{\text{IV}}$ sites acting efficiently to oxidize the generated OOH_{ads} , and facilitating the formation of $\text{O}_{2,\text{ads}}$.

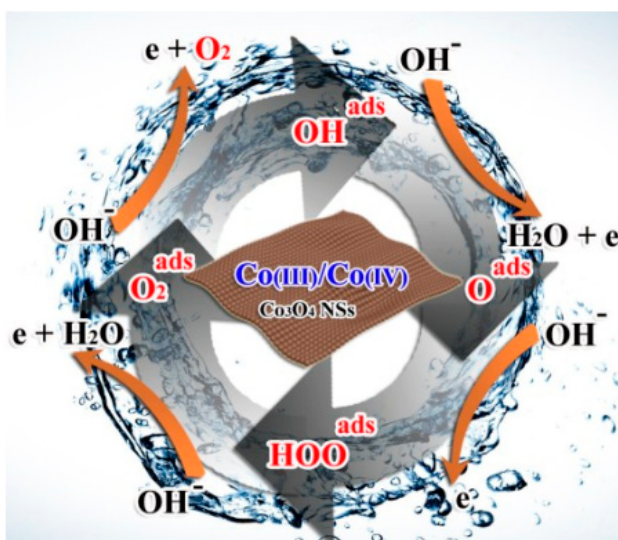


Figure 13. The scheme exemplifying the proposed OER electrocatalytic mechanism on Co_3O_4 NSs. Reproduced from [142], Copyright © Royal Society of Chemistry, 2016.

3.3.2. Chemical Composition

As mentioned above, the electrocatalytic performance of Co_3O_4 nanoparticles mainly depends on the surface area, the oxidation charge of the cobalt atoms, and the oxygen vacancies. Hence, a reasonable tuning of the surface electronic states of undoped Co_3O_4 can provide more electrochemically active sites to favor the OER. The preparation of mesoporous Co_3O_4 nanowires (Co_3O_4 NWs) by Zheng et al. [143], through a facile NaBH_4 reduction method led to seven-fold activity enhancement of OER, as compared to pristine Co_3O_4 , Figure 14. As shown in Figure 14a, the peak current density observed in the cyclic voltammetry curves increased dramatically, after the chemical reduction process, signifying the existence of more active sites as a result of the oxygen vacancies, confirmed by DFT calculations. The increased $\text{Co}^{4+}/\text{Co}^{3+}$ redox peaks (1.4–1.5 V) was ascribed to the formation of $[\text{Co}^{4+}-\text{O}]$ intermediate, involved in the turnover-limiting chemical step of oxygen evolution. The onset potential of the reduced Co_3O_4 NWs was ca. 1.52 V vs. RHE, i.e., ca. 50 mV

and 100 mV more negative than pristine Co_3O_4 NWs and Pt/C catalyst, respectively, Figure 14b. Besides reduction post-treatment, Xia et al. [144] fabricated 3D ordered mesoporous cubic Co_3O_4 implementing hard-templating strategies. X-ray photoelectron spectroscopy (XPS) analysis revealed that the molar surface ratio $\text{Co}^{\text{III+}}/\text{Co}^{\text{II+}}$ of ordered mesoporous Co_3O_4 was much lower than that of bulk-Co, suggesting more surface oxygen vacancies on the former, which benefited the adsorption and activation of molecular oxygen.

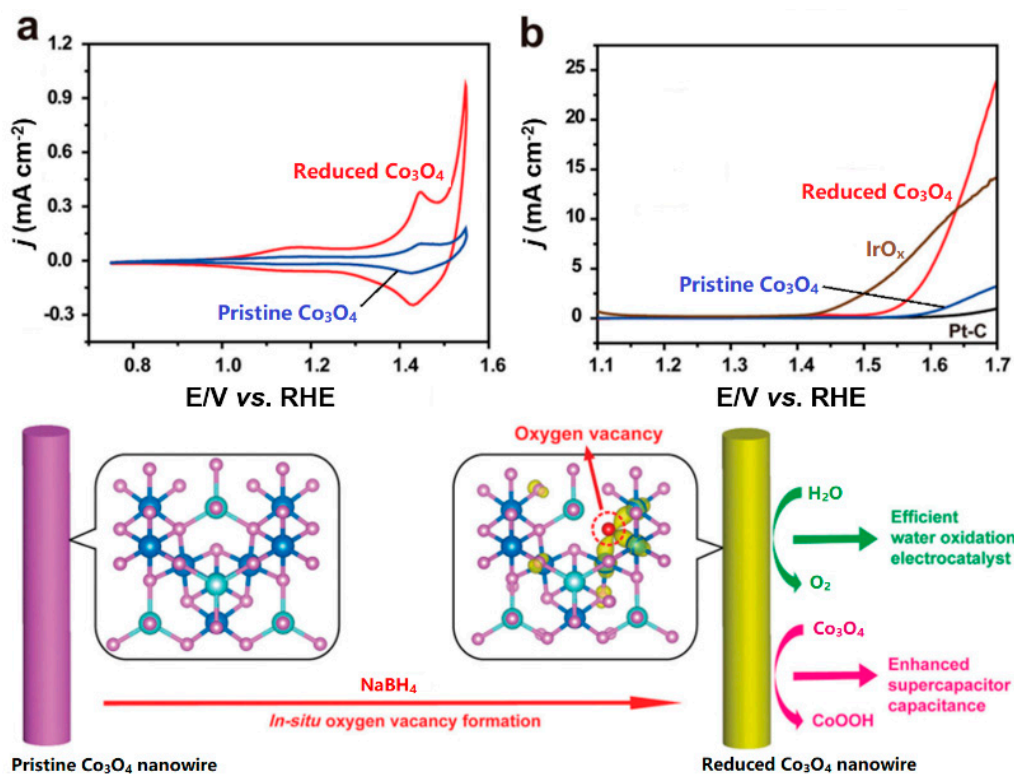


Figure 14. (a) Cyclic voltammograms of reduced Co_3O_4 , and pristine Co_3O_4 NWs deposited on glassy carbon electrodes in O_2 -saturated 1 M KOH at 5 mV s^{-1} ; (b) water oxidation current-potential characteristic of reduced Co_3O_4 NWs (red curve), pristine Co_3O_4 NWs (blue curve), IrO_x (brown curve) and Pt/C (black curve) in O_2 -saturated 1 M KOH at a scan rate 5 mV s^{-1} at 1600 rpm (anodic sweep) at $25 \pm 1^\circ \text{C}$ with iR -compensation. The catalyst mass loadings in all cases was 0.136 mg cm^{-2} ; The bottom panel shows the insitu chemical reduction via NaBH_4 to form oxygen vacancies in Co_3O_4 NWs. Reproduced from [143], Copyright © Wiley, 2014.

3.3.3. Synthesis Strategy

The synthesis of graphene- Co_3O_4 (G- Co_3O_4) composite having a unique sandwich-architecture was reported by Zhao et al. [145]. The large amount of tiny Co_3O_4 nanocrystals, uniformly dispersed on both sides of graphene sheets, allowed for a favorable electron transfer kinetics. The onset potential of G- Co_3O_4 was 0.406 V vs. Ag/AgCl in 1 M KOH, and 0.858 V vs. Ag/AgCl in neutral phosphate buffer solution (PBS). The overpotential at a current density of 10 mA cm^{-2} ($\eta_{@10}$) was 313 mV in 1 M KOH, and 498 mV in PBS, respectively. Kim et al. [146], on the other hand, used dextrose as chemical source to obtain mesoporous carbon, and urea together with $\text{CoCl}_2 \cdot 6\text{H}_2\text{O}$ in a hydrothermal treatment to obtain carbon-cobalt oxide-nanorods (C- Co_3O_4 -NRs). This latter provided an overpotential at a current density of 10 mA cm^{-2} ($\eta_{@10}$) of 415 mV, a value much lower than that of carbon free Co_3O_4 nanorods. The OER activity of the C- Co_3O_4 -NRs electrode was significantly increased with a low onset potential of 356 mV and Tafel slope of 53 mV dec^{-1} .

Additionally, materials with high conductivity and mobility, e.g., Co foil, Ni foam and carbon fiber paper, were employed as support grown on non-precious metal electrocatalysts to facilitate the

electrolyte diffusion, drive off the as-formed gas bubbles from the electrode surface during the oxygen evolution process, favoring the kinetics, and the chemical stability. In this connection, a simple and reasonable method to synthesize self-supported Co_3O_4 nanocrystal/carbon fiber paper via thermal decomposition of the $[\text{Co}(\text{NH}_3)_n]^{2+}$ -oleic acid complex and subsequent spray deposition was done by Fu et al. [147]. The Co_3O_4 NCs with a loading of 0.35 mg cm^{-2} showed a current density of 16.5 mA cm^{-2} at $\eta_{@10}$ of 350 mV in 1 M KOH. With the same perspective, Wei et al. [148] reported the synthesis of Co_3O_4 nanorods array on Co foil (Co_3O_4 NA/CF) oxygen-evolving catalyst using the so-called in situ self-standing method, Figure 15a. The 1D Co_3O_4 NA/CF OER material only needed $\eta = 308 \text{ mV}$ to drive a geometrical current density of 15 mA cm^{-2} in 1 M KOH, exceeding the value reported so far on Co_3O_4 -based electrocatalysts. The electrocatalyst delivered an excellent long-term durability of 22 h, and a turnover frequency of $0.646 \text{ mol O}_2 \text{ s}^{-1}$ at $\eta = 410 \text{ mV}$ in Figure 15b. The suggested OER high activity of Co_3O_4 NA/CF was thought to be the formation of Co^{III} (in an octahedral environment) on CoOOH as a result of Co_3O_4 oxidation. The surface Co^{III} -containing octahedral forms $\text{Co}^{\text{III}}\text{-OH}$, which was further oxidized to form the active catalytic center: $\text{Co}^{\text{IV}}\text{-O}$ for OER. A further coupling of $\text{Co}^{\text{IV}}\text{-O}$ with neighboring species formed hydroperoxo ($\text{Co}^{\text{IV}}\text{-OOH}$) to peroxo ($\text{Co}^{\text{IV}}\text{-OO}$) species, leading to the release of O_2 and initial Co^{III} , see scheme in Figure 15c.

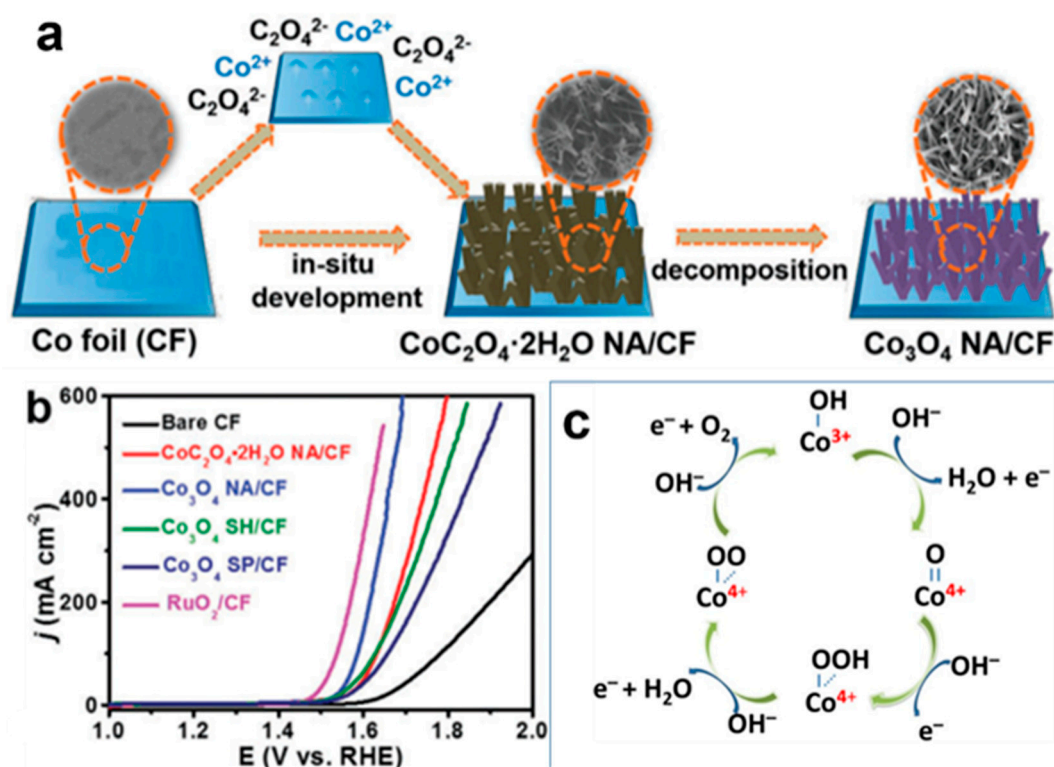


Figure 15. (a) Two-step manufacture of Co_3O_4 NA/CF; (b) LSV curves (anodic sweep) of RuO_2/CF , Co_3O_4 NA/CF, $\text{CoC}_2\text{O}_4 \cdot 2\text{H}_2\text{O}$ NA/CF, and bare Co catalysts in O_2 -saturated 1 M KOH at 5 mV s^{-1} at a rotation speed of 1600 rpm at 25°C . The constant catalyst loading was 1.9 mg cm^{-2} ; (c) Suggested OER mechanism on Co_3O_4 . Reproduced from [148], Copyright © Royal Society of Chemistry, 2018.

3.4. Oxygen Evolution on Cobalt-Based Layered Double-Hydroxides Catalysts

The use of LDH materials for OER has been recently promoted, see Table 2. Cobalt-containing LDHs composed of edge-sharing octahedral MO_6 layers, which are OER active sites, were successfully synthesized and showed an unusual catalytic activity and stability [149–151]. Li et al. [15] presented a strategy for a direct nucleation and growth of CoMn -LDH material on modified multiwall carbon nanotubes (MWCNTs) with three-dimensional hierarchical configuration. This approach afforded an intimate chemical and electrical coupling between LDH nanoplates and carbon materials, to allow

for a rapid electron charge transfer from the active sites to the support. By tuning Co/Mn ratio, the $\text{Co}_5\text{Mn-LDH/MWCNT}$ activated the reaction at a low overpotential of $\eta_{@10} \sim 300$ mV in 1 M KOH. Ren et al. [152] designed and synthesized randomly cross-linked CoNi-LDH/CoO via an in situ reduction and interface-directed assembly in air. Owing to the orbital hybridization between metal $3d$ and O $2p$ orbitals, and electron transfer between metal atoms through Ni-O-Co, some Co and Ni atoms in the CoNi LDH underwent a high +3 valence. For transition metals, highly oxidized redox couples, e.g., $\text{Co}^{4+/3+}$ and $\text{Ni}^{4+/3+}$ were considered as active centers for OER [153].

The specific activity of the material for the target reaction is usually highly dependent on the chemical composition and electronic structure. The higher conductivity induced by modifying the electronic structure of Co is applicable for the electrochemical catalysis, such as de-lithiated hexagonal LiCo_2 for OER, and spinel LiCo_2 for ORR [153]. For the OER, a small amount of Fe doping was effective for enhancing the OER activities of Ni hydroxides or oxides, possibly due to the enhanced structure disorder and conductivity. Inspired by this, Sun et al. [154] systematically investigated the ORR and OER activities of ternary NiCoFe-LDHs and observed that a peroxidation treatment of NiCoFe-LDHs led to obtain o-NiCoFe-LDHs that significantly enhanced the corresponding bifunctional performance of (ORR/OER), as shown in Figure 16a. The XPS results and Zeta potential measurements evidenced that Co^{2+} was partially oxidized to a higher Co^{3+} state, while negligible chemical state change of Ni and Fe elements was observed in o-NiCoFe-LDHs. The partial conversion of Co^{2+} to Co^{3+} state stimulated the charge transfer to the catalyst surface, which could lead to the enhancement of the conductivity. In the Figure 16b, in 6 M KOH medium, the o-NiCoFe-LDHs afforded a high ORR current density of -20 mA cm^{-2} at a required potential of 0.65 V vs. RHE. Moreover, there was a negligible ORR current density degradation of o-NiCoFe-LDHs for 40 h. The higher conductivity induced from the higher valence state of Co, might enhance the electrophilicity of the adsorbed O and thus facilitating the reaction of an OH^- anion with an adsorbed O atom on the catalytic active sites to form adsorbed $-\text{OOH}$ species, which was considered as the rate-limiting step for OER [138,155].

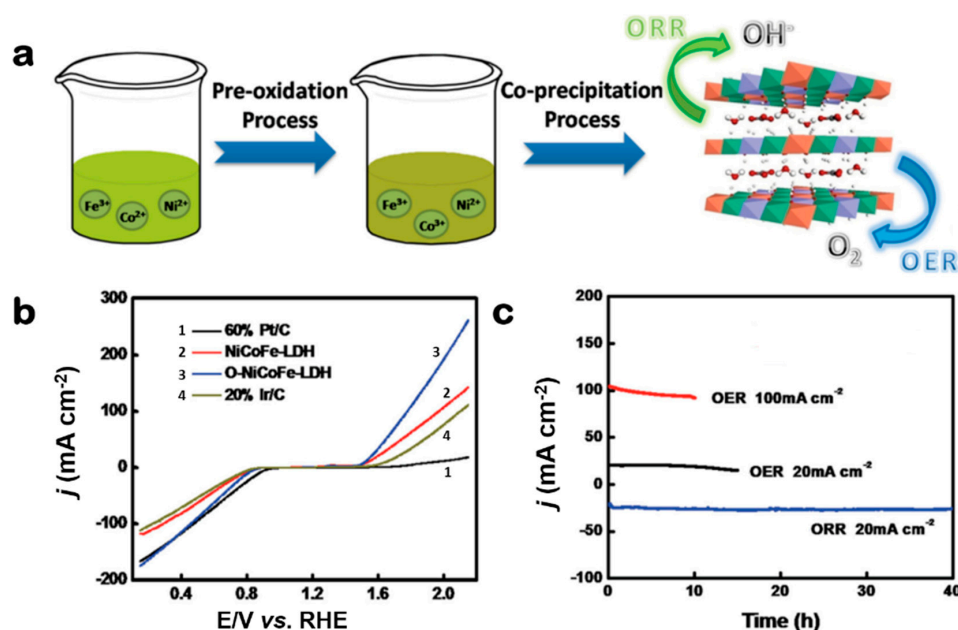


Figure 16. (a) Schematic chemical synthesis route and crystal structure of peroxidized ternary LDH bifunctional catalyst; (b) The global polarization curves of various catalysts loaded onto Teflon-treated carbon fiber paper (T-CFP) in O_2 -saturated 6 M KOH electrolyte with a scan rate of 1 mV s^{-1} , the mass-loading of 1 mg cm^{-2} without iR -compensation; (c) ORR (cathodic sweep) and OER (anodic sweep) stability measurements of o-NiCoFe-LDH/Y-CFP electrode in O_2 -saturated 6 M KOH electrolyte with a constant potential, the mass-loading of 1 mg cm^{-2} . Reproduced from [154], Copyright © Wiley, 2015.

It is fascinating to design and build a bifunctional oxygen electrode catalyst based on the combination of highly OER-active Ni–Fe hydroxides or oxides, and highly ORR-active Co, Fe-based compounds. Feng’s group [33] designed and obtained a bifunctional electrocatalyst based on $\text{NiFeO}_x/\text{Co-N}_y\text{-C}$ by a simple calcination of $\text{Ni}_2\text{Fe-CoPcTs-LDH}$ precursor based on the intercalation of cobalt phthalocyanine tetrasulfonate (CoPcTs) into $\text{Ni}_2\text{Fe-LDH}$ s under N_2 atmosphere at $600\text{ }^\circ\text{C}$. The key aspects of this bifunctional electrocatalyst, for the reversible oxygen electrode, was the mutual incorporation of the ORR-active centers (Co-based compound), and OER-active ones (spinel NiFe_2O_4). Particularly, the CoPcTs–intercalated structure and $\text{Ni}_2\text{Fe-LDH}$ host sheet significantly enhanced the immobilization of CoPcTs and improved the dispersion degree of catalytic sites, respectively.

Moreover, the surface area of lamellar architecture materials can be further enlarged by swelling and exfoliating into individually single layers by mechanical, chemical or electrochemical means [156–159]. The exfoliated single-layered nanosheets revealed significantly higher oxygen evolution activity than the corresponding bulk LDH in alkaline conditions. Hu et al. [159] inferred that the higher OER activities of exfoliated LDHs (CoCo, NiCo, and NiFe–LDH) were mainly attributed to the increase in the number of active edge sites and to higher electronic conductivity. Analogously, Jin et al. [160] selected NiCo LDH as a representative material to demonstrate the concept of the amplified influence of exfoliation using a newly developed high-temperature high-pressure hydrothermal continuous flow reactor (HCFR), see Figure 17. The major findings were presented as follows: (1) the utilized HCFR technology effectively maintain the supersaturation to control the morphology and size of the product; (2) the exfoliation not only resulted in thinner layers with reduced size, but it was also caused by a change in the electronic structure; (3) the increase in the number of edge sites to activate OER; and (4) the increase in the electrochemical active surface area (ECSA) upon the exfoliation was not the only important factor that led to the enhanced OER performance. This work provided a general strategy to enhance the electrocatalytic performance of layered materials by chemical exfoliation.

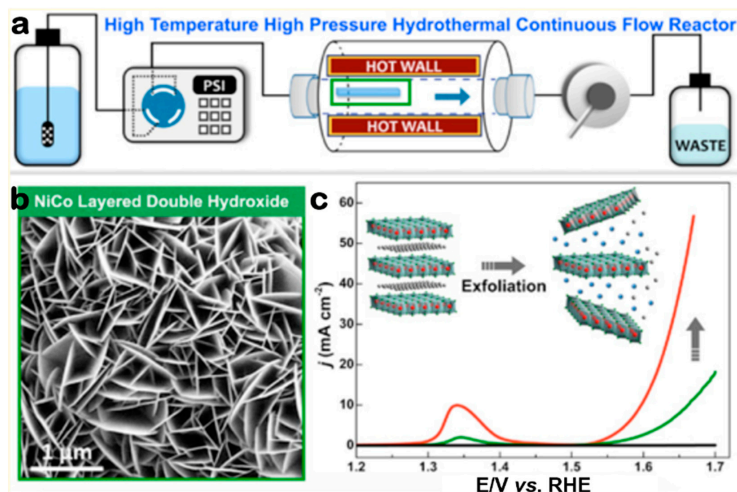


Figure 17. (a) The high-temperature high-pressure continuous flow reactor (HCFR) scheme; (b) scanning electron microscope (SEM) image of exfoliated NiCo LDH from HCFR; (c) iR -corrected and background subtracted polarization curves (anodic sweep) of NiCo LDH nanoplates (green curve) made of HCFR with mass catalyst loading of $\sim 0.23\text{ mg cm}^{-2}$, NiCo LDH nanosheets (red curve) synthesized nanoplates from exfoliated HCFR with a mass catalyst loading of $\sim 0.17\text{ mg cm}^{-2}$, and carbon paper (black curve) in O_2 -saturated 1 M KOH at a scan rate of 0.5 mV s^{-1} . All experiments were conducted at room temperature ($25\text{ }^\circ\text{C}$). Reproduced from [160], Copyright © American Chemical Society, 2015.

Table 2. Selected Co-based catalyst towards the oxygen evolution reaction.

Catalysts	Mass Loading (mg cm ⁻²)	Electrolyte	RPM (rpm)	<i>E</i> _{onset} mV vs. RHE	<i>η</i> @ 10 mA cm ⁻² (mV)	Tafel Slope (mV dec ⁻¹)	TOF (s ⁻¹)	Refs.
Nanobelts CoSe ₂ /N-doped RGO ^a	0.2	0.1 M KOH	1600	-	366	76	-	[135]
Co _{1-x} S/N-S-G ^b	0.5	0.1 M KOH	1600	-	371	63	-	[121]
N-Co ₉ S ₈ /G ^c	0.2	0.1 M KOH	1600	1.51	409	83	-	[19]
Co ₂ B/CoSe ₂	0.4	1 M KOH	-	-	320	56	-	[136]
Co ₃ O ₄ -NSs ^d	1.76	1 M KOH	1600	1.51	330	69	-	[142]
Reduced Co ₃ O ₄ NWs ^e	0.136	1 M KOH	1000	1.52	400	72	-	[143]
G-Co ₃ O ₄	0.189	1 M KOH	1600	0.41 vs. Ag/AgCl	313	56	0.45 @ 0.35 V	[145]
C-Co ₃ O ₄ -NRs ^f	0.142	1 M KOH	-	1.59	415	53	-	[146]
Co ₃ O ₄ NCs ^g	0.35	1 M KOH	-	1.52	350 @ 16.5 mA cm ⁻²	101	-	[147]
OA-Co ₃ O ₄ NCs	0.35	1 M KOH	-	1.55	-	118	-	[147]
Co ₃ O ₄ NA/CF ^h	1.9	1 M KOH	-	-	308 @ 15 mA cm ⁻²	71	0.65 @ 0.41 V	[148]
NiCo _{2.7} (OH) _x	0.2	1 M KOH	1600	1.48	350	65	0.18 @ 0.35 V	[149]
CoFe/C	-	1 M KOH	1600	1.45	300	61	-	[151]
CoNi/C	-	1 M KOH	1600	1.56	360	39	-	[151]
Co ₅ Mn-LDH/MWCNT ^j	0.283	1 M KOH	1600	-	300	74	0.47 @ 0.35 V	[15]
CoNi LDH/CoO	0.265	1 M KOH	1600	1.48	300	123	1.40 @ 0.40 V	[152]
CoCo LDH/CoO	0.265	1 M KOH	1600	1.54	340	123	0.80 @ 0.40 V	[152]
O-NiCoFe-LDH	0.12	0.1 M KOH	1600	-	340	93	0.02 @ 0.30 V	[154]
NiFeO _x /Co-N _y -C	0.196	1 M KOH	1600	1.47	310	60	-	[33]
NiCo-NS ^k	0.07	1 M KOH	-	1.52 @ 1 mA cm ⁻²	334	41	0.01 @ 0.30 V	[159]
CoCo-NS ^k	0.07	1 M KOH	-	1.54 @ 1 mA cm ⁻²	353	45	-	[159]
Exfoliated NiCo LDH	0.17	1 M KOH	-	-	367	112	-	[160]

*E*_{onset}, onset potential; *η* @ 10 mA cm⁻², the overpotential (*η*) located at the current density of 10 mA cm⁻²; TOF, the turnover frequency. ^a RGO, reduced graphene oxides; ^b N-S-G, N, S-doped graphene; ^c G, graphene; ^d NSs, nanosheets; ^e NWs, nanowires; ^f NRs, nanorods; ^g NCs, nanocrystals; ^h CF, carbon fiber; ⁱ MWCNT, multiwall carbon nanotubes; ^k NS, nanosheets.

3.5. Cobalt-Based Bifunctional Catalysts in Assembled Unitized Regenerative Fuel Cells

Bifunctional oxygen electrode catalysts play a vital role in the development of unitized regenerative fuel cells (URFCs). URFC, a compact energy storage and conversion device, can simultaneously work in a fuel cell mode to produce electricity, and as a water electrolyzer mode to store off-peak electricity in the form of hydrogen. In this closed-loop system, the essential component is the desired bifunctional oxygen electrode catalysts with high catalytic activity, long-term durability, and strongly resistance to anodic corrosion. To date, several previous studies have reported cobalt-based materials as promising bifunctional ORR/OER electrocatalysts for a URFC system [161]. Scott's group used cobalt-based ORR catalysts as the cathodes and demonstrated high and stable power density performance ($>200 \text{ mW cm}^{-2}$) in alkaline anion exchange membrane fuel cells (AAEMFCs) [162]. They further [163] modified the ORR and OER electrode with $\text{Cu}_{0.6}\text{Mn}_{0.3}\text{Co}_{2.1}\text{O}_4$ catalyst for regenerative $\text{H}_2\text{-O}_2$ fuel cell. In water electrolyzer mode, the onset voltage for water electrolysis (deionized water as electrolyte) was ca. 1.55 V. At 100 mA cm^{-2} , the voltages of fuel cell mode and electrolyzer mode were 0.58 V and 1.82 V, respectively, indicating that the fuel cell to electrolyzer voltage ratio was ca. 31.87%. However, the current densities in both modes were much lower than those cells with KOH as electrolyte, probably because of the large electrolytic resistance.

Xu et al. [161] measured the performance of a unitized regenerative anion exchange membrane fuel cells (UR-AEMFCs), using a bifunctional ORR/OER catalysts, $\text{Co}_3\text{O}_4/\text{oCNT}$, (oCNT stands for oxidized CNTs) on the oxygen electrode. The obtained performance in fuel cell mode was basically consistent with the result in half-cell mode, while the electrolyzer performance was poor. Likewise, 0.1 M KOH solution in the cell, significantly improved the performance of electrolysis.

Our group designed a self-assembly laminar flow unitized regenerative micro-cell (LFURMC) without gas separator, which was provided with Pt/C as the hydrogen catalyst, bifunctional oxygen $\text{NiFeO}_x/\text{CoNi}_y\text{-C}$ catalyst and 3 M KOH electrolyte [33]. In the fuel cell mode, Figure 18, the $\text{NiFeO}_x/\text{CoNi}_y\text{-C}$ electrode showed the maximum power density of 56 mW cm^{-2} , which was very close to that of Pt/C (63 mW cm^{-2}) and IrO_x/C (58 mW cm^{-2}); in the electrolyzer mode, the maximum electrical power consumed on $\text{NiFeO}_x/\text{CoNi}_y\text{-C}$ (237 mW cm^{-2}), was more than three times that on Pt/C (73 mW cm^{-2}). Moreover, the calculated round-trip efficiency (RTE) of $\text{NiFeO}_x/\text{CoNi}_y\text{-C}$ catalyst nearly held a level of ca. 52% during three cycles, evaluating a super reversibility of the $\text{NiFeO}_x/\text{CoNi}_y\text{-C}$ electrode.

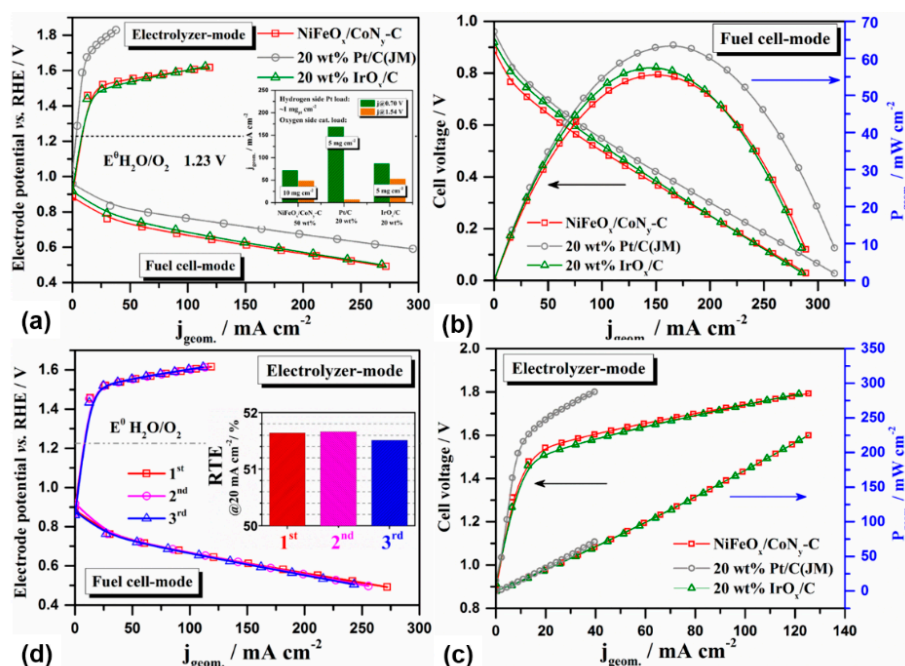


Figure 18. Alkaline laminar flow unitized regenerative micro-cell (LFURMC) experiment. (a) Current-potential of the material as anode (electrolyzer mode) and cathode (fuel cell mode). inset: The geometric activities comparison of three LFURMC; (b) the cell voltage and power density curves of the fuel cell with platinum as the hydrogen catalyst, and NiFeO_x/CoN_y-C, 20 wt% Pt/C and 20 wt% IrO_x/C cathode catalysts; (c) the cell voltage and power density curves of the electrolyzer with platinum as the hydrogen catalyst, and NiFeO_x/CoN_y-C, 20 wt% Pt/C and 20 wt% IrO_x/C cathode catalysts; (d) Stability tests of LFURMC based on the NiFeO_x/CoN_y-C catalyst (three runs), inset: round-trip-efficiency (RTE) for the three cycles. All measurements were conducted at room temperature (25 °C). Remark: no Ohmic-drop correction was made for all determinations. Reproduced from [33], Copyright © Elsevier, 2017.

4. Electrocatalysts for Hydrogen Evolution Reaction (HER)

4.1. Mechanism of HER

The hydrogen evolution reaction (HER) is the half-reaction carried out at the cathode of an electrolyzer, in which protons (acidic environment) or water molecules (alkaline environment) are reduced, accompanied by the subsequent evolution of gaseous hydrogen through the water splitting process. The overall HER proceeds as follow (in all cases, any catalytic site is denoted as “*“):

Acid medium:



Alkaline medium:



The standard potentials (E°) are different due to the nature of the active ions in the reaction. As we can expect, the HER as any electrochemical reaction possesses a certain activation energy barrier to promote the reaction, usually denoted as overpotential η . Therefore, the HER usually demands the assistance of electrocatalytic materials to lower η , and consequently to increase the reaction rate and efficiency. The mechanisms to achieve the HER can be Volmer–Heyrovsky or Volmer–Tafel. In acid medium, the HER proceeds according to the following steps:

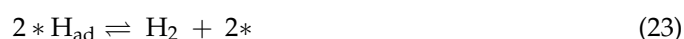
- i. A hydrogen atom adsorption, which is the result of the combination of a proton and an electron on the electrode surface (proton discharge) is the Volmer reaction:



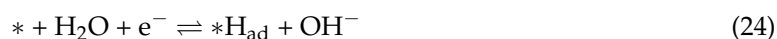
- ii. The adsorbed hydrogen atom interacting with a proton and an electron leads to an electrochemical desorption. This reaction is the Heyrovsky reaction:



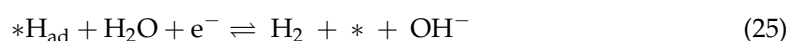
- iii. The coupling of the two adsorbed hydrogen atoms leads to a dissociative desorption of hydrogen, the Tafel reaction:



In alkaline electrolyte, due to the OH^- abundance, the HER proceeds according to the following steps. For the Volmer reaction, the molecular water couples with an electron, leading in an adsorbed hydrogen atom at the electrode surface:



- i. For the Heyrovsky reaction, the adsorbed hydrogen atom combines with molecular water and an electron, allowing the electrochemical desorption of hydrogen:



- ii. The Tafel reaction is similar to that of the acidic medium.

In acid and alkaline media, for the HER, the hydrogen adsorption starts via the Volmer reaction, Equations (21) or (24). The successive hydrogen desorption can proceed via the Heyrovsky reaction, Equations (22) or (25) or the dissociative desorption via the Tafel reaction, Equation (23). On the other hand, the HER can be proposed by the Tafel slope, as derived from the HER polarization curves. The Tafel slope analysis represents the intrinsic nature of the electrocatalytic material, and the empirical magnitude of the Tafel slope can provide information to distinguish the mechanism. For a Tafel rate determining step (RDS), the slope is 30 mV dec^{-1} , whereas for Heyrovsky and Volmer RDS, slopes are 40, and 120 mV dec^{-1} , respectively.

The HER mechanism on Co-based catalysts follows the Volmer–Heyrovsky mechanism, where normally the Heyrovsky step is the RDS in acid medium [164,165]; whereas the Volmer step is considered the RDS in alkaline medium [165].

4.2. Hydrogen Evolution on Cobalt Chalcogenides Catalysts

4.2.1. Synthesis Strategy

Co-based catalysts are potential materials for the HER. Considerable research efforts were devoted to synthesizing cobalt chalcogenides as catalysts for HER. Those dichalcogenides are in the pyrite/marcasite phase. The metal atoms are octahedrally coordinated to adjacent S/Se atoms. Kong et al. [164] claimed that CoSe_2 possessed one of the best HER performance among the first row transition-metal chalcogenides, because of the partially filled e_g band of CoSe_2 . With this knowledge, Liu et al. [166] developed CoSe_2 nanowire arrays on carbon cloth ($\text{CoSe}_2 \text{ NW/CC}$) through a facile two-step hydrothermal preparative strategy. The hydrogen evolution reaction performance was tested in $0.5 \text{ M H}_2\text{SO}_4$. Current densities of 10 and 100 mA cm^{-2} at overpotentials of 130 and 164 mV were maintained for at least 48 h. The excellent HER activity and durability for $\text{CoSe}_2 \text{ NW/CC}$ were explained as follows. (1) The nanoarray allows for the exposure of more active sites; (2) The direct

growth of CoSe₂ on CC offers intimate contact, good mechanical adhesion and excellent electrical connection between them; and (3) The absence of polymer binder for catalyst immobilization.

Vertical-aligned graphene nanoribbons (VA-GNRs) were used as a support for cobalt carbide nanocrystals, e.g., Co₃C/VA-GNRs by Fan et al. [119]. The HER performance in acid medium revealed a Tafel slope of 57 mV dec⁻¹ and $\eta_{@10}$ of ca. 0.125 V. Zhang et al. [167] synthesized by a hydrothermal procedure polymorphic CoSe₂ supported onto graphite with promising HER performance, Figure 19. These authors observed that the optimized calcination temperature of CoSe_x was 300 °C. This treatment allowed the change of a mixed orthorhombic to cubic phase of CoSe₂. The polymorphic CoSe₂ catalytic center showed higher HER performance compared to CoSe_x, cubic CoSe₂ and CoSe synthesized under the same conditions. The high performance observed in polymorphic CoSe₂ was attributed to the enhanced chemisorption of H atoms onto the mixed-phase in the Tafel step.

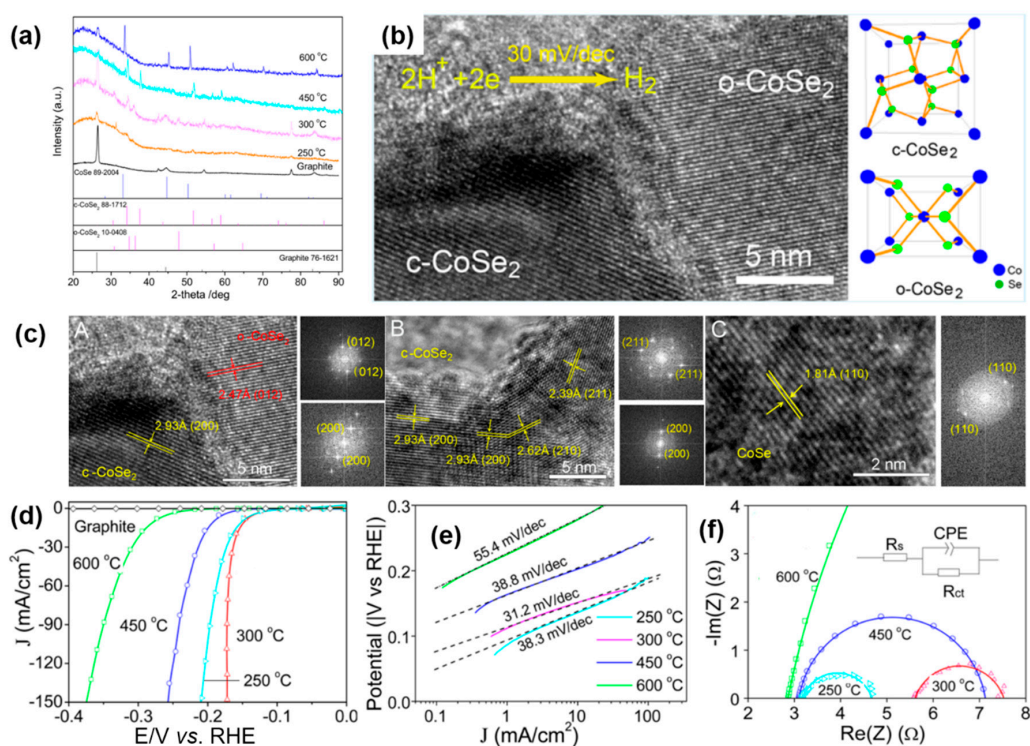


Figure 19. (a) XRD patterns of the as-prepared CoSe_x/GD samples calcined at different temperatures; (b) the crystal structures of cubic CoSe₂ (c-CoSe₂) and orthorhombic CoSe₂ (o-CoSe₂); (c) HRTEM micrographs and electron-diffraction patterns of c-CoSe₂ annealed at 300 °C (A), c-CoSe₂ annealed at 450 °C (B) and CoSe annealed at 600 °C (C), respectively; (d) *iR*-corrected hydrogen evolution reaction (HER) polarization curves (cathodic sweep) of CoSe_x (250 °C), c-CoSe₂ (300 °C), c-CoSe₂ (450 °C) and CoSe (600 °C) in H₂-saturated 0.5 M H₂SO₄ solution with a scan rate of 3 mV s⁻¹; (e) Tafel slopes analysis of polymorphic CoSe₂/GD catalysts; (f) Nyquist plots for the HER at an overpotential of -0.5 V vs. SCE from 200 kHz to 50 mHz, the data were fitted by the simplified Randles equivalent circuit (inset). Reproduced from [167], Copyright © American Chemical Society, 2015.

4.2.2. Crystal Structure and Nanostructure

Tuning the crystal structure and surface morphology, a catalytic center can enhance its performance for electrochemical energy conversion devices. For example, the combined effect of morphology and phase of CoSe₂ was studied by Li et al. [168]. These authors fashioned CoSe₂ nanotubes with orthorhombic- (o-CoSe₂) and cubic-phases (c-CoSe₂) by a facile precursor transformation method, Figure 20a. In the synthetic process, the crystal structure and surface morphology of CoSe₂ were adjusted by the calcination temperature. Benefiting from the advantageous tubular structure, including the functional shells and well-defined interior voids, CoSe₂ nanotubes

showed a clear HER performance in alkaline medium. Interestingly, the authors observed that the orthorhombic phase (*o*-CoSe₂) possessed the highest HER performance in terms of lowest onset overpotential (~54 mV) and smallest Tafel slope (~65.9 mV decade⁻¹) in alkaline medium, see Figure 20b,c. Another approach where the morphology effect towards the HER was observed were given by CoSe₂ nanoparticles [21], nanowires [166,169], interwoven [170], nanocomposites [171], hollow microspheres [172], and nanosheets [173].

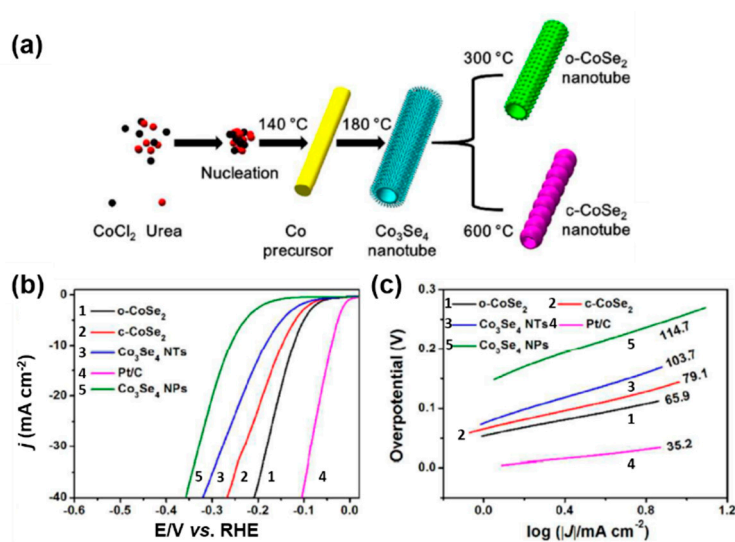


Figure 20. (a) Synthesis route of CoSe₂ nanotubes; (b) *iR*-corrected HER polarization curves (cathodic sweep) of *o*-CoSe₂, *c*-CoSe₂, Co₃Se₄ NTs, Pt/C and Co₃Se₄ nanoparticles (NPs) catalysts at a scan rate of 5 mV s⁻¹ in 1 M KOH solution; and (c) Tafel slopes analysis of all the catalysts. The mass loading of the catalyst was ~0.283 mg cm⁻². Reproduced from [168], Copyright © Royal Society of Chemistry, 2017.

On the other hand, the construction of the ultra-thin two-dimensional (2D) nanostructure have become an promising approach to tailor novel high active electrocatalytic centers, due to the confined charge interaction in the planar dimension with minimum interlayer interaction (which in fact hinders the electrical conductivity), thus improving catalytic properties [174]. An ultrathin 2D structure with abundant low-coordinated surface atoms offers adequate active sites for hydrogen evolution reactions. Liu group [175], prepared the Mn_{0.05}Co_{0.95}Se₂ ultrathin nanosheets with 1.2 nm thickness by usual liquid exfoliation of homogeneous Mn doped CoSe₂/DETA hybrid nanosheets. The subtle distortion of atomic arrangement was induced after the incorporation of Mn²⁺ into CoSe₂, which boosted the exposure of more active edge Se sites, optimizing the HER activity. Since the chalcogenide atoms at the edges of pyrite catalyst have been verified to be HER active sites analogous to MoS₂, the authors proposed that the edge Se sites in the CoSe₂ probably were responsible for HER as the active sites. The Mn-doped CoSe₂ ultrathin nanosheets displayed outstanding HER performance, with a low overpotential of 174 mV, and a Tafel slope of 36 mV dec⁻¹.

4.3. Hydrogen Evolution on MOFs Catalysts

Regarding derived-MOF electrocatalysts, the porous ZIF-9 was used as a cobalt source and sacrificial template to synthesize CoS₂, see Figure 21a [176]. The ZIF-9 presented very weak HER electrocatalytic performance, the benzimidazole ligands of ZIF-9 were substituted by S ions after adding sulfur sources in the appropriate mention of 200 °C and 1 atm hydrothermal temperature and pressure, the resulting CoS₂ had excellent HER activity. The introduction of graphene to further enhance the conductivity of the material, and improve the dispersion of cobalt disulfide, on RGO (CoS₂/RGO) was necessary. In Figure 21b, the HER performance of the material with an overpotential of 180 mV at 10 mA cm⁻² was smaller than those of ZIF-9, and ZIF-9/RGO. The Tafel slope of CoS₂/RGO

was $75 \text{ mV decade}^{-1}$. This slope was near that obtained on Pt/C electrode. Zhang et al. [177] synthesized the core-shell structure Co/Co₉S₈ anchored onto S-, N- co-doped porous graphene sheet (Co/Co₉S₈@SNGS). They employed thiophene-2,5-dicarboxylate (Tdc), and 4,4-bipyridine (Bpy) organic ligands assembled Co-based metal-organic frameworks in situ grown on graphene oxide sheets. The S-containing Tdc, and the N-containing Bpy did not only trigger the growth of Co-MOF nanocrystals but also fixed the S/N atomic ratio of 1:2.4 on graphene oxide sheets. After pyrolysis of Co-MOF at 1000 °C the catalyst showed high bifunctional catalytic activities for the OER, and HER in 0.1 M KOH electrolyte, with an overpotential of 290 mV for OER at a current density of 10 mA cm^{-2} , and 350 mV for HER at a current density of 20 mA cm^{-2} .

Besides the cobalt sulfide, cobalt selenide could also be synthesized using MOFs. CoSe₂ nanoparticles embedded in defective carbon nanotubes (CoSe₂@DC) was produced by carbon-oxidation-selenization procedure of Co-based MOFs [64], Figure 22. The pre-oxidation treatment was a crucial step in introducing an increasing number of defects into carbon nanotubes, which promoted the reaction between Co@Carbon and selenium. The authors associated the enhanced HER performance to the induced carbon-surface defect density, which favored the diffusion of Se atoms through Co atoms, and made the best use of the exposed active surface area. Lin et al. [178] synthesized MOF-derived cobalt diselenide (MOF-CoSe₂) built with CoSe₂ nanoparticles anchored into nitrogen-doped graphitic carbon through in situ selenization of Co-based MOFs. The N-doped MOFs derived architecture benefited of the high conductivity provided by the abundant active reaction sites, ensuring a robust contact between CoSe₂ nanoparticles and N-doped carbon support.

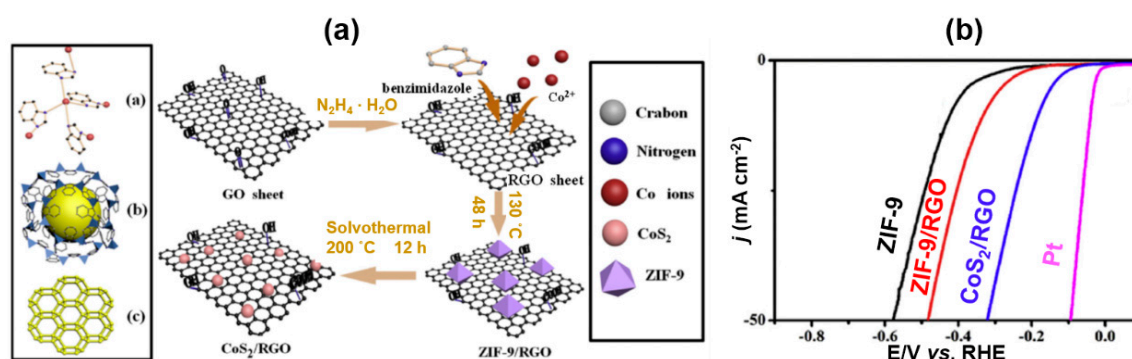


Figure 21. (a) Schematic illustration of the synthesis of CoS₂/RGO; and (b) HER polarization curves (cathodic sweep) collected on different catalysts with mass loading of 0.285 mg cm^{-2} in $0.5 \text{ M H}_2\text{SO}_4$ acidic solution at a scan rate of 5 mV s^{-1} at room temperature. Reproduced from [176], Copyright © Elsevier, 2017.

Table 3 summarizes the relevant contributions regarding the HER Co-based catalysts, wherein it is possible to highlight that these catalysts present considerable performance in acid and in alkaline media. One can stress some remarkable parameters regarding the HER electrocatalytic performance, namely, (1) among non-precious catalysts, Co-based catalytic centers are one potential candidate to replace Pt-based electrodes for the water-splitting cathodic reaction, their high activity and stability; (2) since cobalt selenides catalytic centers boost the HER in acidic and in alkaline media, the chemical coordination of Co with sulfides and phosphides showed considerable performance in acid media; (3) the crystalline structure, due to the exposed active sites and electronic properties are crystalline-phase dependent; (4) the surface morphology can expose active sites; (5) the electrical coupling with conductive supports; in as much as the coupling of Co-based catalytic centers with high surface area and high electrical conductive supports modulate the dispersion of the catalytic centers and the interfacial charge-transfer. Doped carbon supports (mainly N-doped graphitic surfaces) could modify the electronic structure of the anchored catalytic centers; and (6) the synthesis route and metal source; e.g., MOFs, could provide hybrid materials which combine the surface properties of the

porous carbon network and the catalytic properties of Co domains. Those parts are critical points to be considered in tailoring HER advanced materials.

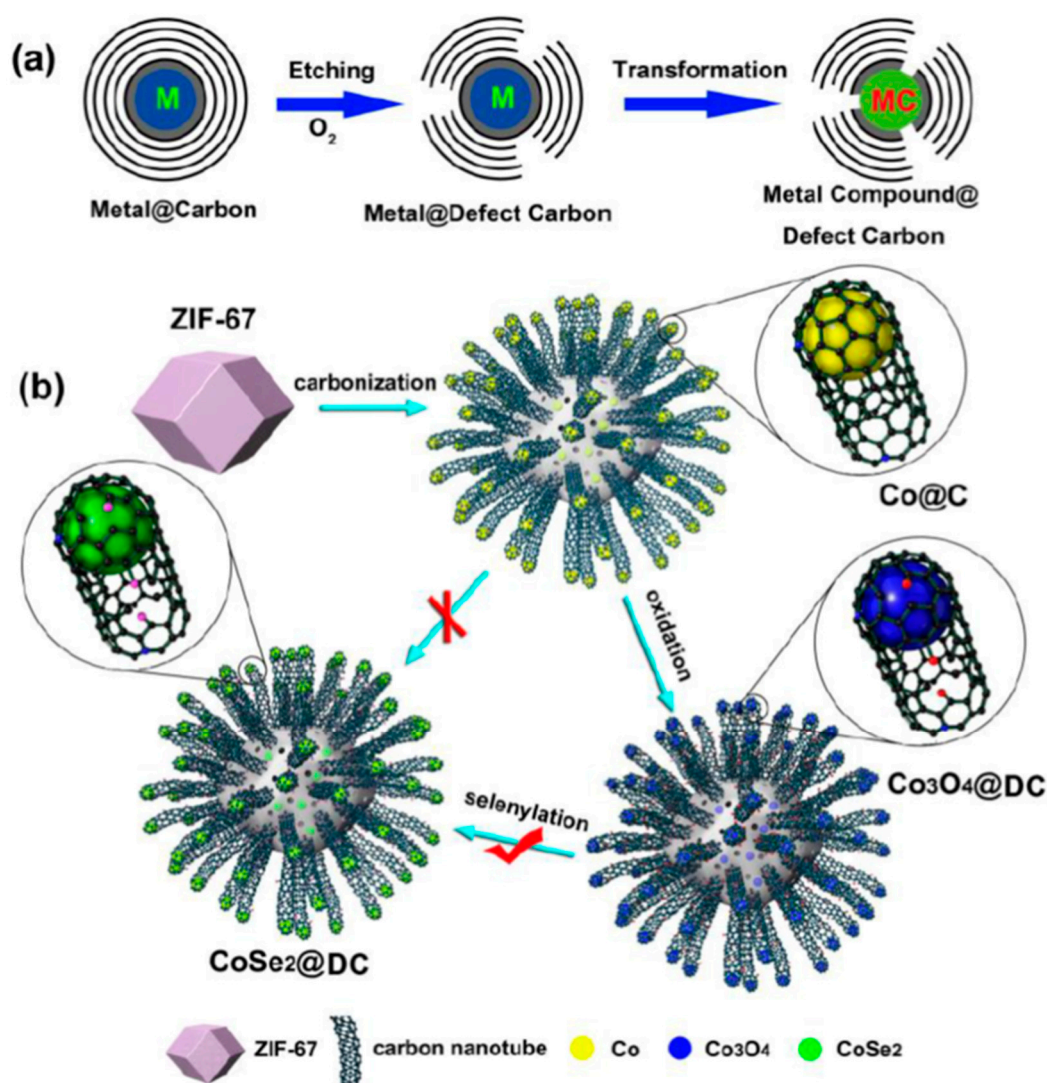


Figure 22. Schematic representation of (a) the etching process of metal@carbon by pre-oxidation; (b) the synthetic chemical route for $CoSe_2@DC$. Reproduced from [64], Copyright © Elsevier, 2016.

Table 3. Selected state-of-the-art Co-based catalyst towards the hydrogen evolution reaction.

Catalysts	Mass Loading (mg cm ⁻²)	Electrolyte	RPM (rpm)	η @10 mA cm ⁻² (mV)	Tafel Slope (mV dec ⁻¹)	Refs.
CoSe ₂ @DC ^a	0.357	0.5 M H ₂ SO ₄	-	132	82	[64]
Co ₃ C-GNRs ^b	0.142	0.5 M H ₂ SO ₄	1600	125	57	[119]
Co ₂ B/CoSe ₂	0.4	1 M KOH	-	300	76	[136]
Cubic CoSe ₂ /GD ^c	2.8	0.5 M H ₂ SO ₄	-	200	42	[179]
Cubic CoSe ₂ nanoparticles/CF ^d	0.26	0.5 M H ₂ SO ₄	-	137	42	[21]
Interwoven CoSe ₂ /CNT ^e	0.54	0.5 M H ₂ SO ₄	-	186	32	[170]
CoSe ₂ -CNT ^e	0.255	0.5 M H ₂ SO ₄	2000	174	38	[171]
Orthorhombic CoSe ₂ nanotubes	0.283	1 M KOH	-	124	66	[168]
Cubic CoSe ₂ nanotubes	0.283	1 M KOH	-	149	79	[168]
Polymorphic CoSe/GD ^c	-	0.5 M H ₂ SO ₄	-	150	31	[167]
CoSe ₂ hollow microspheres/rGO	0.277	0.5 M H ₂ SO ₄	-	250	55	[172]
CoPS/NC ^f	0.17	0.5 M H ₂ SO ₄	2000	80	68	[180]
CoPS/NC ^f	0.17	1 M KOH	2000	148	78	[180]
Nanowires CoSe ₂ /CF ^d	-	0.5 M H ₂ SO ₄	-	150	34	[169]
Nanowires CoSe ₂ /CC ^g	-	0.5 M H ₂ SO ₄	-	150	32	[166]
Nanosheets CoSe ₂ /Ti plate	0.16	0.5 M H ₂ SO ₄	-	165	39	[173]
CoS/CC ^g	3.77	1 M KOH	-	197	98	[181]
CoS/CC ^g	3.77	0.5 M H ₂ SO ₄	-	212	112	[181]
CoS ₂ /RGO ^h	0.285	0.5 M H ₂ SO ₄	-	18	75	[176]
CoS ₂ /P	-	0.5 M H ₂ SO ₄	-	67	50	[182]
		1 M KOH	-	67	60	
Co ₉ S ₈ /NC ^e @MoS ₂	0.283	0.5 M H ₂ SO ₄	-	117	69	[183]
		1 M PBS	-	267	126	

η @ 10 mA cm⁻², the overpotential (η) located at the current density of 10 mA cm⁻²; ^a DC, defective carbon nanotubes; ^b GNRs, graphene nanoribbons; ^c GD, graphite disk; ^d CF, carbon fiber; ^e CNT, carbon nanotubes; ^f NC, N-doped carbon; ^g CC, carbon cloth; ^h RGO, reduced graphene oxides.

5. Summary and Outlook

This review mainly focused on novel cobalt-based catalysts (CoCat) for electrochemical processes, e.g., ORR, OER and HER in acid and alkaline electrolyte, categorized into five groups, namely, cobalt chalcogenides (selenides, sulfides), cobalt oxides, Co-LDH, Co-MOFs, and Co-N_x/C. Tables 1–3 summarize the corresponding electrocatalytic parameters such as onset potential, half-wave potential, Tafel slope, and so on. Based on those results, we assess that cobalt-based materials have emerged as interesting and potential alternatives because of their activities, superior electrochemical stability, and durability compared with precious metals (e.g., Pt, Ir and Ru). While loading cobalt metal compounds on conducting carbonaceous materials, the cobalt-carbon hybrids showed enhanced electrochemical performance. With respect to the electrocatalytic performance of cobalt-based catalysts, the surface engineering (e.g., doping, etching and edging), the structural properties and morphologies (e.g., specific surface area, porosity, core-shell and hollow), anionic substitution (S, Se and Te), defects (e.g., vacancies, topological defects, lattice defects and edge sites), and support materials (e.g., RGO, CNTs, CNHs, and Vulcan-XC-72) were discussed in detail. Furthermore, these catalysts achieved desired catalytic activities towards ORR, OER and HER, as a result of the following strategies: (1) enhancing the SMSI effect, and the synergistic coupling of catalyst-support, resulting in faster electron transport and charge transfer; (2) modulation of the active sites Co³⁺/Co²⁺ ratio via the NaBH₄-assisted route; (3) elucidation of active sites and building well-engineered architecture under the confinement effect; (4) exfoliating the bulk catalysts into atomic level thickness, boosted the exposure and generation of active sites; (5) the direct growth of cobalt-based catalysts on 3D conductive support, e.g., Co foil, Ni foam, and carbon fiber paper, avoided the use of polymer binders, facilitating the electrolyte diffusion, and driving off the as-formed gas bubbles from the electrode surface.

In search of potentially promising and suitable candidates to replace precious catalyst centers for energy conversion and storage systems, a series of cobalt-based materials has been developed. The last 10 years of research on such materials, there has been a boom in the number of publications, that helped to highlight the assembly of unitized regenerated cells based on bifunctional ORR and OER catalysts by exchanging the fuel cell mode to electrolyzer mode. Taking advantage of the exceptional

properties which can be achieved by the rational design of materials, such as a large specific surface area, ultrathin/atomic level thickness, optimized porous structure for the exposure of active sites, high conductivity, and a high uniform dispersion, the Co-based nanomaterials will continue to open new avenues to further enhance electrocatalytic activity and stability. Among these Co-based catalysts, due to the coexistence of the diverse active sites including doping via nitrogen, Co-N_x/C derived from LDH, MOF and other precursor used as templates were considered to substitute Pt, Ru, and Ir-based catalysts in acidic and alkaline medium. Last but not least, in-depth studies and interdisciplinary cooperation are still urgently required. Therefore, the design and development of cobalt-based electrocatalysts should be concentrated on the following aspects in the future: (1) understanding the fundamental reaction mechanisms of ORR, OER and HER by virtue of theoretical prediction and simulation; (2) probing and identifying the ideal active sites, and then integrating the different types of active sites to develop the so-called bifunctional oxygen electrode electrocatalysts or bifunctional HER–OER electrocatalysts; (3) gaining insights into the active sites involved such as metal species, oxygen vacancies, and topological defects, by using various advanced characterization techniques, e.g., X-ray absorption near edge structure spectroscopy (XANES), sub-Ångström-resolution aberration-corrected scanning transmission electron microscopy (HAADF–STEM), and in situ Raman; (4) developing simple and low-cost approaches to synthesize the catalysts with satisfactory activity and stability is expected to achieve the mass-production and high quality required for large-scale applications.

Author Contributions: H.Z. searched the literature, and wrote the main part of the current work; C.A.C.-R. contributed with the data analysis, writing and revision of the current literature; Y.Z. wrote part of this work; S.Z. redacted and corrected the references; Y.F. and N.A.-V. organized, supervised and reviewed the work.

Funding: This research received no external funding.

Acknowledgments: This work is supported by National Key R&D Program of China (No. 2016YFB0301600), the National Natural Science Foundation of China (No. 21571015, 21627813), Program for Changjiang Scholars and Innovative Research Team in University (No. IRT1205), China Scholarship Council (H.Z.), The Priority Academic Program Development of Jiangsu Higher Education Institutions (Y.Z.), and CONACyT-Mexico Scholarship (C.A.C.-R.).

Conflicts of Interest: The authors declare no conflict of interest.

References

1. Park, S.; Shao, Y.Y.; Liu, J.; Wang, Y. Electrocatalysts for Water Electrolyzers and Reversible Fuel Cells: Status and Perspective. *Energy Environ. Sci.* **2012**, *5*, 9331–9344. [[CrossRef](#)]
2. Carrette, L.; Friedrich, K.A.; Stimming, U. Fuel Cells –Fundamentals and Applications. *Fuel Cells* **2001**, *1*, 5–39. [[CrossRef](#)]
3. Jiao, Y.; Zheng, Y.; Jaroniec, M.; Qiao, S.Z. Design of Electrocatalysts for Oxygen- and Hydrogen-Involving Energy Conversion Reactions. *Chem. Soc. Rev.* **2015**, *44*, 2060–2086. [[CrossRef](#)] [[PubMed](#)]
4. Suen, N.T.; Hung, S.F.; Quan, Q.; Zhang, N.; Xu, Y.J.; Chen, H.M. Electrocatalysis for the Oxygen Evolution Reaction: Recent Development and Future Perspectives. *Chem. Soc. Rev.* **2017**, *46*, 337–365. [[CrossRef](#)] [[PubMed](#)]
5. Ge, X.; Sumboja, A.; Wu, D.; An, T.; Li, B.; Goh, F.W.T.; Hor, T.S.A.; Zong, Y.; Liu, Z. Oxygen Reduction in Alkaline Media: From Mechanisms to Recent Advances of Catalysts. *ACS Catal.* **2015**, *5*, 4643–4667. [[CrossRef](#)]
6. Shao, M.H.; Chang, Q.W.; Dodelet, J.P.; Chenitz, R. Recent Advances in Electrocatalysts for Oxygen Reduction Reaction. *Chem. Rev.* **2016**, *116*, 3594–3657. [[CrossRef](#)] [[PubMed](#)]
7. Dai, L.M.; Xue, Y.H.; Qu, L.T.; Choi, H.J.; Baek, J.B. Metal-Free Catalysts for Oxygen Reduction Reaction. *Chem. Rev.* **2015**, *115*, 4823–4892. [[CrossRef](#)] [[PubMed](#)]
8. Liu, Q.; Jin, J.T.; Zhang, J.Y. NiCo₂S₄@Graphene as a Bifunctional Electrocatalyst for Oxygen Reduction and Evolution Reactions. *ACS Appl. Mater. Interfaces* **2013**, *5*, 5002–5008. [[CrossRef](#)] [[PubMed](#)]
9. Gong, M.; Li, Y.G.; Wang, H.L.; Liang, Y.Y.; Wu, J.Z.; Zhou, J.G.; Wang, J.; Regier, T.; Wei, F.; Dai, H.J. An Advanced Ni–Fe Layered Double Hydroxide Electrocatalyst for Water Oxidation. *J. Am. Chem. Soc.* **2013**, *135*, 8452–8455. [[CrossRef](#)] [[PubMed](#)]

10. Zhao, A.Q.; Masa, J.; Xia, W.; Maljusch, A.; Willinger, M.G.; Calavel, G.; Xie, K.P.; Schlogl, R.; Schuhmann, W.; Muhlert, M. Spinel Mn–Co Oxide in N-Doped Carbon Nanotubes as a Bifunctional Electrocatalyst Synthesized by Oxidative Cutting. *J. Am. Chem. Soc.* **2014**, *136*, 7551–7554. [[CrossRef](#)] [[PubMed](#)]
11. Xie, R.F.; Fan, G.L.; Ma, Q.; Yang, L.; Li, F. Facile Synthesis and Enhanced Catalytic Performance of Graphene-Supported Ni Nanocatalyst from a Layered Double Hydroxide-Based Composite Precursor. *J. Mater. Chem. A* **2014**, *2*, 7880–7889. [[CrossRef](#)]
12. Sumboja, A.; An, T.; Goh, H.Y.; Lubke, M.; Howard, D.P.; Xu, Y.; Handoko, A.D.; Zong, Y.; Liu, Z. One-Step Facile Synthesis of Cobalt Phosphides for Hydrogen Evolution Reaction Catalysts in Acidic and Alkaline Medium. *ACS Appl. Mater. Interfaces* **2018**, *10*, 15673–15680. [[CrossRef](#)] [[PubMed](#)]
13. Pramana, S.S.; Cavallaro, A.; Li, C.; Handoko, A.D.; Chan, K.W.; Walker, R.J.; Regoutz, A.; Herrin, J.S.; Yeo, B.S.; Payne, D.J.; et al. Crystal Structure and Surface Characteristics of Sr-Doped GdBaCo₂O_{6–δ} Double Perovskites: Oxygen Evolution Reaction and Conductivity. *J. Mater. Chem. A* **2018**, *6*, 5335–5345. [[CrossRef](#)]
14. Lübke, M.; Sumboja, A.; McCafferty, L.; Armer, C.F.; Handoko, A.D.; Du, Y.H.; McColl, K.; Cora, F.; Brett, D.; Liu, Z.L.; et al. Transition-Metal-Doped α -MnO₂ Nanorods as Bifunctional Catalysts for Efficient Oxygen Reduction and Evolution Reactions. *ChemistrySelect* **2018**, *3*, 2613–2622. [[CrossRef](#)]
15. Jia, G.; Hu, Y.; Qian, Q.; Yao, Y.; Zhang, S.; Li, Z.; Zou, Z. Formation of Hierarchical Structure Composed of (Co/Ni)Mn-LDH Nanosheets on MWCNT Backbones for Efficient Electrocatalytic Water Oxidation. *ACS Appl. Mater. Interfaces* **2016**, *8*, 14527–14534. [[CrossRef](#)] [[PubMed](#)]
16. Yang, Z.; Yao, Z.; Li, G.; Fang, G.Y.; Nie, H.G.; Liu, Z.; Zhou, X.M.; Chen, X.A.; Huang, S.M. Sulfur-Doped Graphene as an Efficient Metal-Free Cathode Catalyst for Oxygen Reduction. *ACS Nano* **2012**, *6*, 205–211. [[CrossRef](#)] [[PubMed](#)]
17. Gago, A.S.; Gochi-Ponce, Y.; Feng, J.Y.; Esquivel, J.P.; Sabate, N.; Santander, J.; Alonse-Vante, N. Tolerant Chalcogenide Cathodes of Membraneless Micro Fuel Cells. *ChemSusChem* **2012**, *5*, 1488–1494. [[CrossRef](#)] [[PubMed](#)]
18. Wang, H.L.; Liang, Y.Y.; Li, Y.G.; Dai, H.J. Co_{1–x}S-Graphene Hybrid: A High-Performance Metal Chalcogenide Electrocatalyst for Oxygen Reduction. *Angew. Chem. Int. Ed. Engl.* **2011**, *50*, 10969–10972. [[CrossRef](#)] [[PubMed](#)]
19. Dou, S.; Tao, L.; Hou, J.; Wang, S.Y.; Dai, L.M. Etched and Doped Co₉S₈/Graphene Hybrid for Oxygen Electrocatalysis. *Energy Environ. Sci.* **2016**, *9*, 1320–1326. [[CrossRef](#)]
20. Chao, Y.S.; Tsai, D.S.; Wu, A.P.; Tseng, L.W.; Huang, Y.S. Cobalt Selenide Electrocatalyst Supported by Nitrogen-Doped Carbon and its Stable Activity toward Oxygen Reduction Reaction. *Int. J. Hydrogen Energy* **2013**, *38*, 5655–5664. [[CrossRef](#)]
21. Kong, D.S.; Wang, H.T.; Lu, Z.Y.; Cui, Y. CoSe₂ Nanoparticles Grown on Carbon Fiber Paper: An Efficient and Stable Electrocatalyst for Hydrogen Evolution Reaction. *J. Am. Chem. Soc.* **2014**, *136*, 4897–4900. [[CrossRef](#)] [[PubMed](#)]
22. Zhang, H.; Wang, H.H.; Sumboja, A.; Zang, W.J.; Xie, J.P.; Gao, D.Q.; Pennycook, S.J.; Liu, Z.L.; Guan, C.; Wang, J. Integrated Hierarchical Carbon Flake Arrays with Hollow P-Doped CoSe₂ Nanoclusters as an Advanced Bifunctional Catalyst for Zn-Air Batteries. *Adv. Funct. Mater.* **2018**, *28*, 1804846. [[CrossRef](#)]
23. Chen, P.R.; Yang, F.K.; Kostka, A.; Xia, W. Interaction of Cobalt Nanoparticles with Oxygen- and Nitrogen-Functionalized Carbon Nanotubes and Impact on Nitrobenzene Hydrogenation Catalysis. *ACS Catal.* **2014**, *4*, 1478–1486. [[CrossRef](#)]
24. Mao, S.; Wen, Z.H.; Huang, T.Z.; Hou, Y.; Chen, J.H. High-Performance Bi-Functional Electrocatalysts of 3D Crumpled Graphene–Cobalt Oxide Nanohybrids for Oxygen Reduction and Evolution Reactions. *Energy Environ. Sci.* **2014**, *7*, 609–616. [[CrossRef](#)]
25. Liang, Y.Y.; Li, Y.G.; Wang, H.L.; Zhou, J.G.; Wang, J.; Regier, T.; Dai, H.J. Co₃O₄ Nanocrystals on Graphene as a Synergistic Catalyst for Oxygen Reduction Reaction. *Nat. Mater.* **2011**, *101*, 780–786. [[CrossRef](#)] [[PubMed](#)]
26. Chen, Y.Z.; Wang, C.M.; Wu, Z.Y.; Xiong, Y.J.; Xu, Q.; Yu, Y.H.; Jiang, H.L. From Bimetallic Metal-Organic Framework to Porous Carbon: High Surface Area and Multicomponent Active Dopants for Excellent Electrocatalysis. *Adv. Mater.* **2015**, *27*, 5010–5016. [[CrossRef](#)] [[PubMed](#)]
27. Ma, T.Y.; Dai, S.; Jaroniec, M.; Qiao, S.Z. Metal–Organic Framework Derived Hybrid Co₃O₄–Carbon Porous Nanowire Arrays as Reversible Oxygen Evolution Electrodes. *J. Am. Chem. Soc.* **2014**, *136*, 13925–13931. [[CrossRef](#)] [[PubMed](#)]

28. Zhong, H.H.; Lou, Y.; He, S.; Tang, P.G.; Li, D.Q.; Alonso-Vante, N.; Feng, Y.J. Electrocatalytic Cobalt Nanoparticles Interacting with Nitrogen-Doped Carbon Nanotube in Situ Generated from a Metal-Organic Framework for the Oxygen Reduction Reaction. *ACS Appl. Mater. Interfaces* **2017**, *9*, 2541–2549. [[CrossRef](#)] [[PubMed](#)]
29. Zhang, W.J.; Sumboja, A.; Ma, Y.Y.; Zhang, H.; Wu, Y.; Wu, S.S.; Wu, H.J.; Liu, Z.L.; Guan, C.; Wang, J.; et al. Single Co Atoms Anchored in Porous N-Doped Carbon for Efficient Zinc–Air Battery Cathodes. *ACS Catal.* **2018**, *8*, 8961–8969. [[CrossRef](#)]
30. Guan, C.; Sumboja, A.; Zang, W.J.; Qian, Y.H.; Zhang, H.; Liu, X.M.; Liu, Z.L.; Zhao, D.; Pennycook, S.J.; Wang, J. Decorating Co/CoN_x Nanoparticles in Nitrogen-Doped Carbon Nanoarrays for Flexible and Rechargeable Zinc–Air Batteries. *Energy Storage Mater.* **2018**, *16*, 243–250. [[CrossRef](#)]
31. Fan, G.L.; Li, F.; Evans, D.G.; Duan, X. Catalytic Applications of Layered Double Hydroxides: Recent Advances and Perspectives. *Chem. Soc. Rev.* **2014**, *43*, 7040–7066. [[CrossRef](#)] [[PubMed](#)]
32. Zhang, S.L.; Zhang, Y.; Jiang, W.J.; Liu, X.; Xu, S.L.; Hou, R.J.; Zhang, F.Z.; Hu, J.S. Co@N-CNTs Derived from Triple-Role CoAl-Layered Double Hydroxide as an Efficient Catalyst for Oxygen Reduction Reaction. *Carbon* **2016**, *107*, 162–170. [[CrossRef](#)]
33. Zhong, H.H.; Tian, R.; Gong, X.M.; Li, D.Q.; Tang, P.G.; Alonso-Vante, N.; Feng, Y.J. Advanced Bifunctional Electrocatalyst Generated through Cobalt Phthalocyanine Tetrasulfonate Intercalated Ni₂Fe-Layered Double Hydroxides for a Laminar Flow Unitized Regenerative Micro-Cell. *J. Power Sources* **2017**, *361*, 21–30. [[CrossRef](#)]
34. Wang, J.H.; Cui, W.; Liu, Q.; Xing, Z.C.; Asiri, A.M.; Sun, X.P. Recent Progress in Cobalt-Based Heterogeneous Catalysts for Electrochemical Water Splitting. *Adv. Mater.* **2016**, *28*, 215–230. [[CrossRef](#)] [[PubMed](#)]
35. Dai, X.F.; Qiao, J.L.; Zhou, X.J.; Shi, J.J.; Xu, P.; Zhang, L.; Zhang, J.J. Effects of Heat-Treatment and Pyridine Addition on the Catalytic Activity of Carbon-Supported Cobalt-Phthalocyanine for Oxygen Reduction Reaction in Alkaline Electrolyte. *Int. J. Electrochem. Sci.* **2013**, *8*, 3160–3175.
36. Zhao, S.; Rasimick, B.; Mustain, W.; Xu, H. Highly Durable and Active Co₃O₄ Nanocrystals Supported on Carbon Nanotubes as Bifunctional Electrocatalysts in Alkaline Media. *Appl. Catal. B* **2017**, *203*, 138–145. [[CrossRef](#)]
37. Liu, S.Y.; Li, L.J.; Ahnb, H.S.; Manthiram, A. Delineating the Roles of Co₃O₄ and N-Doped Carbon Nanoweb (CNW) in Bifunctional Co₃O₄/ CNW Catalysts for Oxygen Reduction and Oxygen Evolution Reactions. *J. Mater. Chem. A* **2015**, *3*, 11615–11623. [[CrossRef](#)]
38. Wu, Z.S.; Ren, W.C.; Wen, L.; Gao, L.B.; Zhao, J.P.; Chen, Z.P.; Zhou, G.M.; Li, F.; Cheng, H.M. Graphene Anchored with Co₃O₄ Nanoparticles as Anode of Lithium Ion Batteries with Enhanced Reversible Capacity and Cyclic Performance. *ACS Nano* **2010**, *4*, 3187–3194. [[CrossRef](#)] [[PubMed](#)]
39. Subramanian, N.P.; Kumaraguru, S.P.; Colon-Mercado, H.; Kim, H.; Popov, B.N.; Black, T.; Chen, D.A. Studies on Co-Based Catalysts Supported on Modified Carbon Substrates for PEMFC Cathodes. *J. Power Sources* **2006**, *157*, 56–63. [[CrossRef](#)]
40. Khan, M.; Tahir, M.N.; Adil, S.F.; Khan, H.U.; Siddiqui, M.R.H.; Al-Warthan, A.A.; Tremel, W. Graphene Based Metal and Metal Oxide Nanocomposites: Synthesis, Properties and their Applications. *J. Mater. Chem. A* **2015**, *3*, 18753–18808. [[CrossRef](#)]
41. Alonso-Vante, N. Platinum and Non-Platinum Nanomaterials for the Molecular Oxygen Reduction Reaction. *Chemphyschem* **2010**, *11*, 2732–2744. [[CrossRef](#)] [[PubMed](#)]
42. Tributsch, H.; Alonso-Vante, N. Energy Conversion Catalysis Using Semiconducting Transition Metal Cluster Compounds. *Nature* **1986**, *323*, 431–432.
43. Higgins, D.C.; Hassan, F.M.; Seo, M.H.; Choi, J.Y.; Hoque, M.A.; Lee, D.U.; Chen, Z. Shape-Controlled Octahedral Cobalt Disulfide Nanoparticles Supported on Nitrogen and Sulfur-Doped Graphene/Carbon Nanotube Composites for Oxygen Reduction in Acidic Electrolyte. *J. Mater. Chem. A* **2015**, *3*, 6340–6350. [[CrossRef](#)]
44. Delacôte, C.; Lewera, A.; Pisarek, M.; Kulesza, P.J.; Zelenay, P.; Alonso-Vante, N. The Effect of Diluting Ruthenium by Iron in Ru_xSe_y Catalyst for Oxygen Reduction. *Electrochim. Acta* **2010**, *55*, 7575–7580. [[CrossRef](#)]
45. Lee, K.; Zhang, L.; Zhang, J.J. Ternary Non-Noble Metal Chalcogenide (W–Co–Se) as Electrocatalyst for Oxygen Reduction Reaction. *Electrochem. Commun.* **2007**, *9*, 1704–1708. [[CrossRef](#)]

46. Zhao, C.; Li, D.Q.; Feng, Y.J. Size-Controlled Hydrothermal Synthesis and High Electrocatalytic Performance of CoS₂ Nanocatalysts as Non-Precious Metal Cathode Materials for Fuel Cells. *J. Mater. Chem. A* **2013**, *1*, 5741–5746. [[CrossRef](#)]
47. Alonso-Vante, N.; Malakhov, I.V.; Nikitenko, S.G.; Savinova, E.R.; Kochubey, D.I. The Structure Analysis of the Active Centers of Ru-containing Electrocatalysts for the Oxygen Reduction. An in Situ EXAFS Study. *Electrochim. Acta* **2002**, *47*, 3807–3814. [[CrossRef](#)]
48. Behret, H.; Binder, H.; Sandstede, G. Electrocatalytic Oxygen Reduction with Thiospinels and Other Sulphides of Transition Metals. *Electrochim. Acta* **1975**, *20*, 111–117. [[CrossRef](#)]
49. Vayner, E.; Sidik, R.A.; Anderson, A.B.; Popov, B.N. Experimental and Theoretical Study of Cobalt Selenide as a Catalyst for O₂ Electroreduction. *J. Phys. Chem. C* **2017**, *111*, 10508–10513. [[CrossRef](#)]
50. Baresel, D.; Sarholz, W.; Scharner, P.; Schmitz, J. Transition Metal Chalcogenides as Oxygen Catalysts for Fuel Cells. *Ber. Bunsenges. Phys. Chem.* **1974**, *78*, 608–618.
51. Sidik, R.A.; Anderson, A.B. Co₉S₈ as a Catalyst for Electroreduction of O₂: Quantum Chemistry Predictions. *J. Phys. Chem. B* **2006**, *110*, 936–941. [[CrossRef](#)] [[PubMed](#)]
52. Zhu, C.Y.; Aoki, Y.; Habazaki, H. Co₉S₈ Nanoparticles Incorporated in Hierarchically Porous 3D Few-Layer Graphene-Like Carbon with S, N-Doping as Superior Electrocatalyst for Oxygen Reduction Reaction. *Part. Part. Syst. Charact.* **2017**, *34*, 1700296. [[CrossRef](#)]
53. Feng, Y.J.; Alonso-Vante, N. Structure Phase Transition and Oxygen Reduction Activity in Acidic Medium of Carbon-Supported Cobalt Selenide Nanoparticles. *ECS Trans.* **2009**, *25*, 167–173.
54. Feng, Y.J.; Alonso-Vante, N. Carbon-Supported CoSe₂ Nanoparticles for Oxygen Reduction Reaction in Acid Medium. *Fuel Cells* **2010**, *10*, 77–83.
55. Wu, G.; Chung, H.T.; Nelson, M.; Artyushkova, K.; More, K.L.; Johnston, C.M.; Zelenay, P. Graphene-Enriched Co₉S₈-N-C Non-Precious Metal Catalyst for Oxygen Reduction in Alkaline Media. *ECS Trans.* **2011**, *41*, 1709–1717.
56. Apostolova, R.D.; Shembel, E.M.; Talyosef, I.; Grinblat, J.; Markovsky, B.; Aurbach, D. Study of Electrolytic Cobalt Sulfide Co₉S₈ as an Electrode Material in Lithium Accumulator Prototypes. *Russ. J. Electrochem.* **2009**, *45*, 311–319. [[CrossRef](#)]
57. Handoko, A.D.; Deng, S.; Deng, Y.; Cheng, A.W.F.; Chan, K.W.; Tan, H.R.; Pan, Y.; Tok, E.S.; Sow, C.H.; Yeo, B.S. Enhanced Activity of H₂O₂-Treated Copper(II) Oxide Nanostructures for the Electrochemical Evolution of Oxygen. *Catal. Sci. Technol.* **2016**, *6*, 269–274. [[CrossRef](#)]
58. Antolini, E. Structural Parameters of Supported Fuel Cell Catalysts: The Effect of Particle Size, Inter-Particle Distance and Metal Loading on Catalytic Activity and Fuel Cell Performance. *Appl. Catal. B* **2016**, *181*, 298–313. [[CrossRef](#)]
59. Wang, J.X.; Inada, H.; Wu, L.J.; Zhu, Y.M.; Choi, Y.M.; Liu, P.; Zhou, W.P.; Adzic, R.R. Oxygen Reduction on Well-Defined Core-Shell Nanocatalysts: Particle Size, Facet, and Pt Shell Thickness Effects. *J. Am. Chem. Soc.* **2009**, *131*, 17298–17302. [[CrossRef](#)] [[PubMed](#)]
60. Feng, Y.J.; He, T.; Alonso-Vante, N. In Situ Free-surfactant Synthesis and ORR-electrochemistry of Carbon-Supported Co₃S₄ and CoSe₂ Nanoparticles. *Chem. Mater.* **2008**, *20*, 26–28. [[CrossRef](#)]
61. Feng, Y.J.; Alonso-Vante, N. Carbon-Supported Cubic CoSe₂ Catalysts for Oxygen Reduction Reaction in Alkaline Medium. *Electrochim. Acta* **2012**, *72*, 129–133. [[CrossRef](#)]
62. Feng, Y.J.; He, T.; Alonso-Vante, N. Oxygen Reduction Reaction on Carbon-Supported CoSe₂ Nanoparticles in an Acidic Medium. *Electrochim. Acta* **2009**, *54*, 5252–5256. [[CrossRef](#)]
63. Wood, K.N.; O’Hayre, R.; Pylypenko, S. Recent Progress on Nitrogen/Carbon Structures Designed for Use in Energy and Sustainability Applications. *Energy Environ. Sci.* **2014**, *7*, 1212–1249. [[CrossRef](#)]
64. Zhou, W.J.; Lu, L.; Zhou, K.; Yang, L.J.; Ke, Y.T.; Tang, Z.H.; Chen, S.W. CoSe₂ Nanoparticles Embedded Defective Carbon Nanotubes Derived from MOFs as Efficient Electrocatalyst for Hydrogen Evolution Reaction. *Nano Energy* **2016**, *28*, 143–150. [[CrossRef](#)]
65. Alonso-Vante, N. Photocatalysis an Enhancer of Electrocatalytic Process, Current Opinion in Electrochemistry. *Curr. Opin. Electrochem.* **2018**, *9*, 114–120. [[CrossRef](#)]
66. Unni, S.M.; Mora-Hernandez, J.M.; Kurungot, S.; Alonso-Vante, N. CoSe₂ Supported on Nitrogen-Doped Carbon Nanohorns as a Methanol-Tolerant Cathode for Air-Breathing Microlaminar Flow Fuel Cells. *ChemElectroChem* **2015**, *2*, 1339–1345. [[CrossRef](#)]

67. García-Rosado, I.J.; Uribe-Calderón, J.; Alonso-Vante, N. Nitrogen-Doped Reduced Graphite Oxide as a Support for CoSe Electrocatalyst for Oxygen Reduction Reaction in Alkaline Media. *J. Electrochem. Soc.* **2017**, *164*, F658–F666. [[CrossRef](#)]
68. Zhu, A.Q.; Tan, P.F.; Qiao, L.L.; Liu, Y.; Ma, Y.J.; Pan, J. Sulphur and Nitrogen Dual-Doped Mesoporous Carbon Hybrid Coupling with Graphite Coated Cobalt and Cobalt Sulfide Nanoparticles: Rational Synthesis and Advanced Multifunctional Electrochemical Properties. *J. Colloid Interface Sci.* **2018**, *509*, 254–264. [[CrossRef](#)] [[PubMed](#)]
69. Hu, H.; Han, L.; Yu, M.; Wang, Z.Y.; Lou, X.W. Metal–Organic-Framework-Engaged Formation of Co Nanoparticle-Embedded Carbon@Co₉S₈ Double-Shelled Nanocages for Efficient Oxygen Reduction. *Energy Environ. Sci.* **2016**, *9*, 107–111. [[CrossRef](#)]
70. Chen, B.L.; Li, R.; Ma, G.P.; Gou, X.L.; Zhu, Y.Q.; Xia, Y.D. Cobalt Sulfide/N, S Codoped Porous Carbon Core-Shell Nanocomposites as Superior Bifunctional Electrocatalysts for Oxygen Reduction and Evolution Reactions. *Nanoscale* **2015**, *7*, 20674–20684. [[CrossRef](#)] [[PubMed](#)]
71. Tao, L.Q.; Zai, J.T.; Wang, K.X.; Zhang, H.J.; Xu, M.; Shen, J.; Su, Y.Z.; Qian, X.F. Co₃O₄ Nanorods/Graphene Nanosheets Nanocomposites for Lithium Ion Batteries with Improved Reversible Capacity and Cycle Stability. *J. Power Sources* **2012**, *202*, 230–235. [[CrossRef](#)]
72. Bai, G.M.; Dai, H.X.; Deng, J.G.; Liu, Y.X.; Wang, F.; Zhao, Z.X.; Qiu, W.G.; Au, C.T. Porous Co₃O₄ Nanowires and Nanorods: Highly Active Catalysts for the Combustion of Toluene. *Appl. Catal. A* **2013**, *450*, 42–49. [[CrossRef](#)]
73. Liu, J.P.; Jiang, J.; Cheng, C.W.; Li, H.X.; Zhang, J.X.; Gong, H.; Fan, H.J. Co₃O₄ Nanowire@MnO₂ Ultrathin Nanosheet Core/Shell Arrays: A New Class of High-Performance Pseudocapacitive Materials. *Adv. Mater.* **2011**, *23*, 2076–2081. [[CrossRef](#)] [[PubMed](#)]
74. Wang, Y.Y.; Lei, Y.; Li, J.; Gu, L.; Yuan, H.Y.; Xiao, D. Synthesis of 3D-Nanonet Hollow Structured Co₃O₄ for High Capacity Supercapacitor. *ACS Appl. Mater. Interfaces* **2014**, *6*, 6739–6747. [[CrossRef](#)] [[PubMed](#)]
75. Singh, S.K.; Dhavale, V.M.; Kurungot, S. Surface-Tuned Co₃O₄ Nanoparticles Dispersed on Nitrogen-Doped Graphene as an Efficient Cathode Electrocatalyst for Mechanical Rechargeable Zinc-Air Battery Application. *ACS Appl. Mater. Interfaces* **2015**, *7*, 21138–21149. [[CrossRef](#)] [[PubMed](#)]
76. Jia, X.D.; Gao, S.J.; Liu, T.Y.; Li, D.Q.; Tang, P.G.; Feng, Y.J. Controllable Synthesis and Bi-Functional Electrocatalytic Performance towards Oxygen Electrode Reactions of Co₃O₄/N-RGO Composites. *Electrochim. Acta* **2017**, *226*, 104–112. [[CrossRef](#)]
77. Liu, J.; Jiang, L.H.; Zhang, B.S.; Jin, J.T.; Su, D.S.; Wang, S.L.; Sun, G.Q. Controllable Synthesis of Cobalt Monoxide Nanoparticles and the Size-Dependent Activity for Oxygen Reduction Reaction. *ACS Catal.* **2014**, *4*, 2998–3001. [[CrossRef](#)]
78. Wang, J.K.; Gao, R.; Zhou, D.; Chen, Z.J.; Wu, Z.H.; Schumacher, G.; Hu, Z.B.; Liu, X.F. Boosting the Electrocatalytic Activity of Co₃O₄ Nanosheets for a Li-O₂ Battery through Modulating Inner Oxygen Vacancy and Exterior Co³⁺/Co²⁺ Ratio. *ACS Catal.* **2017**, *7*, 6533–6541. [[CrossRef](#)]
79. Xu, J.B.; Gao, P.; Zhao, T.S. Non-Precious Co₃O₄ Nano-Rod Electrocatalyst for Oxygen Reduction Reaction in Anion-Exchange Membrane Fuel Cells. *Energy Environ. Sci.* **2012**, *5*, 5333–5339. [[CrossRef](#)]
80. Odedairo, T.; Yan, X.C.; Ma, J.; Jiao, Y.L.; Yao, X.D.; Du, A.J.; Zhu, Z.H. Nanosheets Co₃O₄ Interleaved with Graphene for Highly Efficient Oxygen Reduction. *ACS Appl. Mater. Interfaces* **2015**, *7*, 21373–21380. [[CrossRef](#)] [[PubMed](#)]
81. Chen, Z.Y.; Li, Y.N.; Wang, M.Q.; Xu, M.W.; Bao, S.J. Hollow Co₃O₄ Nanocages Decorated Graphene Aerogels Derived from Carbon Wrapped Nano-Co for Efficient Oxygen Reduction Reaction. *ChemistrySelect* **2017**, *2*, 6359–6363. [[CrossRef](#)]
82. Wu, Z.X.; Wang, J.; Han, L.L.; Lin, R.Q.; Liu, H.F.; Xin, H.L.L.; Wang, D.L. Supramolecular Gel-Assisted Synthesis of Double Shelled Co@CoO@N-C/C Nanoparticles with Synergistic Electrocatalytic Activity for the Oxygen Reduction Reaction. *Nanoscale* **2016**, *8*, 4681–4687. [[CrossRef](#)] [[PubMed](#)]
83. Wang, D.D.; Chen, X.; Evans, D.G.; Yang, W.S. Well-Dispersed Co₃O₄/Co₂MnO₄ Nanocomposites as a Synergistic Bifunctional Catalyst for Oxygen Reduction and Oxygen Evolution Reactions. *Nanoscale* **2013**, *5*, 5312–5315. [[CrossRef](#)] [[PubMed](#)]
84. Huang, W.; Zhong, H.H.; Li, D.Q.; Tang, P.G.; Feng, Y.J. Reduced Graphene Oxide Supported CoO/MnO₂ Electrocatalysts from Layered Double Hydroxides for Oxygen Reduction Reaction. *Electrochim. Acta* **2015**, *173*, 575–580. [[CrossRef](#)]

85. Wang, Y.L.; Wang, Z.C.; Wu, X.Q.; Liu, X.W.; Li, M.G. Synergistic Effect between Strongly Coupled CoAl Layered Double Hydroxides and Graphene for the Electrocatalytic Reduction of Oxygen. *Electrochim. Acta* **2016**, *192*, 196–204. [[CrossRef](#)]
86. Huo, R.J.; Jiang, W.J.; Xu, S.L.; Zhang, F.Z.; Hu, J.S. Co/CoO/CoFe₂O₄/G Nanocomposites Derived from Layered Double Hydroxides towards Mass Production of Efficient Pt-Free Electrocatalysts for Oxygen Reduction Reaction. *Nanoscale* **2014**, *6*, 203–206. [[CrossRef](#)] [[PubMed](#)]
87. Jasinski, R. A New Fuel Cell Cathode Catalyst. *Nature* **1964**, *21*, 1212–1213. [[CrossRef](#)]
88. Wu, G.; More, K.L.; Johnston, C.M.; Zelenay, P. High-Performance Electrocatalysts for Oxygen Reduction Derived from Polyaniline, Iron, and Cobalt. *Science* **2011**, *332*, 443–447. [[CrossRef](#)] [[PubMed](#)]
89. Kothandaraman, R.; Nallathambi, V.; Artyushkova, K.; Barton, S.C. Non-Precious Oxygen Reduction Catalysts Prepared by High-Pressure Pyrolysis for Low-Temperature Fuel Cells. *Appl. Catal. B* **2009**, *92*, 209–216. [[CrossRef](#)]
90. Bashyam, R.; Zelenay, P. A Class of Non-Precious Metal Composite Catalysts for Fuel Cells. *Nature* **2006**, *443*, 63–66. [[CrossRef](#)] [[PubMed](#)]
91. Morozan, A.; Jegou, P.; Jusselme, B.; Palacin, S. Electrochemical Performance of Annealed Cobalt-Benzotriazole/CNTs Catalysts towards the Oxygen Reduction Reaction. *Phys. Chem. Chem. Phys.* **2011**, *13*, 21600–21607. [[CrossRef](#)] [[PubMed](#)]
92. Chen, X.; Li, F.; Zhang, N.L.; An, L.; Xia, D.G. Mechanism of Oxygen Reduction Reaction Catalyzed by Fe(Co)-N_x/C. *Phys. Chem. Chem. Phys.* **2013**, *15*, 19330–19336. [[CrossRef](#)] [[PubMed](#)]
93. Jia, Q.Y.; Ramaswamy, N.; Tylus, U.; Strickland, K.; Li, J.K.; Serov, A.; Artyushkova, K.; Atanassov, P.; Anibal, J.; Gumeci, C.; et al. Spectroscopic Insights into the Nature of Active Sites in Iron–Nitrogen–Carbon Electrocatalysts for Oxygen Reduction in Acid. *Nano Energy* **2016**, *29*, 65–82. [[CrossRef](#)]
94. Wong, W.Y.; Daud, W.R.W.; Mohamad, A.B.; Kadhum, A.A.H.; Loh, K.S.; Majlan, E.H. Recent Progress in Nitrogen-Doped Carbon and its Composites as Electrocatalysts for Fuel Cell Applications. *Int. J. Hydrogen Energy* **2013**, *38*, 9370–9386. [[CrossRef](#)]
95. Niwa, H.; Horiba, K.; Harada, Y.; Oshima, M.; Ikeda, T.; Terakura, K.; Ozaki, J.; Miyata, S. X-ray Absorption Analysis of Nitrogen Contribution to Oxygen Reduction Reaction in Carbon Alloy Cathode Catalysts for Polymer Electrolyte Fuel Cells. *J. Power Sources* **2009**, *187*, 93–97. [[CrossRef](#)]
96. Hu, C.G.; Xiao, Y.; Zhao, Y.; Chen, N.; Zhang, Z.P.; Cao, M.H.; Qu, L.T. Highly Nitrogen-Doped Carbon Capsules: Scalable Preparation and High-Performance Applications in Fuel Cells and Lithium Ion Batteries. *Nanoscale* **2013**, *5*, 2726–2733. [[CrossRef](#)] [[PubMed](#)]
97. Kattel, S.; Atanassov, P.; Kiefer, B. Catalytic Activity of Co–N_x/C Electrocatalysts for Oxygen Reduction Reaction: A Density Functional Theory Study. *Phys. Chem. Chem. Phys.* **2013**, *15*, 148–153. [[CrossRef](#)] [[PubMed](#)]
98. Yin, P.Q.; Yao, T.; Wu, Y.; Zheng, L.R.; Lin, Y.; Liu, W.; Ju, H.X.; Zhu, J.F.; Hong, X.; Deng, Z.X.; et al. Single Cobalt Atoms with Precise N-Coordination as Superior Oxygen Reduction Reaction Catalysts. *Angew. Chem. Int. Ed. Engl.* **2016**, *55*, 10800–10805. [[CrossRef](#)] [[PubMed](#)]
99. Amiin, I.S.; Liu, X.B.; Pu, Z.H.; Li, W.Q.; Li, Q.D.; Zhang, J.; Tang, H.L.; Zhang, H.N.; Mu, S.C. From 3D ZIF Nanocrystals to Co–N_x/C Nanorod Array Electrocatalysts for ORR, OER, and Zn–Air Batteries. *Adv. Funct. Mater.* **2018**, *28*, 1704638–1704646. [[CrossRef](#)]
100. Peng, H.L.; Liu, F.F.; Liu, X.J.; Liao, S.J.; You, C.H.; Tian, X.L.; Nan, H.X.; Luo, F.; Song, H.Y.; Fu, Z.Y.; et al. Effect of Transition Metals on the Structure and Performance of the Doped Carbon Catalysts Derived From Polyaniline and Melamine for ORR Application. *ACS Catal.* **2014**, *4*, 3797–3805. [[CrossRef](#)]
101. Wiesener, K. N₄-Chelates as Electrocatalyst for Cathodic Oxygen Reduction. *Electrochim. Acta* **1986**, *31*, 1073–1078. [[CrossRef](#)]
102. Masa, J.; Xia, W.; Muhler, M.; Schuhmann, W. On the Role of Metals in Nitrogen-Doped Carbon Electrocatalysts for Oxygen Reduction. *Angew. Chem. Int. Ed. Engl.* **2015**, *54*, 10102–10120. [[CrossRef](#)] [[PubMed](#)]
103. Bagotzky, V.S.; Tarasevich, M.R.; Radyushkina, K.A.; Levina, O.A.; Andrusyova, S.I. Electrocatalysis of the Oxygen Reduction Process on Metal Chelates in Acid Electrolyte. *J. Power Sources* **1978**, *2*, 233–240. [[CrossRef](#)]
104. Wiesener, K.; Ohms, D.; Neumann, V.; Franke, R. N₄ Macrocycles as Electrocatalysts for the Cathodic Reduction of Oxygen. *Mater. Chem. Phys.* **1989**, *22*, 457–475. [[CrossRef](#)]

105. Liu, Y.Y.; Yue, X.P.; Li, K.X.; Qiao, J.L.; Wilkinson, D.P.; Zhang, J.J. PEM Fuel Cell Electrocatalysts Based on Transition Metal Macrocyclic Compounds. *Coord. Chem. Rev.* **2016**, *315*, 153–177. [[CrossRef](#)]
106. Osmieri, L.; Videla, A.H.A.M.; Specchia, S. Activity of Co–N Multi Walled Carbon Nanotubes Electrocatalysts for Oxygen Reduction Reaction in Acid Conditions. *J. Power Sources* **2015**, *278*, 296–307. [[CrossRef](#)]
107. Nallathambi, V.; Lee, J.W.; Kumaraguru, S.P.; Wu, G.; Popov, B.N. Development of High Performance Carbon Composite Catalyst for Oxygen Reduction Reaction in PEM Proton Exchange Membrane Fuel Cells. *J. Power Sources* **2008**, *183*, 34–42. [[CrossRef](#)]
108. Lalande, G.; Côté, R.; Tamizhmani, G.; Guay, D.; Dodelet, J.P.; Dignard-Bailey, L.; Weng, L.T.; Bertrand, P. Physical, Chemical and Electrochemical Characterization of Heat-Treated Tetracarboxylic Cobalt Phthalocyanine Adsorbed on Carbon Black as Electrocatalyst for Oxygen Reduction in Polymer Electrolyte Fuel Cells. *Electrochim. Acta* **1995**, *40*, 2635–2646. [[CrossRef](#)]
109. Weng, L.T.; Bertrand, P.; Lalande, G.; Guay, D.; Dodelet, J.P. Surface Characterization by Time-of-Flight SIMS of a Catalyst for Oxygen Electroreduction: Pyrolyzed Cobalt Phthalocyanine-on-Carbon Black. *Appl. Surf. Sci.* **1985**, *84*, 9–21. [[CrossRef](#)]
110. Jahnke, H.; Schönborn, M.; Zimmermann, G. Organic Dyestuffs as Catalysts for Fuel Cells. *Top. Curr. Chem.* **1976**, *61*, 133–181. [[PubMed](#)]
111. Kong, A.G.; Kong, Y.Y.; Zhu, X.F.; Han, Z.; Shan, Y.K. Ordered Mesoporous Fe (or Co)–N–Graphitic Carbons as Excellent Non-Precious-Metal Electrocatalysts for Oxygen Reduction. *Carbon* **2014**, *78*, 49–59. [[CrossRef](#)]
112. Tang, C.; Wang, B.; Wang, H.F.; Zhang, Q. Defect Engineering toward Atomic Co–N_x–C in Hierarchical Graphene for Rechargeable Flexible Solid Zn–Air Batteries. *Adv. Mater.* **2017**, *29*, 1703185–1703191. [[CrossRef](#)] [[PubMed](#)]
113. Zhang, L.L.; Wang, A.Q.; Wang, W.T.; Huang, Y.Q.; Liu, X.Y.; Miao, S.; Liu, J.Y.; Zhang, T. Co–N–C Catalyst for C–C Coupling Reactions: On the Catalytic Performance and Active Sites. *ACS Catal.* **2015**, *5*, 6563–6572. [[CrossRef](#)]
114. Hu, F.; Yang, H.C.; Wang, C.H.; Zhang, Y.J.; Lu, H.; Wang, Q.B. Co–N–Doped Mesoporous Carbon Hollow Spheres as Highly Efficient Electrocatalysts for Oxygen Reduction Reaction. *Small* **2017**, *13*, 1602507–1602514. [[CrossRef](#)] [[PubMed](#)]
115. Cai, S.C.; Meng, Z.H.; Tang, H.L.; Wang, Y.; Tsiakaras, P. 3D Co–N–doped Hollow Carbon Spheres as Excellent Bifunctional Electrocatalysts for Oxygen Reduction Reaction and Oxygen Evolution Reaction. *Appl. Catal. B* **2017**, *217*, 477–484. [[CrossRef](#)]
116. Aijaz, A.; Masa, J.; Rosler, C.; Xia, W.; Weide, P.; Botz, A.J.R.; Fischer, R.A.; Schuhmann, W.; Muhler, M. Co@Co₃O₄ Encapsulated in Carbon Nanotube–Grafted Nitrogen–Doped Carbon Polyhedra as an Advanced Bifunctional Oxygen Electrode. *Angew. Chem. Int. Ed. Engl.* **2016**, *55*, 4087–4091. [[CrossRef](#)] [[PubMed](#)]
117. Kuang, M.; Wang, Q.; Han, P.; Zheng, G.F. Cu, Co–Embedded N–Enriched Mesoporous Carbon for Efficient Oxygen Reduction and Hydrogen Evolution Reactions. *Adv. Energy Mater.* **2017**, *7*, 1700193–1700200. [[CrossRef](#)]
118. Lin, Q.P.; Bu, X.H.; Kong, A.G.; Mao, C.Y.; Bu, F.; Feng, P.Y. Heterometal–Embedded Organic Conjugate Frameworks from Alternating Monomeric Iron and Cobalt Metalloporphyrins and Their Application in Design of Porous Carbon Catalysts. *Adv. Mater.* **2015**, *27*, 3431–3436. [[CrossRef](#)] [[PubMed](#)]
119. Fan, X.J.; Peng, Z.W.; Ye, R.Q.; Zhou, H.Q.; Guo, X. M₃C (M: Fe, Co, Ni) Nanocrystals Encased in Graphene Nanoribbons: An Active and Stable Bifunctional Electrocatalyst for Oxygen Reduction and Hydrogen Evolution Reactions. *ACS Nano* **2015**, *9*, 7407–7418. [[CrossRef](#)] [[PubMed](#)]
120. Zhu, L.; Teo, M.; Wong, P.C.; Wong, K.C.; Narita, I.; Ernst, F.; Mitchell, K.A.R.; Campbell, S.A. Synthesis, Characterization of a CoSe₂ Catalyst for the Oxygen Reduction Reaction. *Appl. Catal. A* **2010**, *386*, 157–165. [[CrossRef](#)]
121. Qiao, X.C.; Jin, J.T.; Fan, H.B.; Li, Y.W.; Liao, S.J. In Situ Growth of Cobalt Sulfide Hollow Nanospheres Embedded in Nitrogen and Sulfur Co–doped Graphene Nanoholes as a Highly Active Electrocatalyst for Oxygen Reduction and Evolution. *J. Mater. Chem. A* **2017**, *5*, 12354–12360. [[CrossRef](#)]
122. Liang, H.; Li, C.W.; Chen, T.; Cui, L.; Han, J.R.; Peng, Z.; Liu, J.Q. Facile Preparation of Three-Dimensional Co_{1-x}S/Sulfur and Nitrogen–Codoped Graphene/Carbon Foam for Highly Efficient Oxygen Reduction Reaction. *J. Power Sources* **2018**, *378*, 699–706. [[CrossRef](#)]

123. Zhang, Y.; Li, P.W.; Yin, X.Y.; Yan, Y.; Zhan, K.; Yang, J.H.; Zhao, B. Cobalt Sulfide Supported on Nitrogen and Sulfur Dual-Doped Reduced Graphene Oxide for Highly Active Oxygen Reduction Reaction. *RSC Adv.* **2017**, *7*, 50246–50253. [[CrossRef](#)]
124. Ganesan, P.; Prabu, M.; Sanetuntikul, J.; Shanmugam, S. Cobalt Sulfide Nanoparticles Grown on Nitrogen and Sulfur Codoped Graphene Oxide: An Efficient Electrocatalyst for Oxygen Reduction and Evolution Reactions. *ACS Catal.* **2015**, *5*, 3625–3637. [[CrossRef](#)]
125. Mahmood, N.; Zhang, C.Z.; Jiang, J.; Liu, F.; Hou, Y.L. Multifunctional Co₃S₄/Graphene Composites for Lithium Ion Batteries and Oxygen Reduction Reaction. *Chem. Eur. J.* **2013**, *19*, 5183–5190. [[CrossRef](#)] [[PubMed](#)]
126. Sennu, P.; Christy, M.; Aravindan, V.; Lee, Y.G.; Nahm, K.S.; Lee, Y.S. Two-Dimensional Mesoporous Cobalt Sulfide Nanosheets as a Superior Anode for a Li-Ion Battery and a Bifunctional Electrocatalyst for the LiO₂ System. *Chem. Mater.* **2015**, *27*, 5726–5735. [[CrossRef](#)]
127. Arunchander, A.; Peera, S.G.; Giridhar, V.V.; Sahu, A.K. Synthesis of Cobalt Sulfide-Graphene as an Efficient Oxygen Reduction Catalyst in Alkaline Medium and its Application in Anion Exchange Membrane Fuel Cells. *J. Electrochem. Soc.* **2016**, *164*, F71–F80. [[CrossRef](#)]
128. Fu, S.F.; Zhu, C.Z.; Song, J.H.; Feng, S.; Du, D.; Engelhard, M.H.; Xiao, D.D.; Li, D.S.; Lin, Y.H. Two-Dimensional N, S-Codoped Carbon/Co₉S₈ Catalysts Derived from Co(OH)₂ Nanosheets for Oxygen Reduction Reaction. *ACS Appl. Mater. Interfaces* **2017**, *9*, 36755–36761. [[CrossRef](#)] [[PubMed](#)]
129. Zhou, Y.X.; Yao, H.B.; Wang, Y.; Liu, H.L.; Gao, M.R.; Shen, P.K.; Yu, S.H. Hierarchical Hollow Co₉S₈ Microspheres: Solvothermal Synthesis, Magnetic, Electrochemical, and Electrocatalytic Properties. *Chemistry* **2010**, *16*, 12000–12007. [[CrossRef](#)] [[PubMed](#)]
130. Tang, Y.P.; Jing, F.; Xu, Z.X.; Zhang, F.; Mai, Y.Y.; Wu, D.Q. Highly Crumpled Hybrids of Nitrogen/Sulfur Dual-Doped Graphene and Co₉S₈ Nanoplates as Efficient Bifunctional Oxygen Electrocatalysts. *ACS Appl. Mater. Interfaces* **2017**, *9*, 12340–12347. [[CrossRef](#)] [[PubMed](#)]
131. Mattioli, G.; Giannozzi, P.; Bonapasta, A.A.; Guidoni, L. Reaction Pathways for Oxygen Evolution Promoted by Cobalt Catalyst. *J. Am. Chem. Soc.* **2013**, *135*, 15353–15363. [[CrossRef](#)] [[PubMed](#)]
132. García-Mota, M.; Bajdich, M.; Viswanathan, V.; Vojvodic, A.; Bell, A.T.; Nørskov, J.K. Importance of Correlation in Determining Electrocatalytic Oxygen Evolution Activity on Cobalt Oxides. *J. Phys. Chem. C* **2012**, *116*, 21077–21082. [[CrossRef](#)]
133. Bajdich, M.; Garcia-Mota, M.; Vojvodic, A.; Nørskov, J.K.; Bell, A.T. Theoretical Investigation of the Activity of Cobalt Oxides for the Electrochemical Oxidation of Water. *J. Am. Chem. Soc.* **2013**, *135*, 13521–13530. [[CrossRef](#)] [[PubMed](#)]
134. Liu, Y.W.; Cheng, H.; Lyu, M.J.; Fan, S.J.; Liu, Q.H.; Zhang, W.S.; Zhi, Y.D.; Wang, C.M.; Xiao, C.; Wei, S.Q.; et al. Low Overpotential in Vacancy-Rich Ultrathin CoSe₂ Nanosheets for Water Oxidation. *J. Am. Chem. Soc.* **2014**, *136*, 15670–15675. [[CrossRef](#)] [[PubMed](#)]
135. Gao, M.R.; Cao, X.; Gao, Q.; Xu, Y.F.; Zheng, Y.R.; Jiang, J.; Yu, S. Nitrogen-Doped Graphene Supported CoSe₂ Nanobelt Composite Catalyst for Efficient Water Oxidation. *ACS Nano* **2014**, *8*, 3970–3978. [[CrossRef](#)] [[PubMed](#)]
136. Guo, Y.X.; Yao, Z.Y.; Shang, C.S.; Wang, E.K. Amorphous Co₂B Grown on CoSe₂ Nanosheets as a Hybrid Catalyst for Efficient Overall Water Splitting in Alkaline Medium. *ACS Appl. Mater. Interfaces* **2017**, *9*, 39312–39317. [[CrossRef](#)] [[PubMed](#)]
137. Lyons, M.E.G.; Brandon, M.P. The Oxygen Evolution Reaction on Passive Oxide Covered Transition Metal Electrodes in Alkaline Solution. Part III - Iron. *Int. J. Electrochem. Sci.* **2008**, *3*, 1425–1462.
138. Yeo, B.S.; Bell, A.T. Enhanced Activity of Gold-Supported Cobalt Oxide for the Electrochemical Evolution of Oxygen. *J. Am. Chem. Soc.* **2011**, *133*, 5587–5593. [[CrossRef](#)] [[PubMed](#)]
139. Simmons, G.W.; Kellerman, E.; Leidheiser, H.J. In Situ Studies of the Passivation and Anodic Oxidation of Cobalt by Emission Moessbauer Spectroscopy. *J. Electrochem. Soc.* **1976**, *123*, 1276–1284. [[CrossRef](#)]
140. Liu, J.; Liu, Y.; Liu, N.Y.; Han, Y.Z.; Zhang, X.; Huang, H.; Lifshitz, Y.; Lee, S.T.; Zhong, J.; Kang, Z.H. Metal-Free Efficient Photocatalyst for Stable Visible Water Splitting via A Two-Electron Pathway. *Science* **2015**, *347*, 970–974. [[CrossRef](#)] [[PubMed](#)]
141. Barkaoui, S.; Haddaoui, M.; Dhaouadi, H.; Raouafi, N.; Touati, F. Hydrothermal Synthesis of Urchin-Like Co₃O₄ Nanostructures and their Electrochemical Sensing Performance of H₂O₂. *J. Solid State Chem.* **2015**, *228*, 226–231. [[CrossRef](#)]

142. Du, S.C.; Ren, Z.Y.; Qu, Y.; Wu, J.; Xi, W.; Zhu, J.Q.; Fu, H.G. Co₃O₄ Nanosheets as a High-Performance Catalyst for Oxygen Evolution Proceeding via a Double Two-Electron Process. *Chem. Commun.* **2016**, *52*, 6705–6708. [[CrossRef](#)] [[PubMed](#)]
143. Wang, Y.C.; Zhou, T.; Jiang, K.; Da, P.M.; Peng, Z.; Tang, J.; Kong, B.A.; Cai, W.B.; Yang, Z.Q.; Zheng, G.F. Reduced Mesoporous Co₃O₄ Nanowires as Efficient Water Oxidation Electrocatalysts and Supercapacitor Electrodes. *Adv. Energy Mater.* **2014**, *4*, 1400696–1400702. [[CrossRef](#)]
144. Xia, Y.S.; Dai, H.X.; Jiang, H.Y.; Zhang, L. Three-Dimensional Ordered Mesoporous Cobalt Oxides: Highly Active Catalysts for the Oxidation of Toluene and Methanol. *Catal. Commun.* **2010**, *11*, 1171–1175. [[CrossRef](#)]
145. Zhao, Y.F.; Chen, S.Q.; Sun, B.; Su, D.W.; Huang, X.D.; Liu, H.; Yan, Y.M.; Sun, K.N.; Wang, G.X. Graphene-Co₃O₄ Nanocomposite as Electrocatalyst with High Performance for Oxygen Evolution Reaction. *Sci. Rep.* **2015**, *5*, 7629–7635. [[CrossRef](#)] [[PubMed](#)]
146. Jadhav, A.R.; Bandal, H.A.; Tamboli, A.H.; Kim, H. Environment Friendly Hydrothermal Synthesis of Carbon-Co₃O₄ Nanorods Composite as an Efficient Catalyst for Oxygen Evolution Reaction. *J. Energy Chem.* **2017**, *26*, 695–702. [[CrossRef](#)]
147. Du, S.C.; Ren, Z.Y.; Zhang, J.; Wu, J.; Xi, W.; Zhu, J.Q.; Fu, H.G. Co₃O₄ Nanocrystal Ink Printed on Carbon Fiber Paper as a Large-Area Electrode for Electrochemical Water Splitting. *Chem. Commun.* **2015**, *51*, 8066–8069. [[CrossRef](#)] [[PubMed](#)]
148. Wei, Y.C.; Ren, X.; Ma, H.M.; Sun, X.; Zhang, Y.; Kuang, X.; Yan, T.; Ju, H.X.; Wu, D.; Wei, Q. CoC₂O₄·2H₂O Derived Co₃O₄ Nanorods Array: A High-Efficiency 1D Electrocatalyst for Alkaline Oxygen Evolution Reaction. *Chem. Commun.* **2018**, *54*, 1533–1536. [[CrossRef](#)] [[PubMed](#)]
149. Nai, J.W.; Yin, H.J.; You, T.T.; Zheng, L.R.; Zhang, J.; Wang, P.X.; Jin, Z.; Tian, Y.; Liu, J.Z.; Tang, Z.Y.; et al. Efficient Electrocatalytic Water Oxidation by Using Amorphous Ni-Co Double Hydroxides Nanocages. *Adv. Energy Mater.* **2015**, *5*, 1401880–1401887. [[CrossRef](#)]
150. Surendranath, Y.; Lutterman, D.A.; Liu, Y.; Nocera, D.G. Nucleation, Growth, and Repair of Acobalt-Based Oxygen Evolving Catalyst. *J. Am. Chem. Soc.* **2012**, *134*, 6326–6336. [[CrossRef](#)] [[PubMed](#)]
151. Ni, B.; Wang, X. Edge Overgrowth of Spiral Bimetallic Hydroxides Ultrathin-Nanosheets for Water Oxidation. *Chem. Sci.* **2015**, *6*, 3572–3576. [[CrossRef](#)] [[PubMed](#)]
152. Wu, J.; Ren, Z.Y.; Du, S.C.; Kong, L.J.; Liu, B.W.; Xi, W.; Zhu, J.Q.; Fu, H.G. A Highly Active Oxygen Evolution Electrocatalyst: Ultrathin CoNi Double Hydroxide/CoO Nanosheets Synthesized via Interface-Directed Assembly. *Nano Res.* **2016**, *9*, 713–725. [[CrossRef](#)]
153. Maiyalagan, T.; Jarvis, K.A.; Therese, S.; Ferreira, P.J.; Manthiram, A. Spinel-Type Lithium Cobalt Oxide as a Bifunctional Electrocatalyst for the Oxygen Evolution and Oxygen Reduction Reactions. *Nat. Commun.* **2014**, *5*, 3949–3956. [[CrossRef](#)] [[PubMed](#)]
154. Qian, L.; Lu, Z.Y.; Xu, T.H.; Wu, X.C.; Tian, Y.; Li, Y.P.; Huo, Z.Y.; Sun, X.M.; Duan, X. Ternary Layered Double Hydroxides as High-Performance Bifunctional Materials for Oxygen Electrocatalysis. *Adv. Energy Mater.* **2015**, *5*, 1500245–1500250. [[CrossRef](#)]
155. Grimaud, A.; May, K.J.; Carlton, C.E.; Lee, Y.L.; Risch, M.; Hong, W.T.; Zhou, J.G.; Shao-Horn, Y. Double Perovskites as a Family of Highly Active Catalysts for Oxygen Evolution in Alkaline Solution. *Nat. Commun.* **2013**, *4*, 2439–2745. [[CrossRef](#)] [[PubMed](#)]
156. Lukowski, M.A.; Daniel, A.S.; Meng, F.; Forticaux, A.; Li, L.S.; Jin, S. Enhanced Hydrogen Evolution Catalysis from Chemically Exfoliated Metallic MoS₂ Nanosheets. *J. Am. Chem. Soc.* **2013**, *135*, 10274–10277. [[CrossRef](#)] [[PubMed](#)]
157. Voiry, D.; Yamaguchi, H.; Li, J.W.; Silva, R.; Alves, D.C.B.; Fujita, T.; Chen, M.W.; Asefa, T.; Shenoy, V.B.; Eda, G.; et al. Enhanced Catalytic Activity in Strained Chemically Exfoliated WS₂ Nanosheets for Hydrogen Evolution. *Nat. Mater.* **2013**, *12*, 850–855. [[CrossRef](#)] [[PubMed](#)]
158. Yu, L.; Yan, Y.X.; Liu, Q.; Wang, J.; Yang, B.; Wang, B.; Jing, X.Y.; Liu, L.H. Exfoliation at Room Temperature for Improving Electrochemical Performance for Supercapacitors of Layered MnO₂. *J. Electrochem. Soc.* **2013**, *161*, E1–E5. [[CrossRef](#)]
159. Song, F.; Hu, X.L. Exfoliation of Layered Double Hydroxides for Enhanced Oxygen Evolution Catalysis. *Nat. Commun.* **2014**, *5*, 4477–4485. [[CrossRef](#)] [[PubMed](#)]
160. Liang, H.F.; Meng, F.; Caban-Acevedo, M.; Li, L.S.; Forticaux, A.; Xiu, L.C.; Wang, Z.C.; Jin, S. Hydrothermal Continuous Flow Synthesis and Exfoliation of NiCo Layered Double Hydroxide Nanosheets for Enhanced Oxygen Evolution Catalysis. *Nano Lett.* **2015**, *15*, 1421–1427. [[CrossRef](#)] [[PubMed](#)]

161. Zhao, S.; Yan, L.T.; Luo, H.; Mustain, W.; Xu, H. Recent Progress and Perspectives of Bifunctional Oxygen Reduction/Evolution Catalyst Development for Regenerative Anion Exchange Membrane Fuel Cells. *Nano Energy* **2018**, *47*, 172–198. [[CrossRef](#)]
162. Mamlouk, M.; Kumar, S.M.S.; Gouerec, P.; Scott, K. Electrochemical and Fuel Cell Evaluation of Co Based Catalyst for Oxygen Reduction in Anion Exchange Polymer Membrane Fuel Cells. *J. Power Sources* **2011**, *196*, 7594–7600. [[CrossRef](#)]
163. Wu, X.; Scott, K. A Non-Precious Metal Bifunctional Oxygen Electrode for Alkaline Anion Exchange Membrane Cells. *J. Power Sources* **2012**, *206*, 14–19. [[CrossRef](#)]
164. Kong, D.S.; Cha, J.J.; Wang, H.T.; Lee, H.R.; Cui, Y. First-Row Transition Metal Dichalcogenide Catalysts for Hydrogen Evolution Reaction. *Energy Environ. Sci.* **2013**, *6*, 3553–3558. [[CrossRef](#)]
165. Anantharaj, S.; Ede, S.R.; Sakthikumar, K.; Karthick, K.; Mishra, S.; Kundu, S. Recent Trends and Perspectives in Electrochemical Water Splitting with an Emphasis on Sulfide, Selenide, and Phosphide Catalysts of Fe, Co, and Ni: A Review. *ACS Catal.* **2016**, *6*, 8069–8097. [[CrossRef](#)]
166. Liu, Q.; Shi, J.L.; Hu, J.M.; Asiri, A.M.; Luo, Y.L.; Sun, X.P. CoSe₂ Nanowires Array as a 3D Electrode for Highly Efficient Electrochemical Hydrogen Evolution. *ACS Appl. Mater. Interfaces* **2015**, *7*, 3877–3881. [[CrossRef](#)] [[PubMed](#)]
167. Zhang, H.X.; Yang, B.; Wu, X.L.; Li, Z.J.; Lei, L.C.; Zhang, X.W. Polymorphic CoSe₂ with Mixed Orthorhombic and Cubic Phases for Highly Efficient Hydrogen Evolution Reaction. *ACS Appl. Mater. Interfaces* **2015**, *7*, 1772–1779. [[CrossRef](#)] [[PubMed](#)]
168. Li, H.M.; Qian, X.; Zhu, C.L.; Jiang, X.X.; Shao, L.; Hou, L.X. Template Synthesis of CoSe₂/Co₃Se₄ Nanotubes: Tuning of their Crystal Structures for Photovoltaics and Hydrogen Evolution in Alkaline Medium. *J. Mater. Chem. A* **2017**, *5*, 4513–4526. [[CrossRef](#)]
169. Wang, K.; Xi, D.; Zhou, C.J.; Shi, Z.Q.; Xia, H.Y.; Liu, G.W.; Qiao, G.J. CoSe₂ Necklace-Like Nanowires Supported by Carbon Fiber Paper: A 3D Integrated Electrode for the Hydrogen Evolution Reaction. *J. Mater. Chem. A* **2015**, *3*, 9415–9420. [[CrossRef](#)]
170. Yue, H.H.; Yu, B.; Qi, F.; Zhou, J.H.; Wang, X.Q.; Zheng, B.J.; Zhang, W.L.; Li, Y.R.; Chen, Y.F. Interwoven CoSe₂/CNTs Hybrid as a Highly Efficient and Stable Electrocatalyst for Hydrogen Evolution Reaction. *Electrochim. Acta* **2017**, *253*, 200–207. [[CrossRef](#)]
171. Kim, J.K.; Park, G.D.; Kim, J.H.; Park, S.K.; Kang, Y.C. Rational Design and Synthesis of Extremely Efficient Macroporous CoSe₂-CNT Composite Microspheres for Hydrogen Evolution Reaction. *Small* **2017**, *13*, 1700068. [[CrossRef](#)] [[PubMed](#)]
172. Dai, C.; Tian, X.K.; Nie, Y.L.; Tian, C.; Yang, C.; Zhou, Z.X.; Li, Y.; Gao, X.Y. Successful Synthesis of 3D CoSe₂ Hollow Microspheres with High Surface Roughness and its Excellent Performance in Catalytic Hydrogen Evolution Reaction. *Chem. Eng. J.* **2017**, *321*, 105–112. [[CrossRef](#)]
173. Xiao, H.Q.; Wang, S.T.; Wang, C.; Li, Y.Y.; Zhang, H.R.; Wang, Z.J.; Zhou, Y.; An, C.H.; Zhang, J. Lamellar Structured CoSe₂ Nanosheets Directly Arrayed on Ti Plate as an Efficient Electrochemical Catalyst for Hydrogen Evolution. *Electrochim. Acta* **2016**, *217*, 156–162. [[CrossRef](#)]
174. Di, J.; Yan, C.; Handoko, A.D.; Seh, Z.W.; Li, H.M.; Liu, Z. Ultrathin Two-Dimensional Materials for Photo- and Electrocatalytic Hydrogen Evolution. *Mater. Today* **2018**, *21*, 749–770. [[CrossRef](#)]
175. Liu, Y.W.; Hua, X.M.; Xiao, C.; Zhou, T.F.; Huang, P.C.; Guo, Z.P.; Pan, B.C.; Xie, Y. Heterogeneous Spin States in Ultrathin Nanosheet Inducing Subtle Lattice Distortion for Efficiently Triggering Hydrogen Evolution. *J. Am. Chem. Soc.* **2016**, *138*, 5087–5092. [[CrossRef](#)] [[PubMed](#)]
176. Yang, Y.Y.; Li, F.; Li, W.Z.; Gao, W.B.; Wen, H.; Li, J.; Hu, Y.P.; Luo, Y.T.; Li, R. Porous CoS₂ Nanostructures Based on ZIF-9 Supported on Reduced Graphene Oxide: Favourable Electrocatalysis for Hydrogen Evolution Reaction. *Int. J. Hydrogen Energy* **2017**, *42*, 6665–6673. [[CrossRef](#)]
177. Zhang, X.; Liu, S.W.; Zang, Y.P.; Liu, R.R.; Liu, G.Q.; Wang, G.Z.; Zhang, Y.X.; Zhang, H.M.; Zhao, H.J. Co/Co₉S₈@S, N-Doped Porous Graphene Sheets Derived from S, N Dual Organic Ligands Assembled Co-MOFs as Superior Electrocatalysts for Full Water Splitting in Alkaline Media. *Nano Energy* **2016**, *30*, 93–102. [[CrossRef](#)]
178. Lin, J.; He, J.R.; Qi, F.; Zheng, B.J.; Wang, X.Q.; Yu, B.; Zhou, K.R.; Zhang, W.L.; Li, Y.R.; Chen, Y.F. In-Situ Selenization of Co-based Metal-Organic Frameworks as a Highly Efficient Electrocatalyst for Hydrogen Evolution Reaction. *Electrochim. Acta* **2017**, *247*, 258–264. [[CrossRef](#)]

179. Zhang, H.X.; Lei, L.C.; Zhang, X.W. One-Step Synthesis of Cubic Pyrite-Type CoSe₂ at Low Temperature for Efficient Hydrogen Evolution Reaction. *RSC Adv.* **2014**, *4*, 54344–54348. [[CrossRef](#)]
180. Li, Y.Z.; Niu, S.Q.; Rakov, D.; Wang, Y.; Caban-Acevedo, M.; Zheng, S.J.; Song, B.; Xu, P. Metal Organic Framework-Derived CoPS/N-doped Carbon for Efficient Electrocatalytic Hydrogen Evolution. *Nanoscale* **2018**, *10*, 7291–7297. [[CrossRef](#)] [[PubMed](#)]
181. Li, N.; Liu, X.; Li, G.D.; Wu, Y.Y.; Gao, R.Q.; Zou, X.X. Vertically Grown CoS Nanosheets on Carbon Cloth as Efficient Hydrogen Evolution Electrocatalysts. *Int. J. Hydrogen Energy* **2017**, *42*, 9914–9921. [[CrossRef](#)]
182. Ouyang, C.B.; Wang, X.; Wang, S.Y. Phosphorus-Doped CoS₂ Nanosheet Arrays as Ultra-Efficient Electrocatalysts for the Hydrogen Evolution Reaction. *Chem. Commun.* **2015**, *51*, 14160–14163. [[CrossRef](#)] [[PubMed](#)]
183. Li, H.M.; Qian, X.; Xu, C.; Huang, S.W.; Zhu, C.L.; Jiang, X.C.; Shao, L.; Hou, L.X. Hierarchical Porous Co₉S₈/Nitrogen-Doped Carbon@MoS₂ Polyhedrons as pH Universal Electrocatalysts for Highly Efficient Hydrogen Evolution Reaction. *ACS Appl. Mater. Interfaces* **2017**, *9*, 28394–28405. [[CrossRef](#)] [[PubMed](#)]



© 2018 by the authors. Licensee MDPI, Basel, Switzerland. This article is an open access article distributed under the terms and conditions of the Creative Commons Attribution (CC BY) license (<http://creativecommons.org/licenses/by/4.0/>).